Search for new long-lived hadronically-decaying particles produced in association with a Z boson with the ATLAS detector at the LHC

by

Michael David Werner

A dissertation submitted to the graduate faculty

in partial fulfillment of the requirements for the degree of

DOCTOR OF PHILOSOPHY

Major: High Energy Physics

Program of Study Committee:
Chunhui Chen, Major Professor
Soeren Prell
John Lajoie
James Cochran
Steve Kaust

Iowa State University

Ames, Iowa

2018

DEDICATION

I would like to dedicate this thesis to my parents, Mark and Sandi, without whose support I would not have travelled this path. Also to my husband Ryan who kept me going when I needed it most.

I would also like to thank all my friends and family for their efforts to pull me away from the work from time to time and keep me sane.

TABLE OF CONTENTS

ACKNOWLEDGEMENTS

I would like to take this opportunity to express my thanks to those who helped me with various aspects of conducting research and the writing of this thesis.

For his helpful advice, guidance, and great expertise I would like to thank my major professor Chunhui Chen.

For sharing their expertise from across the world when I did not have any nearby, I would like to thank Rachel Rosten and Heather Russell.

For introducing me to physics at a young age and encouraging my passion for it, I would like to thank my high school teacher Virgil Arns.

For reading and providing valuable suggestions on my thesis, I am grateful to the members of my committee : Chunhui Chen, Soeren Prell, Jim Cochran, John Lajoie, and Steve Kautz.

For all that I have learned from them, I would like to express my gratitude to the Iowa State High Energy Physics group.

And to the ATLAS Collaboration, it is an honor to be a part of such an experiment and I am thankful to everyone who made it possible for students like me to learn more about the wonders of nature and its fundamental constituents.

ABSTRACT

The standard model fails to fully explain several observations about the universe, one of the prominent ones is the existence of dark matter. Many different models have been proposed for dark matter candidates, but it is possible that the dark matter itself will remain elusive. Dark sector models contain both dark matter and a new force which acts upon it. The force-carrying boson of this dark sector may be more easily detected than dark matter itself. These models contain a number of free parameters, some combinations of which result in the dark sector particle being long-lived but unstable, resulting in a unique experimental signature.

A search is presented for the production of an uncharged long-lived particle in association with a standard model Z boson. The search is based on 36.01 fb^{-1} of proton-proton collision data at $\sqrt{s} = 13$ TeV recorded in 2015-2016 with the ATLAS detector at the Large Hadron Collider. Data are analyzed in a dilepton + jets region which is characterized by two high transverse momentum electrons or muons and at least one jet with a very large fraction of its energy deposited in the hadronic calorimeter. Background rates for such jets are estimated using a single lepton + jets region consistent with a lepton from the decay of a standard model W boson.

No significant excess is observed and 95% confidence level upper limits are derived on the cross section times the branching ratio as a function of the particle's proper lifetime.

CHAPTER 1. INTRODUCTION

All natural phenomena can be described by one of the four fundamental forces : gravitational, electromagnetic, the weak nuclear force, and the strong nuclear force. The last three of these constitute the Standard Model (SM) of particle physics.

Despite the many successes of the Standard Model (experimentally verified quantities and predictions) there are many reasons to believe that it is not the complete explanation for the universe.

Gravity is not included in the theory, dark matter and dark energy are still unexplained, and within the Standard Model itself there lies no explanation for the widely varying masses of the particles.

To address these problems with the Standard Model, many new theoretical models have been proposed - many of which posit the existence of a "Dark Sector" of particles which do not normally interact via Standard Model forces.

The work presented in this thesis comprises a search for signs of such a dark sector via an exotic decay (a signature not expected from SM physics).

CHAPTER 2. THE STANDARD MODEL AND THE DARK MATTER HYPOTHESIS

2.1 The Standard Model

What is matter made of and why does it interact the way it does? Particle physics seeks to answer these questions. The current understanding of particles and their interactions is consolidated into the Standard Model (SM) of particle physics. According to the SM, matter is composed of fundamental particles called quarks and leptons and the forces between these particles are carried by particles called gauge bosons. Additionally there is the Higgs boson, which gives the fundamental particles their masses. These particles are all summarized in Figure 2.1.

Fundamental particles are considered to be point-like - having no volume or internal structure. Each of these particles has an anti-particle with the same mass but opposite electric charge. Fundamental particles without electric charge are their own anti-particles.

2.1.1 Fundamental Forces

There are two fundamental forces that most people are familiar with : gravity (which holds us to the Earth) and electromagnetism (which we use for many things - from moving a compass needle to operating probes in space). The two remaining forces are very short-ranged and operate on the scale of atomic nuclei. Inside the nucleus of an atom are packed many positively charged protons (in a material like lead, for instance, there are 82 such protons). Normally the electromagnetic force would push all of these protons apart but a ‘strong nuclear force’ holds them together. This force is carried by particles aptly named ‘gluons’. Similarly to the electromagnetic force which acts on electrically charged particles - the strong nuclear force only acts on particles with ‘color charge’.

Occasionally the neutron within a nucleus will become a proton - releasing an electron in the process. This change happens via the fourth and final fundamental force - the ‘weak nuclear force’.

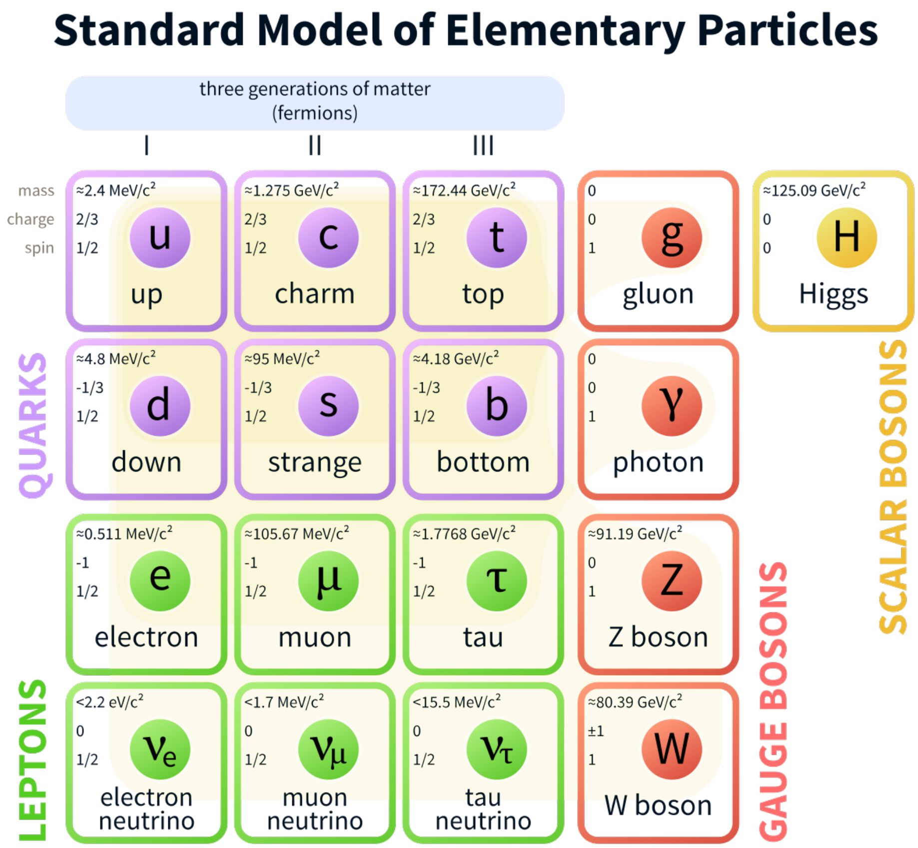

Figure 2.1: The Standard Model of Particle Physics

The weak nuclear force has 3 force carrying particles - 2 electrically charged W bosons and 1 uncharged Z boson.

2.1.2 Leptons

Leptons are spin-1/2 fermions that interact via all forces except for the strong nuclear force (because they do not carry color charge). There are 3 'generations' of leptons - characterized by their different mass scales and lifetimes. The electron is the lightest charged lepton and is completely stable (i.e. it does not decay). The muon is the next lightest charged lepton, about 200 times the mass of the electron. Unlike the electron, the muon is unstable - with a proper lifetime of 2 microseconds...however because many muons are produced with large speeds by interactions in Earth's upper atmosphere a small fraction make it all the way down to the surface before decaying. In fact - muons are traveling through us all the time [57]. The third and heaviest charged lepton is the tau which is about 17 times more massive than the muon. Like the muon the tau is unstable - decaying within 3×10^{-13} seconds. (The reason for these lifetimes will be discussed in Section 2.3.3.2).

Each charged lepton has a corresponding neutral partner called a neutrino (called the electron neutrino, muon neutrino, and tau neutrino respectively). Neutrinos of each generation are completely stable and 'nearly massless' particles. Neutrinos rarely interact with matter at all - countless numbers of them pass through our planet every moment unimpeded.

2.1.3 Quarks

Quarks are the building blocks of the more familiar particles - the proton and the neutron (collectively called nucleons). Each nucleon is made up of 3 quarks : the proton is composed of two u quarks and a d quark while the neutron is composed of 2 d quarks and a u quark.

Experiments have revealed 6 different quarks : The u (up) quark, the d (down) quark, the s (strange) quark, the c (charm) quark, the b (bottom) quark, and the t (top) quark. Like the leptons these 6 particles are organized into 3 generations - u and d, s and c, and b and t. Also like the leptons each generation has a greater mass than the one before. In addition to their electric charge, quarks carry color charge.

The strong nuclear force is so strong that any quarks produced in collisions quickly pull other quarks from the quantum vacuum to form color-neutral particles - converting the energy of their bond into mass in the form of other quarks. When a quark anti-quark ($q\bar{q}$) pair creates a color-neutral particle we call it a meson, and when a triplet of quarks create a color-neutral particle we call it a baryon. The majority of the mass of many mesons and baryons (99% of the proton mass [36]) comes from the strong force field energy rather than the mass of the constituent quarks (exceptions are mesons and baryons made up of the heavier quarks). This means that while the

Higgs mechanism is responsible for the quark mass, the majority of the visible mass in the universe comes from the strong force.

2.1.4 Gauge Bosons

In the mathematical formulation of quantum field theory, the Lagrangian can be made invariant under a local gauge transformation by the addition of a field called a "gauge field". The quantum of this gauge field is referred to as a gauge boson. The gauge bosons within the standard model consist of the photon (a massless particle which mediates the electromagnetic force), the W and Z bosons (which mediate the weak nuclear force), and the gluon (which mediates the strong nuclear force). All of these bosons have been experimentally verified and their properties measured. The discovery of the massive W and Z bosons were an important verification of the validity of the Standard Model.

2.1.5 Higgs Boson

On July 4th, 2012 the ATLAS and CMS experiments announced the discovery of a new particle consistent with the SM Higgs boson. By March of 2013 CERN had confirmed that the particle was indeed a Higgs. The Higgs mechanism explains why some particles have mass while others do not (for example, the photon is massless but the W and Z bosons are very massive). This discovery was the last particle of the Standard Model which remained to be found - cementing the validity of the theory.

Discovery of the Higgs boson was the primary motivation in the design of the LHC, and now that the particle has been found a plethora of new searches have been spawned to look for new properties or new particles resulting from its decay.

The SM Higgs is expected to decay in many different ways [49], the relative branching fractions for the most dominant decay modes are shown in Table 2.1. It is noteworthy that the first discovery of the 125 GeV Higgs boson occurred in measurements of the $H \to \gamma\gamma$ decay channel, despite the

Table 2.1: The dominant expected branching fractions of the 125 GeV SM Higgs boson with theoretical uncertainties. [49]

Decay Channel	Branching Ratio	Relative Uncertainty
$H \rightarrow b\bar{b}$	0.584	$\pm 3.3\%$
$H \rightarrow W^+W^-$	0.214	$\pm 4.3\%$
$H \rightarrow \tau^+\tau^-$	0.063	$\pm 5.7\%$
$H \rightarrow ZZ$	0.025	$\pm 4.3\%$
$H \rightarrow \gamma\gamma$	0.002	$\pm 5.0\%$
$H \rightarrow Z\gamma$	0.002	$\pm 9.0\%$

fact that it is expected to decay to that final state only 0.2% of the time. This is due to the final state of two high energy photons having very few background processes.

Any deviation from these predicted branching fractions can be interpreted as a sign of new physics, and a possible new particle. For example, the $H \rightarrow \gamma\gamma$ decay occurs via a loop (shown in Figure 2.2). While this loop can be made with any charged SM particles the more massive a particle the greater the fraction it contributes. The massive top quark and W boson thus make up the vast majority of the branching fraction. If there exists another massive charged particle to which the Higgs couples then the branching fraction measured will deviate from the expected SM calculation.

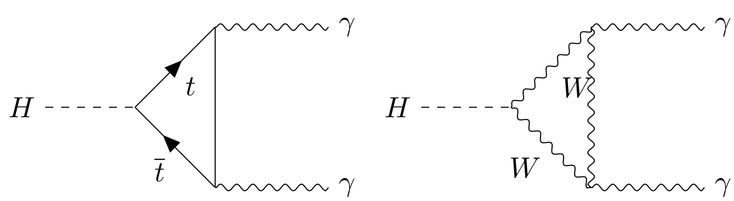

Figure 2.2: The dominant tree-level Feynman diagrams of the decay of the SM Higgs boson to a pair of photons. The presence of a non-SM particle could contribute to this loop, resulting in a different branching fraction for the $H \rightarrow \gamma\gamma$ decay than predicted by the SM. All Feynman diagrams in this document were drawn using the TikZFeynman package [37].

Branching fractions are only one of a large number of possible Higgs measurements which could indicate deviations from the SM. Other useful measurements include the mass and width of the Higgs boson, the coupling strength of the Higgs to all SM particles (these couplings would be universally affected by a hidden sector of particles), and even the production rate of the Higgs at the LHC (related to coupling to gluons) [38].

2.1.6 Incomplete

Despite the success of the Standard Model in explaining known physics and accurately predicting the existence of previously unknown particles - there are many phenomena that continue to defy explanation :

Neutrinos : The SM predicts that neutrinos are massless, however experiments indicate that they have mass (albeit small).

Gravity : The SM does not have an explanation for gravity. Attempts to introduce a new gauge boson (graviton) have been unsuccessful.

Dark Matter : The SM does not contain an explanation for Dark Matter

Matter-Antimatter Asymmetry : The SM does not explain why the visible universe contains matter and not antimatter - when we produce matter in our experiments they come in almost equal parts (there are known processes that violate CP symmetry, such as the decays of kaons and B mesons).

Dark Energy : The SM does not explain the accelerating expansion of the universe (a phenomenon known as 'dark energy')

Inelegance : The SM has many independent constants (19) which must be set. Some physicists argue that this is inelegant.

These unexplained phenomena suggest that the SM is still incomplete, and thus the majority of analyses in the field of high energy physics attempt to address at least one of these concerns. This analysis focuses on an explanation for dark matter, and so the following sections will explain the mystery of dark matter in greater detail.

2.2 Dark Matter

Astrophysical observations have indicated that the universe contains a significant amount of mass which is not visible. While some models seek to explain this away by modifying gravity or invoking known invisible objects (i.e. brown dwarfs and black holes), another (and arguably simpler) possibility is that there exists some unknown stable form of matter which doesn't interact electromagnetically.

2.2.1 Rotation Curves

The first evidence for the existence of dark matter came from the rotation speeds of stars within their galaxies. The speeds at which many stars orbit the centers of their galaxies are so fast at the edges that the gravity from the visible mass indicates the stars should be able to escape. Calculations show that these galaxies must have at least *six* times the visible matter in the form of invisible matter just to hold the galaxy together. The rotation curve for Galaxy M33 is shown in Figure 2.3.

This phenomenon of an invisible source of gravity is even more pronounced when studying clusters of galaxies. The Coma cluster in particular contains galaxies moving so fast that they should be flying apart, leaving the cluster. Similar calculations show that the dark matter could outnumber the visible matter in the Coma cluster by a factor of 100 to 1. [47]

2.2.2 Known Invisible Matter

The first place to look for an explanation for this matter is what is already known. There are several astrophysical objects which do not emit light and yet have mass, such as interstellar gas, planets, brown dwarfs, and black holes.

While many of the astrophysical objects mentioned do not emit light of their own, they do absorb light that falls on them and emit their own radiation based on their temperature. Absorption spectra from stellar light shone through clouds of interstellar dust allow the determination of the composition of such clouds. Gas clouds, brown dwarfs, and gas giant planets emit light very freely in

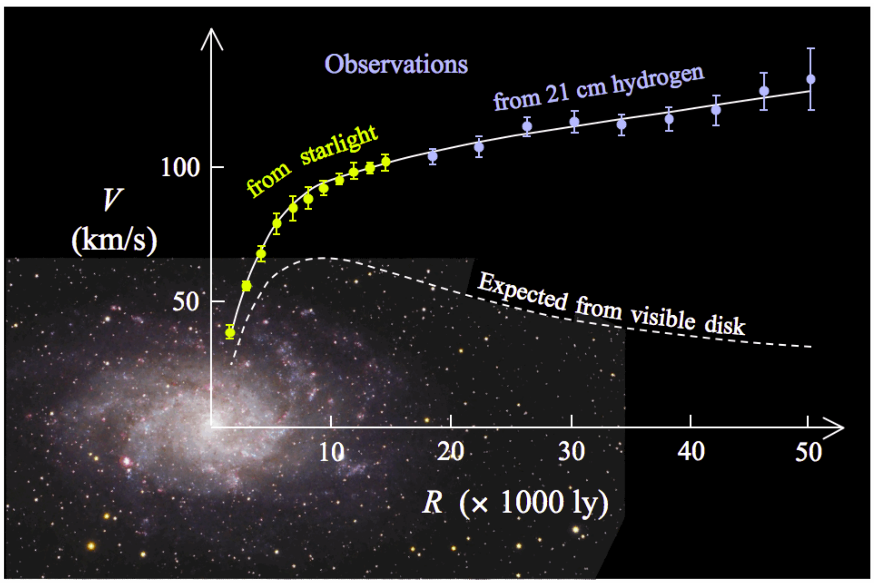

Figure 2.3: Rotation curve for galaxy M33 [32]. The speeds of the stars within the disk were determined by measuring the degree of red/blue shift in the average stellar spectrum as well as the 21cm hydrogen line (which better penetrates gas clouds). The observed luminosity is used to determine the approximate mass as a function of radial distance, and is extremely inconsistent with the observed rotational speeds.

the infrared spectrum, enabling measurement via luminosity. Rocky compact planets (like our own) are much smaller targets and therefore more difficult to detect. However we have recently begun to inventory these objects by observing the effects of their gravity on their companion stars in our own galaxy. The total mass of planets do not compare to the masses of their suns. Dark matter is known to be dispersed in many galaxies. For black holes to produce the observed gravitational effects they must be numerous, which also implies they must be of relatively low mass (similar to the mass of our sun). Conventional calculations do not allow any stars less than ≈ 15 solar masses to undergo the gravitational collapse necessary to form such black holes. During the inflationary period of our universe (in the years after the big bang before the first stars shone) fluctuations in density could have produced black holes in a variety of masses. Such objects are called "primordial" black holes [42]. With the recent detection of relatively light black hole mergers by LIGO this hypothesis has gained renewed interest and is an active area of investigation[43, 29].

2.2.3 The Bullet Cluster

Two principle explanations exist to explain these astrophysical observations : either there is some invisible matter present or our understanding of gravity is wrong at galactic scales. The bullet cluster of galaxies (shown in Figure 2.5) presented the strongest evidence in favor of the former [31].

The bullet cluster is the aftermath of a collision between two clusters of galaxies. The galaxies (being relatively small targets) passed by one-another while the intergalactic gas clouds collided - heating up in the process and releasing X-rays. With the gas and the stars visible most of the normal matter can be accounted for - and the mass distribution determined. Next using gravitational lensing the gravitational distribution was determined. Comparing the two a separation of more than 8 standard deviations was discovered between the centers of visible mass and the centers of gravity. This measurement is best explained by each cluster of galaxies possessing a large mass of dark matter which is unimpeded by the collision while the majority of the visible mass is slowed (the interstellar gas makes up $\approx 80\%$ of the total visible mass of the cluster). This was the clearest signature yet that dark matter is not simply a misunderstanding of the force of gravity but something particulate.

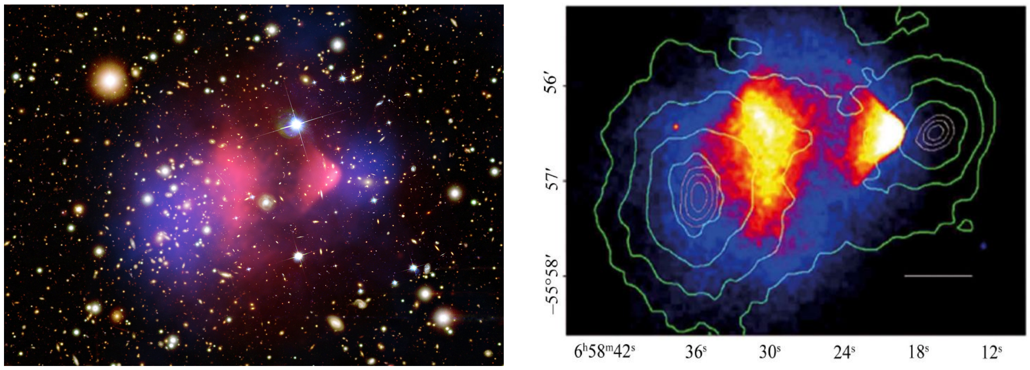

Figure 2.5: The bullet cluster. The X-ray gas clouds (shown in pink) are compared to the center of mass of the cluster (shown in blue). The gravitational contours (determined by gravitational lensing) are shown on the right. The centers are separated by more than 8 standard deviations, indicating a high degree of certainty that the visible matter is not the only source of gravity. [31]

Further evidence for the particle hypothesis is presented in a recent study which discovered a galaxy (NGC1052DF2) in which the visible matter completely accounts for the gravitation. [56]

2.2.4 Structure Formation

Calculations of the early universe indicate that the expansion of the universe was so rapid that if only normal matter were present then stars and galaxies would never have formed - as the matter would fly apart much too fast. Thus the presence of clustered dark matter is critical for the formation of the universe as we know it. If the dark matter particles in this early universe were extremely light then they would travel at relativistic speeds (i.e. be "hot") and therefore not clump together (see Figure 2.6). Therefore "cold" dark matter (CDM) is the favored hypothesis for dark matter (CDM particles must have a relatively large mass to move at non-relativistic speeds in the early universe).

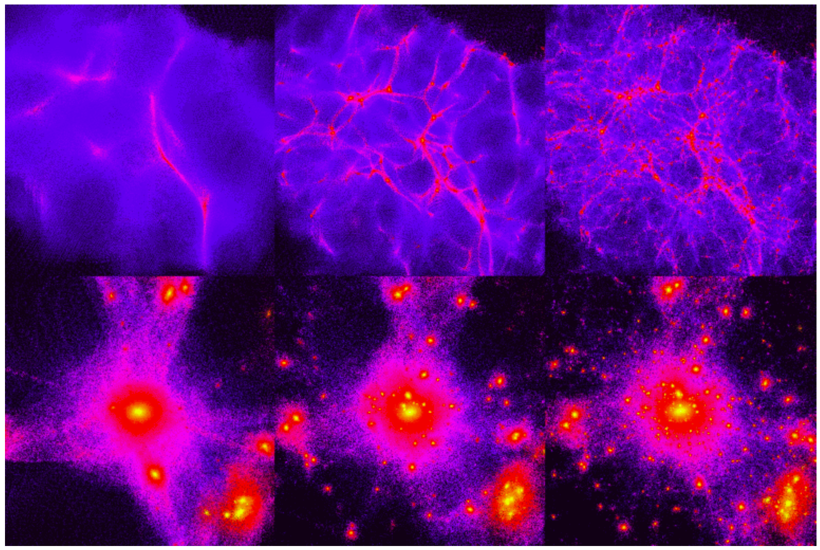

Figure 2.6: Top row: Simulations of what structure in Hot (left), Warm (middle), and Cold (Right) dark matter universes would look like at high redshift (early times). Bottom row: same as top row, except now as they would look at the present time (z=0).[35] Our universe contains many smaller galaxies in clusters which is most consistent with the Cold Dark Matter (CDM) simulation.

2.3 Beyond the Standard Model

If dark matter is indeed particulate then it must have the following properties

- **Uncharged :** Dark matter doesn't interact electromagnetically and therefore it must not carry an electric charge. (This rules out the charged leptons e, μ, τ, all quarks, and the charged $W^{\pm}$ gauge bosons).
- **Non-Zero Mass :** It must have mass (ruling out the photon and gluon).
- **Long Lifetime :** It must be relatively stable with a lifetime longer than the current age of the universe (ruling out the remaining bosons, Z and H).
- **"Cold" :** It must have enough mass to move non relativistically in the early universe (while neutrinos do have some mass - experiments indicate the masses are far too small to be CDM).

These requirements indicate that some new particle must exist that is not included in the Standard Model and therefore requires new theory. Several models have been proposed, including supersymmetry (SUSY) models in which the DM candidate is a gravitino or neutralino, axions, extra dimensions, or a generic hidden sector (in which there exists a new force and corresponding "dark charge" carried by particles)[24, 3]. For this thesis a generic hidden (or "dark") sector model is tested.

2.3.1 The Dark Sector and Metastablility

Since the discovery of the Higgs boson in 2012, there is significant evidence that the origin of mass via interactions with the Higgs field is correct. Because this field gives most SM particles mass, it is an excellent target for searches of BSM particles - including dark matter itself which would show up as a large amount of missing energy (the stable particles would simply leave the detector without interacting with it).

There is, however, the possibility that this production may be elusive, or even impossible for the Higgs boson (for example, if the dark matter particle has a mass greater than half of that of the Higgs boson then the decay is not kinematically possible). In this case it may be possible to search instead for other non-stable particles which interact with stable dark matter in the same way that our SM Z/γ bosons interact with leptons (a so-called "dark sector" particle). One such proposed particle is the dark photon. Such a particle which mediates an interaction between stable dark matter particles may also couple to standard model particles more strongly than the stable dark matter itself. At large masses ($> 10GeV$) the "dark photon" can mix with the standard model Z boson. In this regime it is also often referred to as a "dark Z" (Z_d).

2.3.2 Long Lived Particles

A long-lived particle (LLP) is any particle which travels a measurable distance within our experiment before decaying. There are such particles (hadrons) within the Standard Model summarized in Table 2.2. Note that the table is presented with two different units : the first (ns) is an intuitive definition of a proper lifetime in the rest frame, the second (mm/c) is a more useful experimental definition which is a good indication of how far a fast moving (highly boosted) particle will travel in our experiment. For the ATLAS experiment the top items in the Table 2.2 highlighted in gray are considered 'stable' while those at the bottom and highlighted in light gray are considered 'prompt' and do not travel far enough into the detector to measure.

Table 2.2: Proper lifetimes of a few selected Standard Model particles, intended to demonstrate the range of proper lifetimes.

Particle (quark content)	**Proper Lifetime [ns]**	**[mm/c]**
n (udd)	880×10^9	2.6×10^{14}
μ^+/μ^- (lepton)	2200	6.6×10^5
π^+/π^- (ud)	26	7800
K_L^0 (ds)	0.50	150
many B hadrons (b)	0.001	0.30
τ^+/τ^- (lepton)	2.9×10^{-4}	0.09
t (top quark)	5×10^{-25}	3×10^{-11}

2.3.3 Theoretical Mechanisms

There are a variety of mechanisms which can result in a particle having a long lifetime. These mechanisms arise in a number of different models - each of which can have their own dark matter candidates.

2.3.3.1 Ultra Small Couplings

The most basic origin of a long-lived particle is an extremely small coupling to other particles. For the toy model depicted in Figure 2.8 we can say that the lifetime is related to the coupling g as $\tau \propto 1/g^2$. However the exact same vertex (with the time reversed) determines the production cross-section from collisions of Standard Model quark which is related to the coupling as $\sigma \propto g^4$. The result of these two factors being in balance with one-another is that any particle which is "long-lived" will have such a small production cross-section that it will never be produced. Instead such particles must be produced via some other process (usually through the decay of a more massive 'mediator').

Figure 2.8: This is a generic decay/production process. The process is time-symmetric so the cross-section of the interaction is related to the lifetime of the decaying particle.

2.3.3.2 Massive Mediators

Some long-lived particles can decay only through a relatively massive mediating particle. One example of this is the decay of the Standard Model muon, which is illustrated via the Feynman diagram in Figure 2.9. From this diagram the lifetime of the muon is related to the mass of the mediator as $\tau_\mu \propto \frac{M_W^4}{g^4 m_\mu^5}$. [40] Note that the proper lifetime scales enormously according to the W boson mass. In many models with LLPs the mediators are considered to exist at the TeV scale or higher.

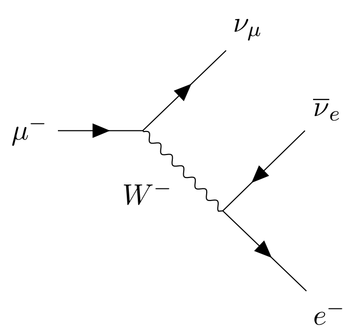

Figure 2.9: Decay of the SM muon. This decay occurs only via the massive mediating W boson. Due to the large mass of the mediator relative to the decaying particle the proper lifetime of the decay is very large.

2.3.3.3 Small Mass Differences

The final mechanism that will be discussed is that illustrated in Figure 2.10. In this toy model if the mass of particle C is extremely small compared to A and B, then the momentum phase space available for this decay is given by $|\vec{p}| \approx (m_A^2 - m_B^2)/(2m_A)$. This momentum space appears in the denominator of the lifetime expression - resulting in an inverse dependence $\tau \propto \frac{m_A^3}{m_A^2 - m_B^2}$.

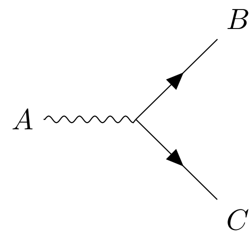

Figure 2.10: Toy Model : Mass Difference

This mechanism is very common in SuperSymmetry (SUSY) models - where the lightest supersymmetric particle (LSP) is a completely stable dark-matter candidate while the next-to-lightest supersymmetric particle (NLSP) is a particle of slightly larger mass which may be more easily detected.

2.3.4 Hidden Valley Model

The model considered throughout the rest of this paper is illustrated by the Feynman diagram shown in Figure 2.11. [33] A massive scalar mediator Φ (possibly a Higgs boson H) decays into a dark-sector boson Z_d and a standard model Z boson. In this model the Z_d is long-lived, with a proper lifetime on the order of $\approx$ 1m/c.

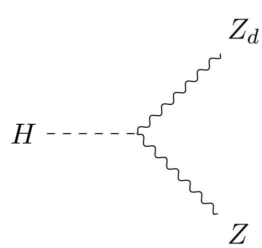

Figure 2.11: Feynman diagram for $H/\Phi \to ZZ_d$

Monte Carlo samples of Φ/H boson production in the gluon-gluon fusion mode with $\Phi/H \to ZZ_d$, $Z \to \ell^+\ell^-$ and $Z_d \to gg, b\bar{b}$ or $c\bar{c}$ are generated by the Powheg-Box v2 generator interfaced to Pythia 8.210 with the NNPDF23LO [22] PDF set with the A14 tune [11]. Here it is assumed that the dominant decay final states of the Z_d are $Z_d \to gg, b\bar{b}$ or $c\bar{c}$, preferentially to the heaviest quarks kinematically allowed. However, this analysis is not sensitive to the different flavors of partons as decays within the volume of the ATLAS calorimeter occur shortly (study detailed in Sec 4.3.2)). Nine samples were produced at different mass points of Φ and Z_d, three of which are at the SM Higgs mass, $m_\Phi = 125\text{GeV}$, as described in Table 2.3.

In this model the Z_d is uncharged and therefore leaves no tracks within the ATLAS tracker (see Sec 3.2.2) before it decays. If the Z_d decays within the volume of the ATLAS hadronic calorimeter (see Sec 3.2.4), forming a CalRatio (CR) jet (described in detail in Section 4.3). Some fraction of the Z_d will decay further within the detector, leaving displaced charged tracks, and some fraction of them will decay outside the detector completely (resulting in missing transverse energy). For each of the signal MC samples, the proper lifetime of the Z_d is chosen to maximize the probability for it to decay inside the HCal barrel which exists between 2.28 and 4.25 meters from the beamline. The precise geometry of the ATLAS detector is described in detail in Section 3.2.4. These studies suggest that at most only about 20 percent of produced LLPs will decay within the volume of the HCal, as shown in Figure 2.12.

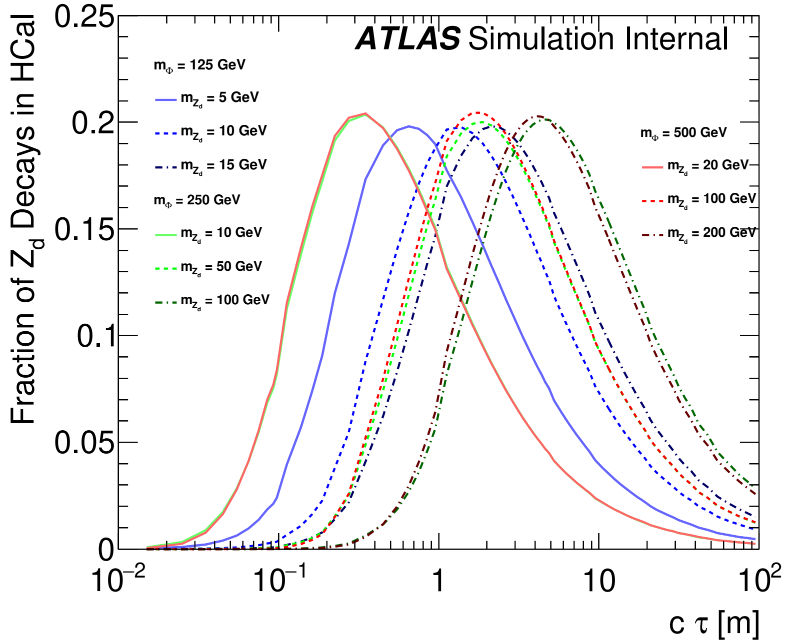

Figure 2.12: The probability of a Z_d boson to decay within the volume of the hadronic calorimeter as a function of its proper lifetime for different choices of Φ mass and Z_d mass.

Table 2.3: The masses of the mediator and LLP are shown for each sample generated. Each sample was generated at a proper lifetime which optimized the number of events passing our selection criteria.

m_Φ [GeV]	m_{Z_d} [GeV]	τ_0 [m/c]	# of events
125	5	0.6	116 000
125	10	1.3	115 000
125	15	2.6	114 000
250	10	0.4	118 000
250	50	2.0	117 000
250	100	3.0	118 000
500	20	0.4	114 000
500	100	2.2	114 000
500	200	3.0	116 000

CHAPTER 3. THE LHC AND THE ATLAS EXPERIMENT

3.1 The LHC

The Large Hadron Collider (LHC) [20] is the world's largest and most powerful particle accelerator. The facility is located near Geneva, Switzerland and operated by the European Council for Nuclear Research (CERN), shown in Figure 3.1. The 27 km accelerator ring boosts the speed of charged particles to nearly the speed of light.

Figure 3.1: An aerial view of the Large Hadron Collider (LHC). Geneva, Switzerland

Particle accelerators function by using radio-frequency (RF) cavities to accelerate charged particles. At these accelerators there are two factors important for experiments : high energy collisions (to produce particles that we've never seen before), and frequent collisions (so that much data can be collected - as many searches are looking for rare events). A circular accelerator is ideal for this reason as un-collided particles are recycled (maintaining a high luminosity beam).

The use of circular accelerators does come with an intrinsic energy limit to which particles can be boosted. The more energy a particle has, the faster it moves and the stronger magnets must be to deflect the particle into a circular motion. This deflection requires powerful magnets, the strength required scaling inversely with the accelerator radius ($B \propto \frac{1}{r}$). Additionally, as a charged particle is deflected by a magnetic field it emits photons (referred to as synchrotron radiation), which carry away some of the particle's energy. At a certain energy the particle will lose all of the energy it gains from the accelerator via synchrotron radiation. The rate of power loss is proportional to the inverse square of the radius of the trajectory ($P \propto \frac{1}{r^2}$). If the magnets available have a fixed strength then both of these relationships result in a larger radius accelerator being required to produce higher energy beams.

The proton beams of the LHC consist of bunches of 10^{11} protons each separated by about 25 ns (a distance of about 7.5m) at an energy of 6.5 TeV each. The large number of protons in a bunch ensures a high probability of a proton collision when the beams are crossed. The bunches collide 40 million times per second (40 MHz) inside each of the 4 detectors : two general-purpose detectors ATLAS and CMS, a specialized detector for studying b hadrons - LHCb, and a detector for studying heavy ion collisions - ALICE. With so many protons in each bunch there are often multiple proton-proton collisions in each crossing. Such interactions are called "pileup" and will be discussed in detail in Section 3.2.8.

The beams are produced by stripping hydrogen gas of its electrons (via heating and an electric field) and pumping it through a series of smaller accelerators shown in Figure 3.2. A linear accelerator (LINAC 2) boosts the protons to 50 MeV before they enter the proton synchrotron booster which further accelerates them to 1.4GeV. After the PS BOOSTER the beam enters the Proton Synchrotron itself which is a circular accelerator which takes them up to 25 GeV before entering the Super Proton Synchrotron (SPS - a ring 7km in circumference) which accelerates them to 450 GeV. From the SPS the beam is split into two and injected into the LHC where they quickly reach the 6.5 TeV at which the accelerator is currently operating.

Proton bunches at the LHC are organized consecutively into groupings called bunch trains which includes 36 bunches each separated by a bunch spacing of 25ns. This spacing defines the smallest unit of time, and therefore distance, that separates consecutive bunch sites, with each assigned a unique bunch crossing identification (BCID). Bunch spacings are assigned a BCID whether they are filled with protons or are empty. Bunch trains are generally separated by only a few empty BCIDs. A single larger gap of roughly 300 empty BCIDs ($\approx 7\mu$s) allows for quick detector calibrations during data-taking.

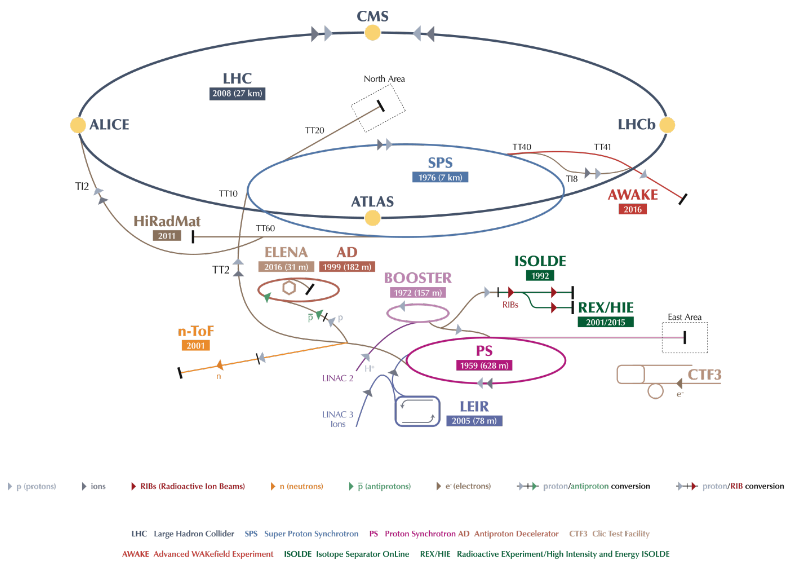

Figure 3.2: A diagram of each accelerator system used to inject protons into the LHC beam.

The LHC was brought online in 2015 after a long shutdown which was used to repair the various detectors and delivered a total luminosity of 3.21fb^{-1} before the year's end. In 2016 the collider was online for much longer and the instantaneous luminosity of the beams was increased, allowing 10 times as much data (32fb^{-1}) to be collected. This surpassed the amount of data collected during Run 1 (2011-2012) by about 50%, as shown in Figure 3.3.

The luminosity collected by the ATLAS detector during 2015+2016 as well as the pileup conditions are summarized in Table 5.1.

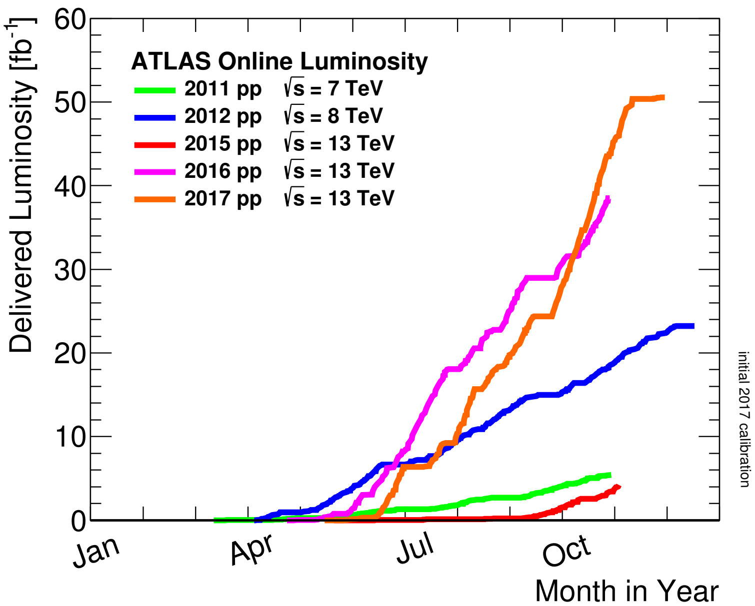

Figure 3.3: The luminosity delivered by the LHC to the ATLAS detector (by year).

Table 3.1: The total integrated luminosity $\int \mathcal{L}dt$ and the average number of interactions per bunch crossing in each data-taking period.

Period	max. $\mathcal{L}$ (cm^{-2}s^{-1})	$\int \mathcal{L}dt$ (fb^{-1})	average $\langle\mu\rangle$
2015	0.50×10^{34}	3.21	13.6
2016	1.37×10^{34}	32.86	24.9

3.2 The ATLAS Experiment

The ATLAS detector was designed as a general purpose detector built with these criteria in mind :

- High resolution tracking at large energies. This is important also for determining the electric charge of particles which curve in the presence of a magnetic field.
- Good electromagnetic calorimetry for electron and photon measurement and identification
- Excellent hadronic calorimetry for accurately reconstructing jets
- High precision muon momentum resolution
- Triggering at low energy (GeV scale) to optimize the efficiency of most physics processes

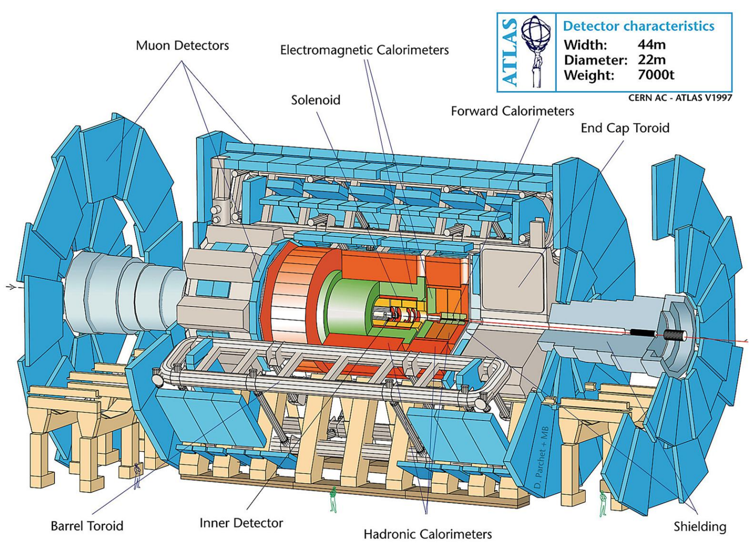

Figure 3.4: The ATLAS Detector

The cylindrical detector stands 25 meters in diameter and 44 meters in length. The detector is built in layers with the tracking system closest to the beamline followed by the electromagnetic calorimeter, the hadronic calorimeter, and finally the muon spectrometer. The following sections describe each of these systems, with many of the details taken from the original technical design report [4].

3.2.1 Coordinates and Measured Quantities

The ATLAS experiment uses a coordinate system with the origin at the nominal interaction point (IP) where the proton beams collide. The beams travel along the z-axis and the transverse (x-y) plane is defined with the x-axis towards the center of the LHC ring and the y-axis upwards. In the transverse plane the cylindrical coordinates (r, ϕ) are used (with the azimuthal angle ϕ defined from the x-axis). Pseudorapidity is regularly used in lieu of the polar angle and is defined by $\eta = -\ln[tan(\frac{\theta}{2})]$. The 'angular' distance between objects is regularly defined as $\Delta R = \sqrt{(\Delta\eta)^2 + (\Delta\phi)^2}$. Due to the fact that practically all of the momentum of the beams lies in the z-direction the momentum in the transverse plane is well constrained and is therefore well suited for analysis. Such quantities are often indicated by a capital 'T' subscript (e.g E_T, p_T, m_T, etc).

3.2.2 Tracker

The ATLAS Tracker (shown in Figure 3.5, also referred to as the Inner Detector or ID) is made up of three main systems : the pixel detector, the semiconductor tracker (SCT), and the transition radiation tracker (TRT). These systems lie within a 2T magnetic field which causes charged particles to curve in their flight paths.

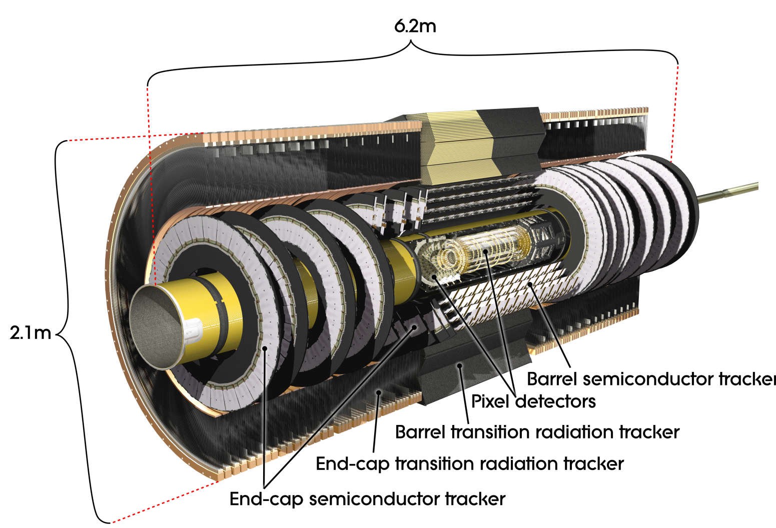

Figure 3.5: The tracking system of the ATLAS detector

The pixel detector and SCT are very finely segmented silicon strips and lie closest to the beamline while the TRT uses gas filled tubes (in the same fashion that a Geiger counter works).

A charged particle inside a magnetic field travels in a curved trajectory, the radius of which is directly related to the charge, momentum, and mass of that particle.

3.2.3 Electromagnetic Calorimeter

The ATLAS electromagnetic calorimeter (often referred to as the ECal) lies just beyond the tracker and outside of the solenoid of the tracking magnet. A small section of the ECal is shown in Figure 3.6. The ECal is made of three layers of lead absorber plates and filled with liquid argon (LAr), chosen for its high radiation tolerance and uniformity. The LAr is kept at 89 K through the use of cryostats. Readout electrodes are placed between absorber plates and held at a potential of 2kV to collect ions produced by charged particles traveling through the LAr. The average drift time of ions through the LAr is 450ns. Because of the long drift time, to obtain accurate tracking information the signal readout is recorded every 25 ns. The readouts are then checked to determine the shape of the signal peak, which allows calculation of the amplitude and time of the energy deposit.

Any charged particles will lose some energy via bremsstrahlung radiation (emitting photons) when interacting with absorber material, however the power radiated has a strong dependence on the particle mass (varying between m^{-4} and m^{-6} depending on the precise kinematics) [39]. This means that electrons lose energy at a rate $(m_p/m_e)^4 \approx 10^{13}$ times faster than protons, and $(m_\mu/m_e)^4 \approx 10^9$ times faster than muons. If the emitted photons are of large enough energy ($\gtrapprox 1GeV$) then they will produce electron-positron pairs each of which will continue to emit bremsstrahlung photons in a chain until the energy of each particle becomes very small ($\lessapprox 10MeV$). At low energies the electrons lose their energy through ionizing the material while photons lose their remaining energy via Compton scattering and the photoelectric effect. [39] The energy of the shower is measured in the detector via the amount of ionization left in the calorimeter cell.

The energy loss happens so rapidly for electrons and photons (due to the low mass of the electron) that the ECal can be relatively thin and still absorb all of the energy without stopping heavier particles.

The thickness of the ECal was chosen to collect all of the energy from photons and electrons, and some small fraction of the energy of the other charged particles which pass through it. By combining this information with the tracking system we can distinguish photons, positrons, and electrons from other particles.

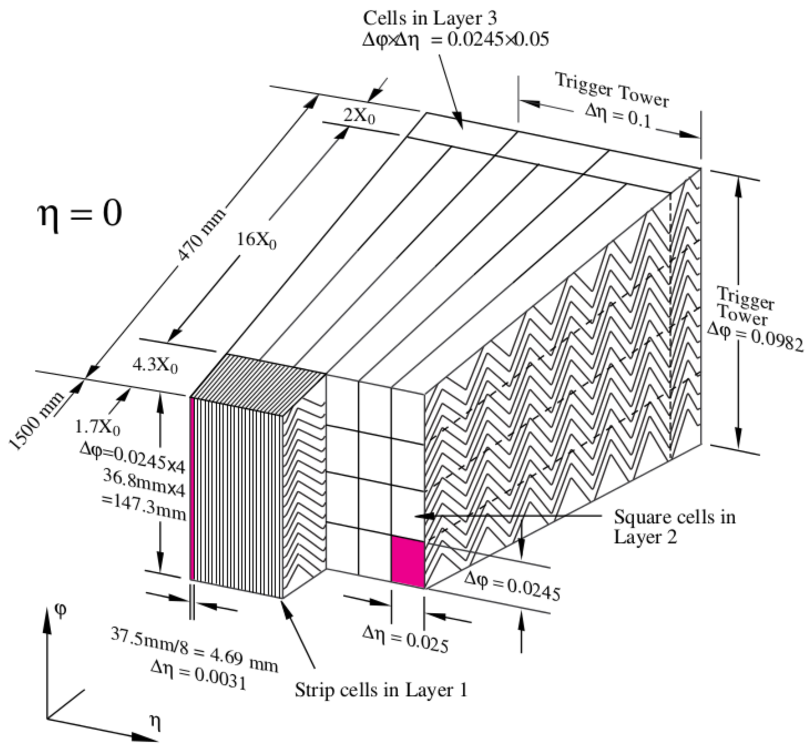

Figure 3.6: A cross-section of the ATLAS Electromagnetic calorimeter

3.2.4 Hadronic Calorimeter

The ATLAS hadronic calorimeter (often referred to as the HCal or TileCal) lies beyond the ECal. A small section of the HCal is shown in Figure 3.7. Similar in mechanism to the ECal, the HCal is made of iron absorber plates and uses two polystyrene based scintillators and an additional PVT based scintillator (rather than the lead-LAr combination of the ECal).

Unlike photons, electrons, and muons, hadronic particles lose most of their energy via strong interactions (rather than bremsstrahlung radiation). First, energetic secondary hadrons are produced from a collision of the incoming hadron. The exact characteristics of the secondary hadrons are highly variable and have a significant effect on the deposition of energy; for example, neutral pions are short-lived particles and will result in the next part of the shower "chain" happening quickly (because they decay via $\pi^0 \rightarrow \gamma\gamma$ - which then proceeds to deposit energy quickly just as in the ECal), while the long-lived neutrons will cause the energy to be deposited over a greater distance, possibly resulting in additional "tertiary" hadrons or such a time delay in energy deposition that its fraction of the energy is simply not collected by the detector. This effect limits the resolution of any hadronic calorimeter. [39]

While the name of the hadronic calorimeter implies it captures all the energy of hadronic particles in most cases the majority of the particle energy is collected by the electromagnetic calorimeter. Hadronic particles merely produce longer showers and therefore deposit more energy in the hadronic calorimeter than electrons and photons. A simple illustration of this is shown in Fig **??** and in atmospheric simulations in Fig 3.8.

3.2.5 Muon Spectrometer

The ATLAS Muon Spectrometer (MS) lies beyond the HCal and makes up the largest volume of the detector (shown in Figure 3.9). The system consists of several detectors (drift tubes, strip detectors) which function similarly to those discussed in the tracking section. This region also has a toroidal magnetic field used to cause the muons to curve and thus their charge and momentum can be determined. Unlike in the calorimeters, the muons are not stopped by their interaction with the detector. At this distance from the ID, muons are the only charged Standard Model particles which haven't been absorbed by the inner layers of the detector - resulting in a great identification.

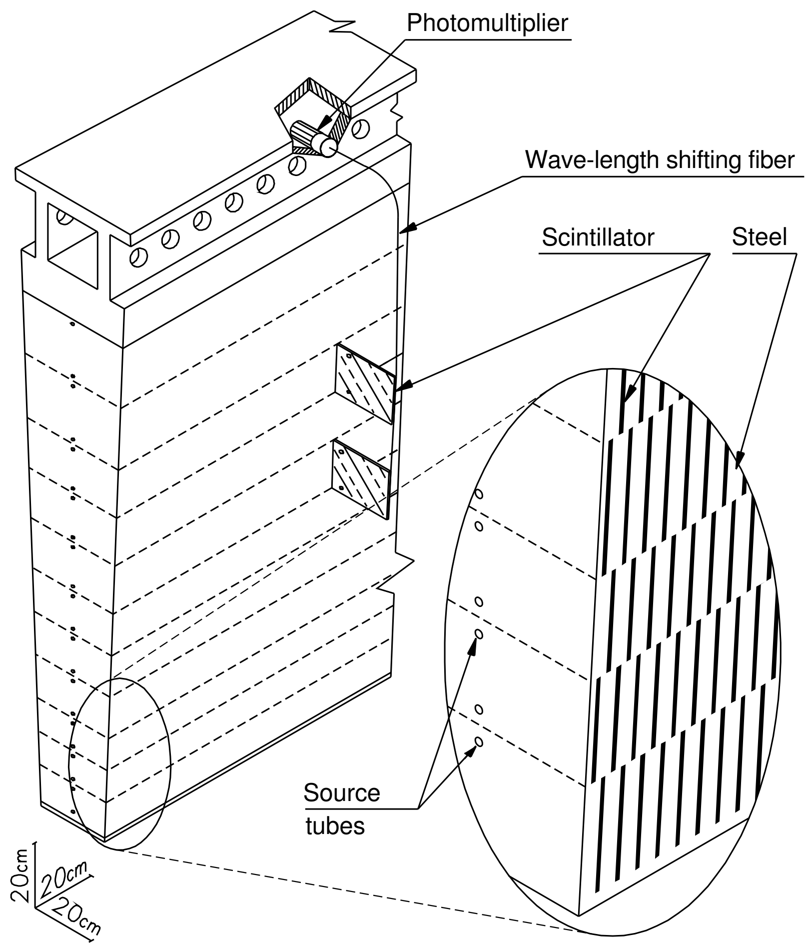

Figure 3.7: A cross-section of the ATLAS Hadronic calorimeter (TileCal)

3.2.6 Triggering And Data Acquisition

The LHC collides bunches of protons at a rate of 40 MHz; however to save the results of each of these interactions would require writing 60 TB of data every second - which is impractical both in terms of the storage space and the data bandwidth. Because of this the detector records only a small fraction of events and special hardware (called triggers) are used to pick events most useful for analysis.

Some events are so rare that every single one can be saved (for example events with a very high energy muon). Triggers for such events are said to be 'unprescaled'. Prescaled triggers are ones which are saved only some of the time, for example, a trigger with a prescale of 3 saves 1 out of

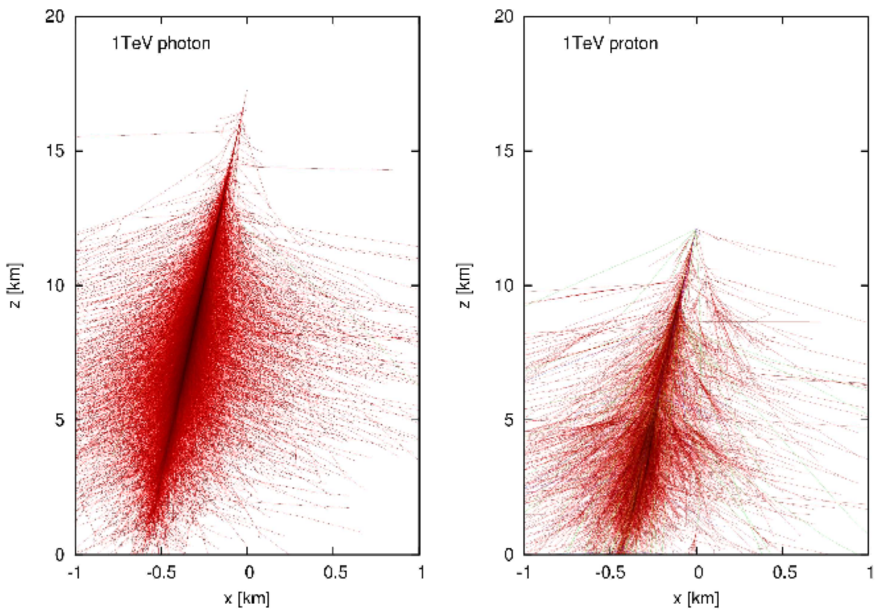

Figure 3.8: Two examples of simulated extended air showers developed in the Earth's atmosphere . Each line represents the path of an elementary particle created during the shower evolution. The left panel presents the shower generated by a single photon of energy 1TeV, while the right panel shows the shower originating from a single proton of the same energy[23]. Note how the proton shower takes longer to evolve, depositing more of its energy deeper in the atmosphere. These showers evolve much more quickly within the dense material of calorimeters.

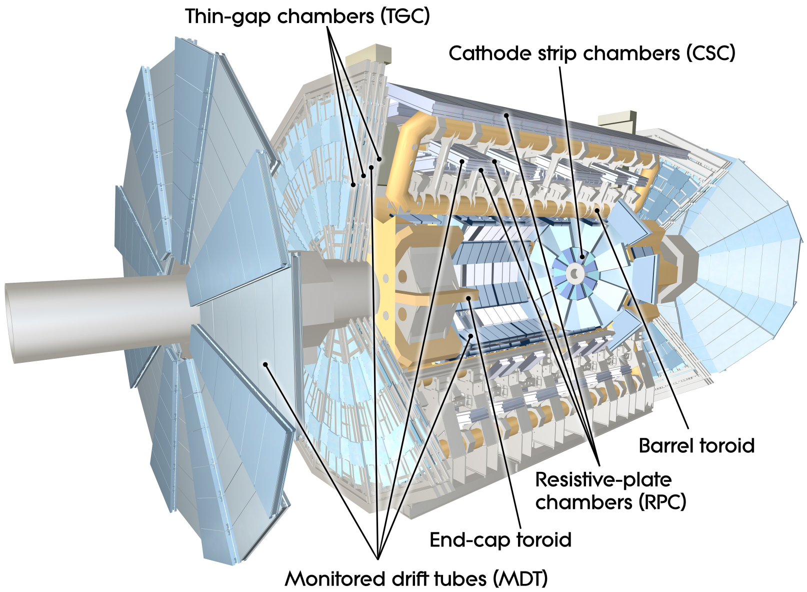

Figure 3.9: A cross-section of the ATLAS Muon Spectrometer (MS)

every 3 events which fires it. Analysis teams must identify triggers which work for their analysis - as well as perform studies on how efficient the trigger is for selecting their events.

3.2.7 Luminosity Measurement

To measure a cross-section it is important to measure the actual luminosity delivered by the LHC to the ATLAS detector. Generally the luminosity is given by

$$\mathcal{L} = \frac{\mu n_b f_r}{\sigma_{inel}} \tag{3.1}$$

where μ is the number of interactions per bunch crossing, $n_b f_r$ is the number of bunches crossing per unit time. The dominant technique for measurement relies on counting events via different detectors, which means that the measurement is really based only on the number of visible events and is thus written

$$\mathcal{L} = \frac{\mu n_b f_r}{\sigma_{inel}} = \frac{\mu^{vis} n_b f_r}{\epsilon \sigma_{inel}} = \frac{\mu^{vis} n_b f_r}{\sigma_{vis}} \tag{3.2}$$

The event counting techniques are calibrated using measurements inferred from accelerator parameters. The absolute luminosity is given by

$$\mathcal{L} = \frac{n_b f_r n_1 n_2}{2\pi \Sigma_x \Sigma_y} \tag{3.3}$$

where n_1 and n_2 are the numbers of particles in the two colliding bunches and Σ_x and Σ_y characterize the widths of the horizontal and vertical beam profiles. The beam profile widths are measured using van der Meer (vdM) scans where one beam is steered across another which is held stationary and the energy collected by various detectors is monitored [6]. The luminosity can be measured using the ECal, however there exist several specialized detectors to perform this measurement with greater coverage. These detectors include the Minimum Bias Trigger Scintillators (MBTS), the Luminosity measurement using Cerenkov Integrating Detector (LUCID), the Zero Degree Calorimeter (ZDC), and the Absolute Luminosity For ATLAS (ALFA) [54].

The basic unit of storing luminosity information is called a Lumi-block (LB) and corresponds to about 2 minutes. All data quality information is stored alongside the corresponding lumiblock, which is later used to select which LBs to use for analysis, called the “Good Runs List” (GRL).

3.2.8 Pileup

Due to the fact that in each bunch crossing multiple protons can interact, so-called ’pileup’ events need to be separated from the events of interest. The majority of proton-proton collisions result in low energy hadronic jets. Several measures are taken to properly account for pileup in events. The tracking system can be used to determine the vertex with the largest transverse momentum (largest Σp_T^2) and jets without tracks coming from this vertex may be presumed to be pileup jets and therefore ignored (see Section 4 for more details).

The rate of pileup events is directly related to the luminosity of the beam and the known cross-section of inelastic collisions ($\sigma_{inel} = 80$mb at $\sqrt{s} = 13$TeV [1]).

$$R_{inel} = \mathcal{L}\sigma_{inel} \tag{3.4}$$

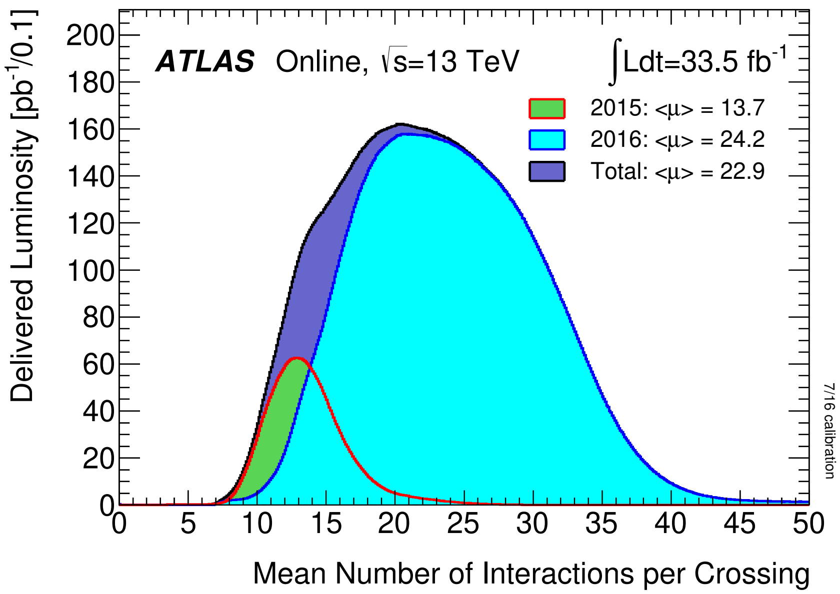

Figure 3.10: The mean number of interactions in the ATLAS detector in 2015+2016 data.

This interaction rate is measured using the Min-Bias Trigger System (MBTS)[7]. From this the average number of interactions per bunch crossing, called μ, can be computed as

$$\mu = \frac{R_{inel}}{n_{bunch} f_{cross}} \tag{3.5}$$

where n_{bunch} is the number of proton bunches and f_{cross} is the frequency of the collisions (which is 25ns). The mean number of interactions per bunch crossing in 2015 and 2016 are shown in Figure 3.10. From this figure it is clear that the instantaneous luminosity of the beam was increased in 2016, resulting in a much larger number of pileup events[**?**].

To account for situations where pileup is not distinguishable from true signal events, pileup information is included in physics simulations and thus must be subsequently reweighted to match the pileup distribution in data [26]. This reweighting procedure is a possible source of systematic uncertainty which will be discussed further in Section 8.4.

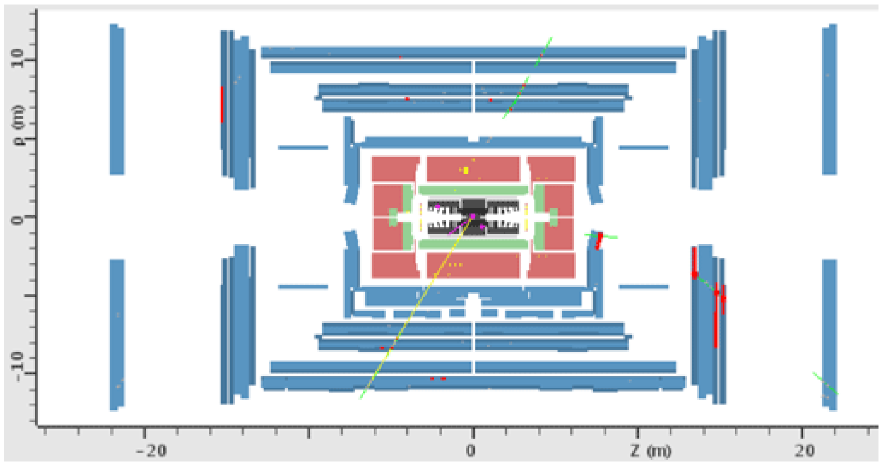

Figure 3.11: An ATLAS event display from 2010 showing a cosmic muon entering from the top of the detector (shown as a green line) and depositing energy in the hadronic calorimeter [50].

3.2.9 Cosmic Rays And Beam Induced Backgrounds

Cosmic rays often result in high energy showers of particles in Earth's upper atmosphere. Each minute, 10,000 muons per square meter reach the surface. Occasionally these muons are energetic enough to register in the ATLAS detector. An example of an event containing a cosmic muon registered by the detector is shown in Fig 3.11.

The proton beams of the LHC confine the protons to their bunches as much as possible, however some may separate from the beam (this is called 'beam halo'). Occasionally protons within the halo collide with the collimators which focus the beam - resulting in a *pp* collision event originating far outside of the detector. The resulting sprays are largely parallel to the beamline and may travel into the detector - leaving energy in various systems. This is often referred to as "Beam Induced Background" (BIB). An example of a BIB event is shown in Fig 3.12.

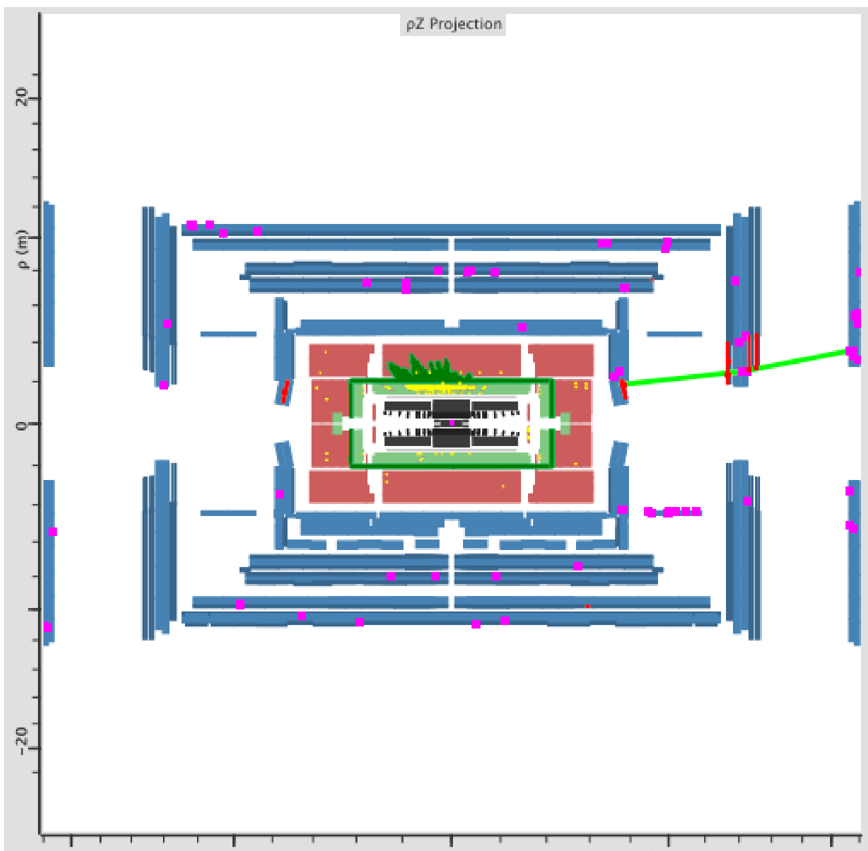

Figure 3.12: An ATLAS event display showing a large energy deposit in the calorimeters made by a muon traveling nearly parallel to the beamline.

CHAPTER 4. OBJECT RECONSTRUCTION

Events are required to have at least one primary vertex that has at least two associated tracks, each with transverse momentum $p_{\mathrm{T}} > 400\mathrm{MeV}$. If there is more than one primary vertex reconstructed in the event, the one with the largest track $\sum p_{\mathrm{T}}^2$ is chosen as the hard-scatter primary vertex and is subsequently used for calculation of the main physics objects in the analysis: electrons, muons, jets and missing transverse energy ($E_{\mathrm{T}}^{\mathrm{miss}}$). The definitions of those physics objects are summarized in the following sections.

Many objects have some kind of requirement to ensure that they come from the chosen primary vertex. This is determined using two inner tracking criteria : the transverse and longitudinal impact parameters, illustrated in Fig 4.1. These parameters are defined relative to the position of the PV.

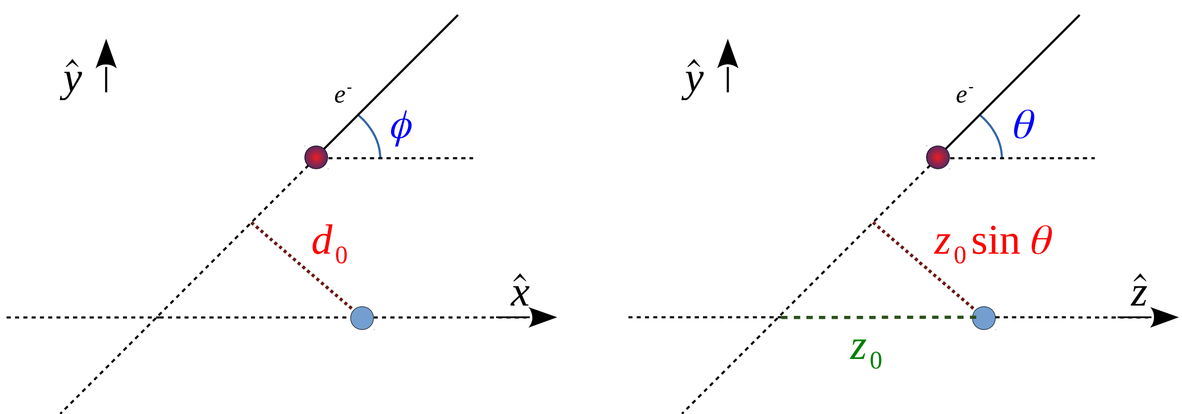

Figure 4.1: The definitions of the transverse impact parameter (d_0) and the longitudinal impact parameter ($z_0 sin\theta$)

4.1 Electron

Electron candidates are identified by matching clusters of deposits in the EM calorimeter with tracks from the ID. The energy cluster is determined using a sliding window algorithm [45]. In this approach the calorimeter is divided into a grid of $N_\eta \times N_\phi$ elements (200×256 for the ATLAS detector). The total energy of each element in all layers of the calorimeter is summed, creating a "tower". A window of fixed size $N_\eta^{window} \times N_\phi^{window}$ in units of towers is moved across the tower grid. If the transverse energy of all towers within the window pass a threshold E_T^{thresh} (2.5 GeV for the ATLAS EM calorimeter) it is used as a "seed" for the clustering algorithm. Cluster reconstruction is very efficient for true electrons. In MC simulations, the efficiency is about 95% for electrons with a transverse energy of $E_T = 7GeV$ and reaches 99% at $E_T = 15GeV$ and 99.9% at $E_T = 45GeV$, placing a requirement only on the angular distance between the generated electron and the reconstructed electron cluster. The efficiency decreases with increasing pseudorapidity in the endcap region $|\eta| > 1.37$ [52, 12], shown in Fig 4.2.

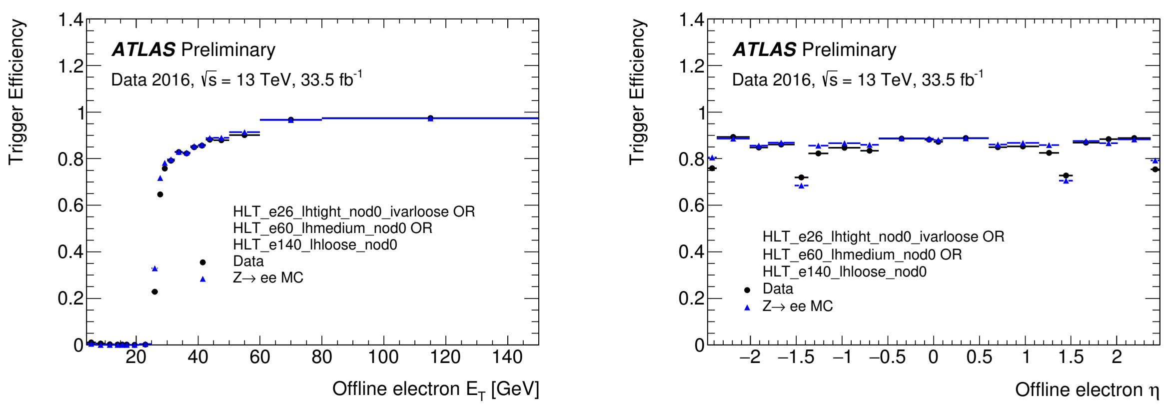

Figure 4.2: Efficiency of the HLT e26_lhtight_nod0_ivarloose trigger as a function of the offline electron candidate's transverse energy (E_T) and pseudorapidity (η). The Level-1 (L1) trigger requires an isolated electromagnetic cluster with $E_\mathrm{T} > 22$GeV. The HLT e26_lhtight_nod0_ivarlooose trigger requires an electron candidate with $E_\mathrm{T} > 26$GeV satisfying the likelihood-based tight identification without applying transverse impact parameter requirements but applying variable-size cone isolation. For physics analysis the trigger is Red with higher E_T-threshold triggers applying looser identification criteria. The offline reconstructed electron is required to pass a likelihood-based tight identification and be isolated. The efficiencies were measured with a tag-and-probe method (see Appendix C for details on the tag-and-probe method) using $Z \to ee$ decays in data and Monte Carlo. The error bars show the statistical uncertainties. [52]

For each cluster which passes loose shower shape requirements a region of interest (ROI) around the cluster with a cone size of $\Delta R = 0.3$ is formed. Track seeds (which have at least 3 hits in different silicon layers) with $p_T > 1GeV$ are tested against pion and electron pattern recognition algorithms are required to lie inside the cluster ROI. A track fit is used to extrapolate the track to the calorimeter using the cluster momentum and the track momentum separately. If either succeeds then the final track reconstruction is done using a Gaussian Sum Fitter (GSF).

After calibrations and corrections are applied, the four momentum is calculated using the energy measurement of the cluster and the η and ϕ measurements from the track.

This procedure does not completely exclude other physics objects from being reconstructed as electrons, including hadronic jets, non-prompt electrons from photon conversions, and semi-leptonic decays of hadrons with heavy quarks. A multivariate analysis (MVA) technique takes into account several cluster and track variables to create a likelihood (LH) identification for each candidate as either signal or background.

Different working points balancing signal efficiency with background rejection are provided. The levels of identification are categorized as "LooseLH", "MediumLH" and "TightLH" corresponding respectively to 96%, 94% and 88% identification efficiencies for signal electrons at $E_{\mathrm{T}} = 100\,\mathrm{GeV}$.

An electron from a W or Z boson decay will be produced relatively isolated while jets, converted photons, and other fake electron objects will have other nearby energy deposits. Isolation is measured for each candidate in both the calorimeter and the tracking system. The calorimeter isolation ($E_T^{cone0.2}$) calculates the sum of E_T within a cone with $\Delta R < 0.2$ around the center of the cluster, subtracting the 5×7 cell window contribution from the electron. Track isolation is determined similarly from the transverse momentum of tracks $p_T^{varcone0.2}$ within a cone of variable size $\Delta R < min(0.2, 10GeV/E_T)$.

The identification and isolation working points are optimized for electrons coming from the PV, and in this analysis the leptons are crucial for the proper identification of the PV. For these reasons we additionally impose cuts on the longitudinal (z_0) and transverse (d_0) impact parameters to verify that the electron indeed comes from the PV. Electrons are required to have $|\eta| < 2.47$, excluding the transition region between the barrel and endcap EM calorimeter ($1.37 < |\eta| < 1.52$) in which uncertainties are known to be very large.

Finally, a minimum p_T threshold is set above trigger threshold to avoid large uncertainties from the trigger turn-on curve.

The identification requirements used for this analysis are summarized in Table 4.1. Two types of electrons are used : ”signal” and ”veto”. Veto electrons are used to avoid contamination from the signal region in the control region (this will be discussed further in Section 5).

Table 4.1: The object definitions for electrons used in this analysis are shown. Veto Leptons are defined to reduce signal contamination of the control region. Due to the change of triggers from 2015 to 2016 the p_{T} cut used was increased slightly to 27 GeV.

Cut	Veto Electron	Signal Electron
$p_T^{min}[GeV]$	7	25(27)
$\|\eta\|$	$< 2.47 \notin [1.37, 1.52]$	
Identification	LooseLH	MediumLH
Isolation	GradientIsolated	
$\|d_0/\sigma(d_0)\|$	< 5	
$\|z_0 sin\theta\|[mm]$	< 0.5	

The electron reconstruction efficiency and MC scale factors are determined using the tag-and-probe method (see Appendix C for details on the tag-and-probe method). Samples of $J/\psi \rightarrow ee$ and $Z \rightarrow ee$ events are used to obtain relatively pure samples of electrons. The backgrounds in these samples is estimated using combined template fits. The efficiency, shown in Fig **??**, is then defined by the number of probe electrons passing the selection.

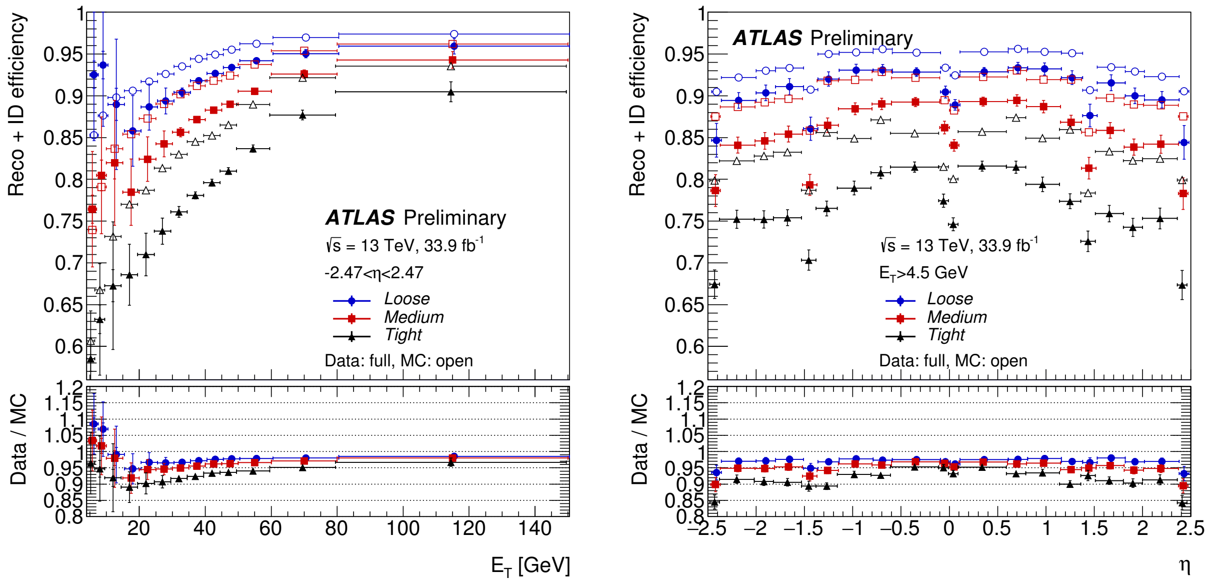

Figure 4.3: Electron reconstruction and identification efficiencies in $Z \to ee$ events as a function of η and E_{T}, for electrons with $E_{\mathrm{T}} > 4.5$ GeV. The efficiencies are shown in data and MC for three operating points that are based on a likelihood approach, Loose, Medium and Tight. The data effciencies are obtained by applying data/MC efficiency ratios that were measured in $J/\psi \to ee$ and $Z \to ee$ events to MC simulation. A dataset corresponding to an integrated luminosity of 33.9 fb^{-1} that was recorded by the ATLAS experiment in the year 2016 at a center-of-mass energy of $\sqrt{s} = 13$ TeV was used. Both the likelihood based electron identification algorithms and the measurement of efficiencies are described in [17].

4.2 Muon

In the MS, hits collected by the MDTs [34] are checked for a trajectory along a straight line, forming "segments". Segments are determined separately by the CSC detectors using a specialized search algorithm. Muon track candidates are then constructed by combining the segments from multiple layers, removing some hits as needed to improve the quality of the fit. At least two matching segments are required to construct a track (except in the barrel-endcap transition region where 1 high quality segment will suffice).

Muon objects are reconstructed by matching track candidates independently created in the MS and ID [19]. There exist four types of muon candidates, each of which combine the information from different detectors with different algorithms.

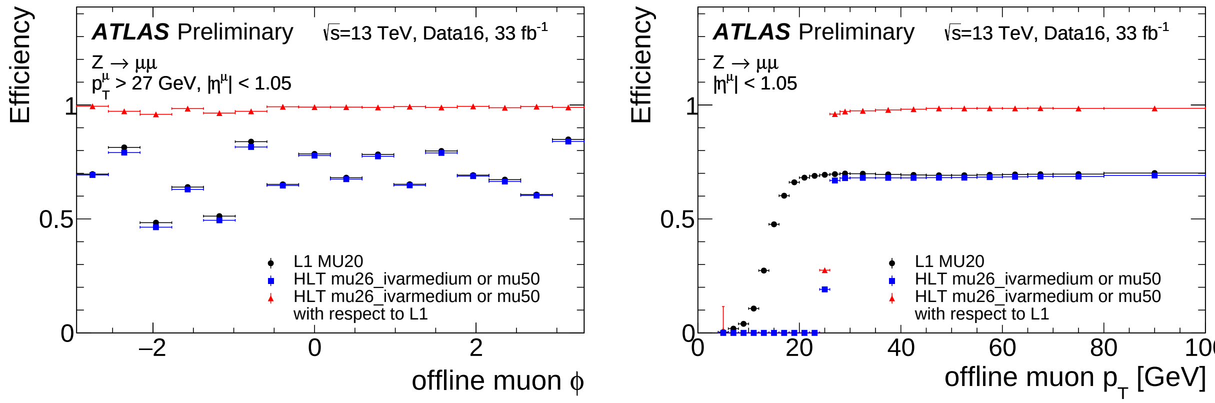

Figure 4.4: Absolute efficiency of Level 1 (L1) MU20 trigger and absolute and relative efficiencies of the OR of mu26_ivarmedium with mu50 High Level triggers (HLT) plotted as a function of p_{T} and η of offline muon candidates in the barrel detector region. The efficiency is computed with respect to offline isolated muon candidates which are reconstructed using standard ATLAS software and are required to pass Medium quality requirement. The MU20 trigger requires that a candidate passed the 20GeV threshold requirement of the L1 muon trigger system. The mu26_ivarmedium trigger is seeded by the MU20 trigger and is required to satisfy a 26GeV HLT threshold and to pass a medium isolation selection computed using inner detector tracks reconstructed online by the HLT within a cone with a variable size which depends on the p_{T} of the muon. The mu50 trigger is seeded by MU20 at L1 and is required to satisfy a p_{T} threshold of 50GeV. The efficiency is measured using a tag-and-probe method with $Z \rightarrow \mu\mu$ candidates, with no background subtraction applied, in 13TeV data from 2016 with 25ns LHC bunch spacing. Only statistical data uncertainties are shown. [34]

- **Combined (CB) :** Track reconstruction is performed independently in the MS and ID. The full muon track is reconstructed by combining these tracks, starting in the MS and extrapolating inward, towards the ID.

- **Segment-Tagged (ST) :** Track reconstruction is performed in the ID and then extrapolated towards the MS, where it must match at least one MDT/CSC track segment (useful for low-p_T muons).

- **Calorimeter-Tagged (CT) :** Track reconstruction is performed in the ID. The track is then extrapolated to the calorimeter, where it matches an energy deposit. This type is the least pure type of muon, but is useful in the region $|\eta| < 0.1$ where the MS has no coverage.

- **Stand-Alone (SA) :** Track reconstruction is performed in the MS and when extrapolated must fall close to the IP. This used to recover muons in the range $2.5 < |\eta| < 2.7$ which has poor ID coverage.

Using the four types of muon candidates and additional cuts on tracking and calorimetry variables, several working points are available offering different background rejection, namely "Very-Loose", "Loose", "Medium" and "Tight". In this analysis Medium and Loose working points are used, corresponding to efficiencies of 96.1% and 98.1% respectively.

The Medium working point uses only CB and SA muons while the Loose working point uses all four types. CB muons are required to have ≥ 3 hits in at least 2 MDT layers, except for tracks in the $|\eta| < 0.1$ region, while SA muons are required to have hits in at least 3 MDT/CSC layers. SA muons are only used outside the area covered by the ID, $2.5 < |\eta| < 2.7$. The Loose working point includes all muons in the Medium working point. In addition it includes CT and ST muons in the range $|\eta| < 0.1$

Muon isolation is determined similarly to electron isolation: both tracking and calorimeter based isolation measurements are used to create working points. The track based muon isolation uses a larger cone size than the electron case, $\Delta R < 0.3$.

Finally, as with electrons, two types of muons are defined for this analysis, "signal" and "veto". The object definitions are summarized in Table 4.2.

Table 4.2: The object definitions for muons used in this analysis are shown. Veto muons are defined to reduce signal contamination of the control region. Due to the change of triggers from 2015 to 2016 the p_{T} cut used was increased slightly to 27 GeV.

Cut	Veto Muon	Signal Muon
$p_T^{min}[GeV]$	7	25(27)
$\|\eta\|$	< 2.4	
Identification	Loose	Medium
Isolation	GradientIsolated	
$\|d_0/\sigma(d_0)\|$	< 3	
$\|z_0 sin\theta\|[mm]$	< 0.5	

The muon reconstruction efficiency and MC scale factors are determined using the tag-and-probe method and are shown in Figure 4.5 (see Appendix C for details on the tag-and-probe method). Decays of $J/\psi \to \mu\mu$ and $Z \to \mu\mu$ are easily selected, pure samples of muons. The muon reconstruction efficiency is shown as a function of muon p_{T} in Figure 4.5.

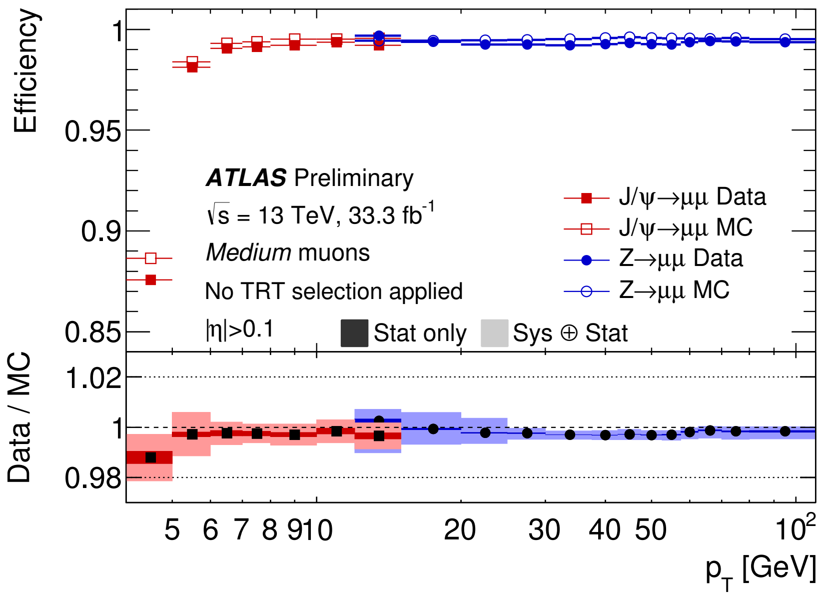

Figure 4.5: Muon reconstruction efficiencies for the Medium identification algorithm measured in $J/\psi \to \mu\mu$ and $Z \to \mu\mu$ events as a function of the muon momentum. Only statistical errors are shown in the top panel. The bottom panel reports the efficiency scale factors. The darker error bands indicate the statistical uncertainty, while the lighter bands indicate the quadratic sum of statistical and systematic uncertainties.

4.3 Jet

As discussed in Section 2.1.3, quarks and gluons from pp collisions undergo a process called hadronization quickly after being separated, forming a large variety of mesons and baryons all with their own properties. When a quark or gluon has a high momentum the hadronization process can produce several particles in the same direction. With such wide variety of possible particles with different properties in such a small space it becomes exceptionally difficult to distinguish all of the "daughter" particles from one-another. For this purpose the ATLAS detector utilizes the concept of a "Jet".

A Jet is formed when the daughter particles all lie within a single small cone inside the detector. While the energy and momentum of each individual particle within the cone can't be determined, the total energy and momentum (corresponding to the total energy and momentum of the initiating parton) can. The process of measuring the energy within a cone is complicated by a number of possible factors, including but not limited to :

- **Dead Material :** There are several components of the detector which are not part of a measuring device (structural components responsible for holding the apparatus together, for example). When particles travel through this material and deposit energy it will not be detected, resulting in a lower measurement than the true energy. This material is distributed unevenly throughout the detector, so care must be taken to treat each region of the detector properly.

- **Leakage :** As discussed in Sec 3.2.4, hadronic showers can penetrate far deeper into a calorimeter than their electromagnetic counterparts. It is possible for some showers to "punch through" the calorimeter, leaving some energy uncollected.

- **Noise Thresholds :** The electronic measuring devices used in the detector produce a certain level of noise, which appears as low energy fluctuations in the calorimeter. Particles produced with energies at or below these noise levels blend in with the noise of the detector and cannot be easily separated.

- **Pileup :** As discussed in Sec 3.2.8 the ATLAS detector produces many pp collisions at each bunch crossing. These pp collisions tend to produce many low energy jets, which leave energy in the detector, possibly overlapping with objects of interest (and therefore increasing the measured energy).

Jets are reconstructed from three-dimensional topological EM calorimeter energy clusters using the anti-k_t algorithm [46] with a distance parameter (cone size) of $\Delta R = 0.4$. All selected clusters contain a significant amount of energy relative to known noise values. The jet energies are then corrected [10] for detector inhomogeneities, the non-compensating nature of the calorimeter, and the impact of multiple overlapping pp interactions. Correction factors are derived using test beam, cosmic ray, pp collision data, and a detailed Geant4 detector simulation. Energy deposits are assumed to have come from massless particles originating from the center of the detector. The 4-momentum of all clusters can then be added together to determine the p_{T} of the jet. Only jets with a $p_{\mathrm{T}} > 7$ GeV and $|\eta| < 4.5$ are used for calibration. Calibration begins with choosing the proper origin for the jet, usually the primary vertex (PV) and recalculating the 4-momentum. The z-coordinate of the beamspot varies considerably (with a luminous region of $40 - 55$ mm in 2012) and so the ϕ coordinate is less resolved than the θ coordinate of the transverse plane [15].

To correct for the extra energy deposited by pileup events, the average energy density of pileup jets (energy per unit area) was measured as a function of the number of primary vertices N_{PV} and the average number of interactions $\langle\mu\rangle$. The area of jets is then measured using ghost particles (see the later section on track association Sec 4.3.1) and the average energy contributed from pileup is subtracted.

Next the effect of leakage is corrected for by sequentially adjusting the measured energy based on the fraction of jet energy in the first layer of the calorimeter, the fraction in the third layer, the track multiplicity, and the amount of activity measured in the MS behind the jet.

Lastly, the in-situ calibration is performed using jets recoiled against known physics objects which can be measured with relatively high precision ($Z \to \ell\ell + Jet$, $\gamma + Jet$, and even dijet events). These calibrations introduce relatively large uncertainties for all ATLAS analyses using jets and are further described in Sec 8.

4.3.1 Ghost Track Association

The track-jet association is done using a ghost association method [27, 28]. This method creates a "ghost" track for each measured track with 0 energy and the same η,ϕ. These tracks are appended to the list of jet constituents and then the jet clustering algorithm is run. Because each ghost track corresponds to a real track the number of ghost-associated tracks matches the number of real tracks associated with the jet, but without the energy of the tracks modifying the clustering. The ID tracks used as the input of the association are required to have $p_{\mathrm{T}} > 1\,\mathrm{GeV}$ and $|\eta| < 2.5$. In addition, the tracks must have at least 7 hits in total in the pixel and SCT detectors, not more than one hit in the pixel detector shared by multiple tracks, not more than one missing hit in the pixel detector when it is expected, and not more than two missing hits in the SCT detector. The longitudinal impact parameter z_0 of the tracks is required to be $|z_0 \sin\theta| < 3\,\mathrm{mm}$, where measurements are made with respect to the location of the primary vertex.

4.3.2 CalRatio (CR) Jets

When a long lived neutral particle decays inside the HCal it can result in a reconstructed jet which has no associated charged tracks and a large fraction of its energy in the HCal. Such jets are referred to as "CalRatio" (CR) jets [13, 55] and are defined as follows.

- Jet $E_{\mathrm{T}} > 40\mathrm{GeV}$ and $|\eta| < 2.0$. For higher mass samples this E_{T} cut is increased to provide better sensitivity, described in Section 9 and Fig 4.9.

- Jets with $E_{\mathrm{T}} < 60\mathrm{GeV}$ are also required to lie outside the region of the Gap Scintillator $1.0 > |\eta| > 1.3$ (shown in Fig 6.2) to avoid an effect due to noise detailed further in Sec 6.

- $\log_{10}(\frac{1-EMF}{EMF}) > 1.2$ (referred to as *logRatio*), where EMF is the fraction of the jet energy deposited in the ECal ($EMF = \frac{E_{ECal}}{E_{ECal}+EHCal}$). The distribution of this variable in jets passing all other CR jet cuts in W+Jets data and signal MC is shown in Fig 4.6.

- There are no tracks with $p_{\mathrm{T}} > 1\mathrm{GeV}$ associated with the jet. The distribution of this variable in jets passing all other CR jet cuts in W+Jets data and signal MC is shown in Fig 4.7.

- $-3\mathrm{ns} < \mathrm{JetTiming} < 15\mathrm{ns}$ where the jet timing is obtained as the averaged time of all cells weighted by the square of cell energy with respect to the global event timing. The distribution of this variable in jets passing all other CR jet cuts in W+Jets data and signal MC is shown in Fig 4.8.

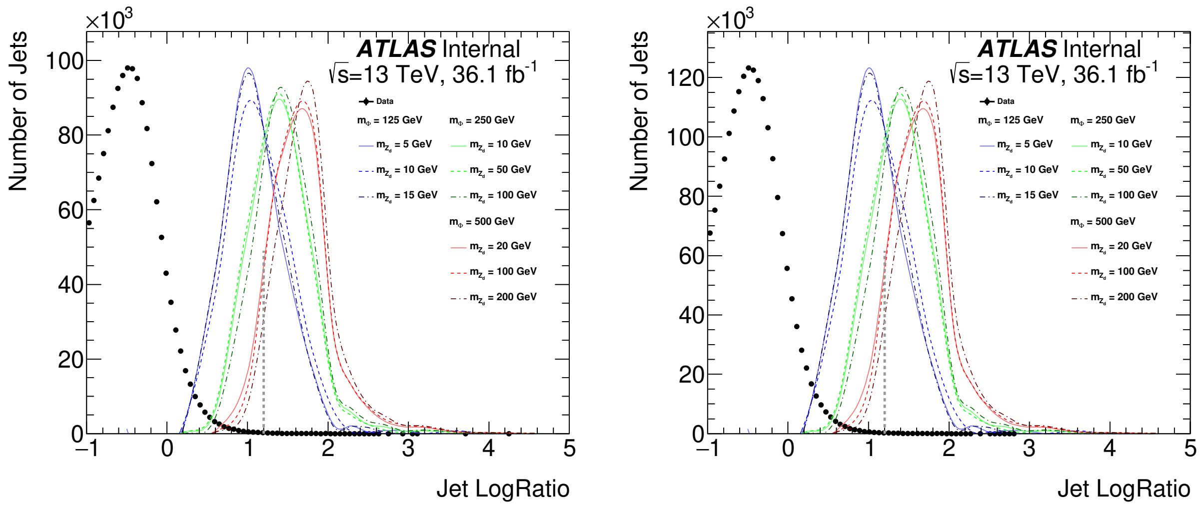

Figure 4.6: The value of $log_{10}(\frac{1-EMF}{EMF})$ of all jets in W+jets data compared to the value for truth CR jets in the signal MC for the electron channel (left) and muon channel (right). Plots are shown after all selections have been applied *except* the cut on this variable which is indicated by the vertical gray lines.

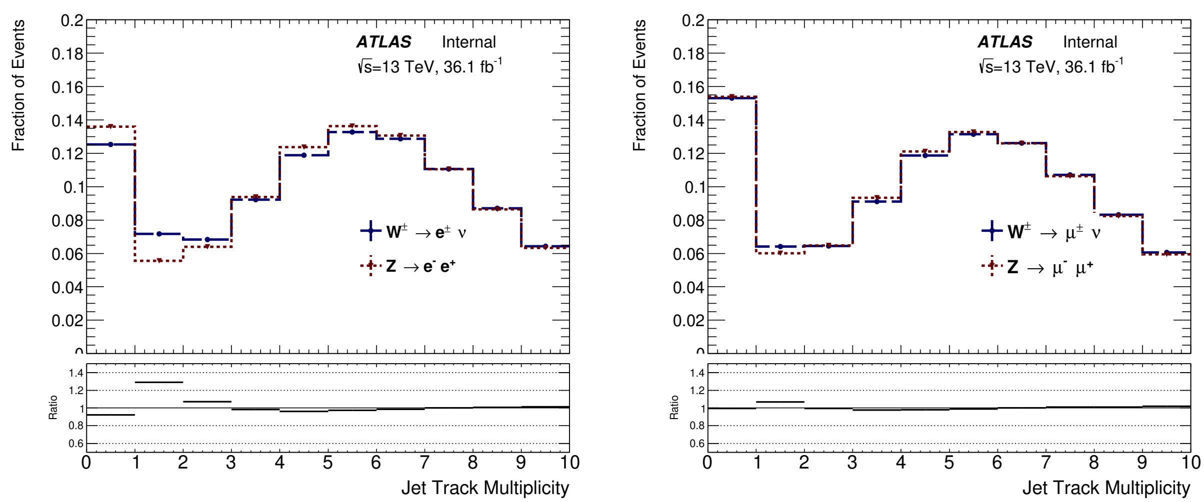

Figure 4.7: The track multiplicity of all jets with $log_{10}(\frac{1-EMF}{EMF}) > 1.2$ and $E_{\mathrm{T}} > 40\mathrm{GeV}$ in W+jets data compared to signal jets in MC. We consider the contribution from signal to be negligible above 2 tracks.

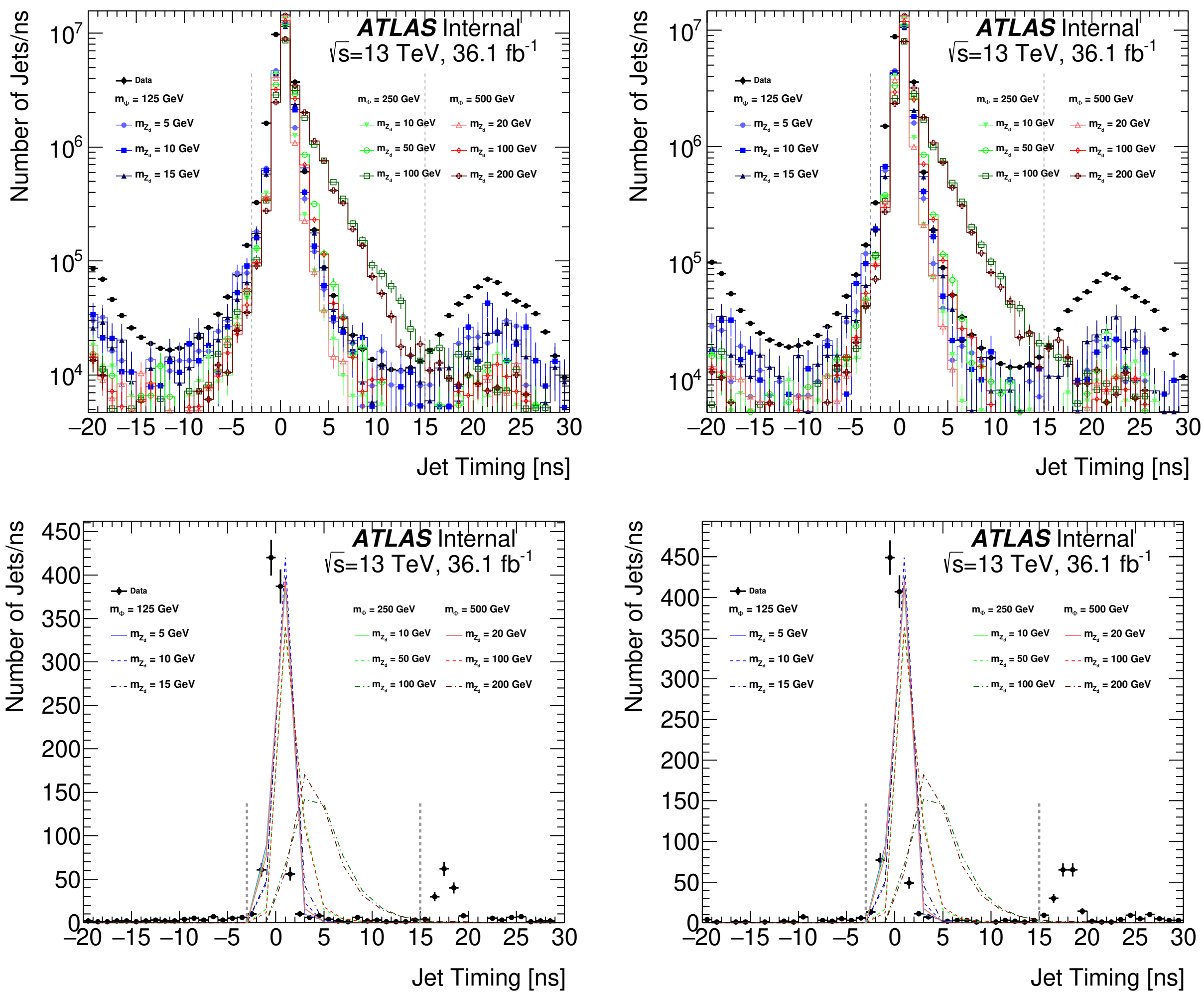

Figure 4.8: The jet timing of all jets in W+jets data compared to the jet timing of truth CR jets in the signal MC for the electron channel (left) and muon channel (right). This variable is shown prior to selection (top) and after all selection *except* the timing cut (bottom). The cuts are indicated by the dashed vertical gray lines. The two least boosted samples (with $m_\Phi = 250\text{GeV}, m_{Z_d} = 100\text{GeV}$ and $m_\Phi = 500\text{GeV}, m_{Z_d} = 200\text{GeV}$) have Z_d which travel slowly and thus take longer to reach the HCal before their decay, resulting in a larger value of jet timing.

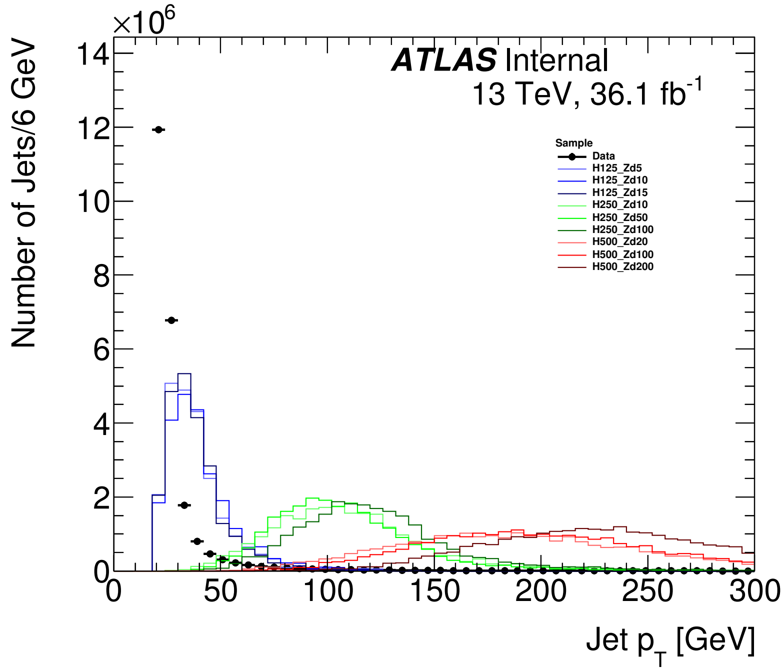

Figure 4.9: The E_{T} spectrum of all signal jets in signal MC compared to all baseline jets in W+Jets data. For each signal sample the chosen E_{T} cut was selected to optimize the sensitivity : at 40 GeVfor $m_{\Phi} = 125$GeV samples, 60 GeVfor $m_{\Phi} = 250$GeV samples, and 80 GeVfor $m_{\Phi} = 500$GeV samples.

The standard jet cleaning cut level associated with the ATLAS jet cleaning tool [16], 'LooseBad', contains cuts on jets with very low ECal activity which would unfortunately remove much of the effect from decays of a neutral LLP in the HCal. The analysis presented here instead uses the cut level 'LooseBadLLP' which contains all of the same cuts as LooseBad except for those that cut on low EMF jets. The criterion also contains two additional cuts intended to reduce the sensitivity to LAr noise bursts, $|negE| < 4$GeV (The sum of all negative energy cells associated with the jet) and $FracSamplingMax > 0.85$ (The maximum fraction of a jet's energy collected in only one layer of the calorimeter).

Typical analyses with jets at ATLAS also utilize the "jet vertex tagger" (JVT) tool to remove pileup jets based on their tracks indicating they originate from another vertex. For this analysis the JVT tool is not applied as it removes trackless jets, which happen to be characteristic of the jets from long lived neutral particles as indicated by Fig 4.7. As such, this analysis is expected to

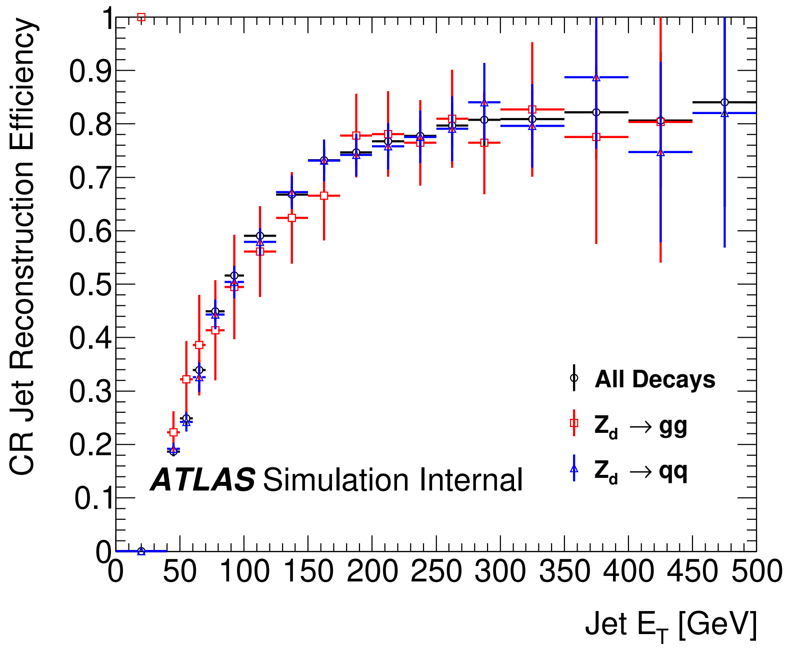

Figure 4.10: The fraction of jets from LLP decays within the volume of the HCal which result in the reconstruction of a CR jet as a function of jet E_{T} for decays of Z_d to both gg and $q\bar{q}$ final states. No significant difference between the final states is observed. To cover the entire E_{T} range shown jets from all signal MC samples are included.

be more sensitive to the effect of pileup jets than most others. In this analysis, preselected jets are required to have $p_{\mathrm{T}} > 20\,\mathrm{GeV}$ and $|\eta| < 2.0$. The choice of η requirement is to ensure the selected jet to be completely inside the tracking system.

The CR jet reconstruction efficiency depends heavily on E_{T} spectrum of the jets and therefore also varies considerably between MC samples. This efficiency can be determined using truth-level information about where in the detector the particle decay occurs. When the decay occurs within the volume of the HCal barrel (with $2.28\mathrm{m} < \mathrm{L_{xy}} < 4.25\mathrm{m}$ from the beamline) then the jet coinciding with the decay (using a $\Delta R < 0.1$ cone match) is marked as a "Truth CR Jet". The fraction of the truth CR jets which pass all CR Jet selection criteria is the CR jet reconstruction efficiency. This efficiency is shown in Fig 4.10 as a function of jet E_{T} and in Fig 4.11 as a function of the LLP decay position L_{xy}.

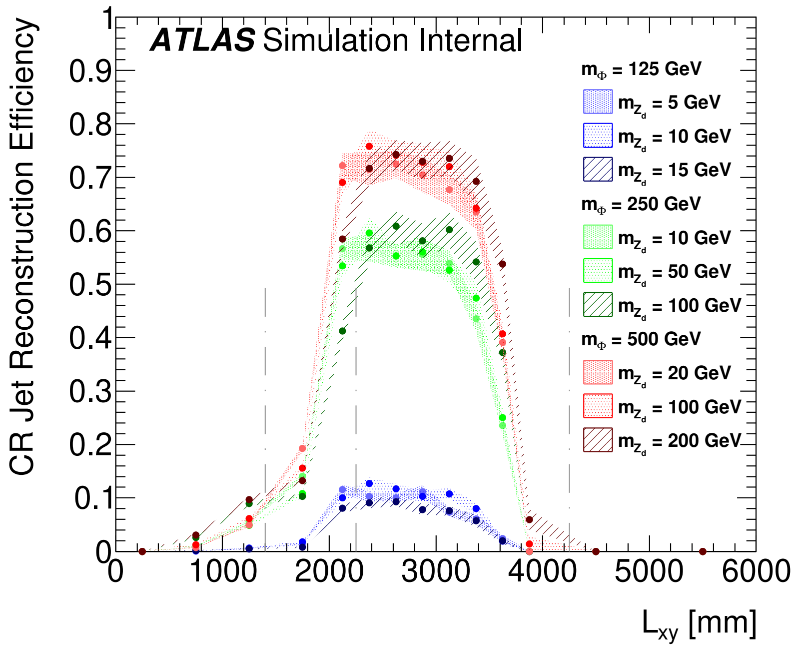

Figure 4.11: The fraction of LLP decays which result in the reconstruction of a CR jet as a function of jet truth L_{xy} for each signal MC sample. The reconstruction begins to become efficient beyond the volume of the tracker (at $L_{xy} \approx 1m$) and becomes maximally efficient within the volume of the HCal (2.28m < L_{xy} < 4.25m). The dashed vertical gray lines indicate the boundaries between the ID and ECal, ECal and HCal, and HCal and MS respectively.

4.4 Object Overlap Removal

Occasionally one or more of these objects will overlap with one-another in the detector. To ensure only good events are selected a procedure is used to isolate the objects of interest. Electrons are discarded if they share ID tracks with selected muon candidates, and the muon is kept. Jets are discarded if they are within a cone of size $\Delta R < 0.2$ around the direction of an electron or muon candidate. Muons within this distance of a jet may be discarded instead, if

- The jet has fewer than three tracks.
- OR $p_{\mathrm{T}}(\mu)/p_{\mathrm{T}}(j) > 0.5$ and $p_{\mathrm{T}}(\mu)/|\sum p_{\mathrm{T}}| > 0.7$, where $\sum p_{\mathrm{T}}$ is the sum of the transverse momenta of tracks associated with the jet.

In the latter case, the muon is retained but the jet is rejected. Additionally, if the distance between a jet and a lepton candidate is within $0.2 < \Delta R < 0.4$ the jet is retained and the nearby lepton is rejected from the analysis. This overlap removal is done by the OverlapRemovalTool and corresponds to the "Standard" configuration for the tool.

4.5 Missing Transverse Energy ($E_{\mathbf{T}}^{\mathbf{miss}}$)

The missing transverse energy, $E_{\mathrm{T}}^{\mathrm{miss}}$, is the absolute value of the negative vectorial sum of the transverse momenta of calibrated objects, such as electrons, muons, and jets. Charged-particle tracks compatible with the primary vertex and not matched to any of those objects are also included in the $E_{\mathrm{T}}^{\mathrm{miss}}$ reconstruction as Track Soft-Terms (TST) [14].

$$E_x^{miss} = -\sum_{e \in "electrons"} p_x^e - \sum_{\mu \in "muons"} p_x^\mu - \sum_{j \in "jets"} p_x^j - \sum_{s \in "softterms"} p_x^s \tag{4.1}$$

$$E_T^{miss} = \sqrt{(E_x^{miss})^2 + (E_y^{miss})^2} \tag{4.2}$$

The use of TST neglects the contribution from neutral particles. A calorimeter soft term (CST) is also available which consists of calorimeter clusters unassociated with objects, however it is very sensitive to pileup conditions and has thus been found to have considerably worse resolution than the TST.

In this analysis $W \rightarrow \ell\nu_\ell$ events are used as a control region and so the $E_{\mathrm{T}}^{\mathrm{miss}}$ represents the transverse energy carried away by the neutrino. However in events with jets semileptonic decays are possible in which the quark initiating a jet decays via the weak interaction shown in Fig 4.12. In this case the daughter quark of the decay continues to produce a hadronic jet, however a lepton and neutrino are also produced, the latter which carries energy away undetected. The frequency of these events are reduced by requiring the leptons to be isolated (i.e. well separated from any jet).

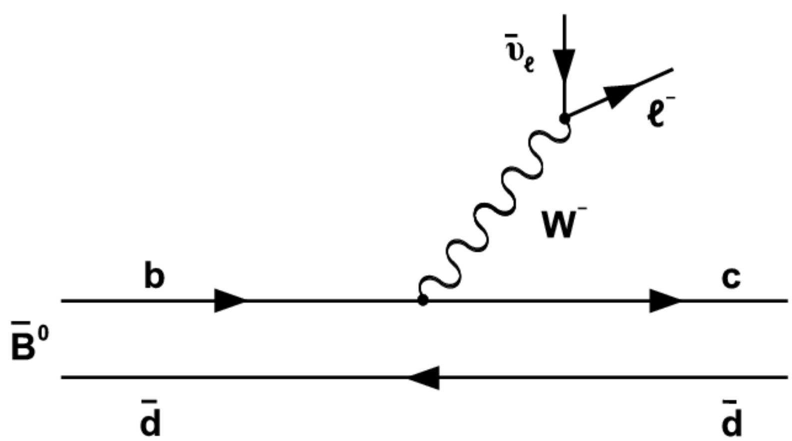

Figure 4.12: The tree-level feynman diagram for the semileptonic decay of a B meson. One of the quarks within the meson undergoes a flavor changing decay via the weak force, resulting in a charged lepton and neutrino.

CHAPTER 5. EVENT SELECTION

This thesis is based on the full dataset from 2015-2016 pp collisions with center-of-mass energy $\sqrt{s} = 13$TeV recorded by the ATLAS experiment.

Only events from "good" lumiblocks are used, as defined in the "Good Runs List" (GRL), corresponding to a total luminosity of 36.1fb^{-1}. These are summarized in Table 5.1.

Table 5.1: The total integrated luminosity $\int \mathcal{L}dt$ and the average number of interactions per bunch crossing in each data-taking period.

Period	max. $\mathcal{L}$ (cm^{-2}s^{-1})	$\int \mathcal{L}dt$ (fb^{-1})	average $\langle\mu\rangle$
2015	0.50×10^{34}	3.21	13.6
2016	1.37×10^{34}	32.86	24.9

5.1 Trigger Selection

The triggers used for this analysis are the lowest threshold unprescaled single-lepton triggers in each data-taking period, in addition to a higher p_{T} trigger for the run which doesn't include an isolation requirement to increase efficiency. The triggers used are summarized in Table 5.2. An additional prescaled trigger was added for the electron channel to increase the statistics in the LooseLH region.

At higher instantaneous luminosities the rates at which triggers fire necessarily increase, and thus in order for a trigger to remain unprescaled the E_{T} threshold had to be increased. The offline selection criteria (detailed in Section 4) were chosen to be 1GeV above the trigger E_{T} thresholds to ensure that any effects from the calibration of lepton p_{T} do not result in widely different efficiencies.

Table 5.2: The list of triggers used in each data-taking period.

Data period	Electron trigger	Muon Trigger
2015	HLT_e24_lhvloose_L1EM20VH OR HLT_e24_lhmedium_iloose_L1EM20VH OR HLT_e60_lhmedium	HLT_mu20_iloose_L1MU15 OR HLT_mu50
2016 A	HLT_e24_lhvloose_L1EM20VH OR HLT_e24_lhtight_nod0_ivarloose OR HLT_e60_lhmedium_nod0	HLT_mu24_ivarloose OR HLT_mu50
B-D3	HLT_e24_lhvloose_L1EM20VH OR HLT_e24_lhtight_nod0_ivarloose OR HLT_e60_lhmedium_nod0	HLT_mu24_ivarmedium OR HLT_mu50
D4-onward	HLT_e26_lhvloose_nod0_L1EM20VH OR HLT_e26_lhtight_nod0_ivarloose OR HLT_e60_lhmedium_nod0	HLT_mu26_ivarmedium OR HLT_mu50

5.2 Event Preselection

Before the analysis selection cuts are applied, a preselection is imposed to reject unwanted events (those with known reconstruction problems). This stage begins with ”event cleaning”, which is standardized for ATLAS analyses.

ATLAS software performs several tests to check the quality of an event which are then recorded along with the data. Among the quality tests are tests for corrupted events or events in which there was a recorded noise burst in some calorimeter cells.

Events are further required to contain a primary vertex (as defined in Section 4) and be present on the ”Good Runs List” (GRL), which is a centrally produced file with information when all parts of the LHC and detector were fully operational and the data quality was good.

Once these event-level cuts are applied, further preselection is performed on the contained physics objects. An event is required to have at least one lepton passing the requirements in Sections 4.1,4.2. This lepton is further required to match the trigger which initially collected this event.

Events are further required to contain at least one baseline jet as defined in Sec 4.3.

5.3 Event Reweighting

As mentioned in Sec 3.2.8, MC simulated events are overlapped with simulated pileup events, using a distribution of what the pileup was expected to be. The true pileup $\langle\mu\rangle$ distribution from events included in the GRL is used to reweight the events in MC so that they properly match the data.

Additionally, weights are applied to MC simulated events to correct for the inefficiencies in object selection. Electrons and Muons have weights applied to correct for reconstruction and isolation efficiencies, as well as the efficiencies of their corresponding triggers (see Section 4 for details).

Finally, MC events are scaled to the total integrated luminosity of the data used.

5.4 Control Events

For this analysis we utilize a $W + Jets$ control region to measure the expected background (from all sources) in our signal region. Events containing a W boson candidate are selected by requiring exactly one lepton passing the object selection criteria, no "veto" leptons, and a $E_{\mathrm{T}}^{\mathrm{miss}}$ of at least 25 GeV. In addition, it is required that transverse mass of the W boson, m_T, be larger than 50 GeV, where m_T is defined as

$$m_T = \sqrt{2 * E_{\mathrm{T}}(\ell) * E_{\mathrm{T}}^{\mathrm{miss}} * (1 - cos(\phi_\ell - \phi_{E_{\mathrm{T}}^{\mathrm{miss}}}))}, \tag{5.1}$$

where $E_{\mathrm{T}}(\ell)$ is the transverse energy of the lepton candidate, ϕ_ℓ and $\phi_{E_{\mathrm{T}}^{\mathrm{miss}}}$ are the azimuthal angle of the lepton candidate and of the missing transverse energy, respectively. The $W \to \ell\nu$ channels contain a significant number of events from the SM multijet production, in which particles are falsely identified as leptons (fakes). Fake electrons originate primarily from jets that have a large electromagnetic energy fraction passing the electron selection requirements, photon conversions, and electrons from heavy-flavor decays. The fake muons include muons arising from semileptonic decays of charm or bottom hadrons (Fig 4.12), in-flight decays of pions or kaons, or energetic particles that reach the muon spectrometer and are thus far less prevalent than the fake electrons.

5.4.1 QCD Multijet Background Estimation

The multijet background for the $W \to \ell\nu$ sample is very difficult to model in MC simulation, therefore a template derived from control data with a modified lepton selection is used to fit the W transverse mass distribution to estimate the contribution. In this method, an enriched multijet sample is constructed by selecting events with exactly one lepton that passes loose identification criteria: the selected electron candidate is required to be "Loose" but not "Medium" quality, and the selected muon candidate is required to pass all the nominal requirements and fail the isolation requirement.

The constructed m_T templates for multijet production in the electron and muon channels are shown in Fig. 5.1. Afterwards a binned likelihood fit to the m_T distribution of the selected $W \to \ell\nu$ events is performed for the electron and muon separately. In the fit, the contribution from the SM top production is fixed to the MC prediction and the shape of the $W \to \ell\nu$ signal samples are fixed to the ones from the simulated MC events. The normalizations of the $W \to \ell\nu$ signal contribution and multijet contribution are allowed to float. The fitted results are shown in Fig. 5.2.

The m_T distributions of reconstructed $W \to \ell\nu$ candidates are shown in Fig. 5.2. In the $W \to e\nu$ channel, approximately 17% events are from the multijets contamination, while in the $W \to \mu\nu$ channel, the fraction is only $\approx 2.2\%$.

The rate of CR jets are measured in these control events and used to estimate the number of signal events in the Z+Jets region. This background estimation procedure is outlined in full detail in Section 6.

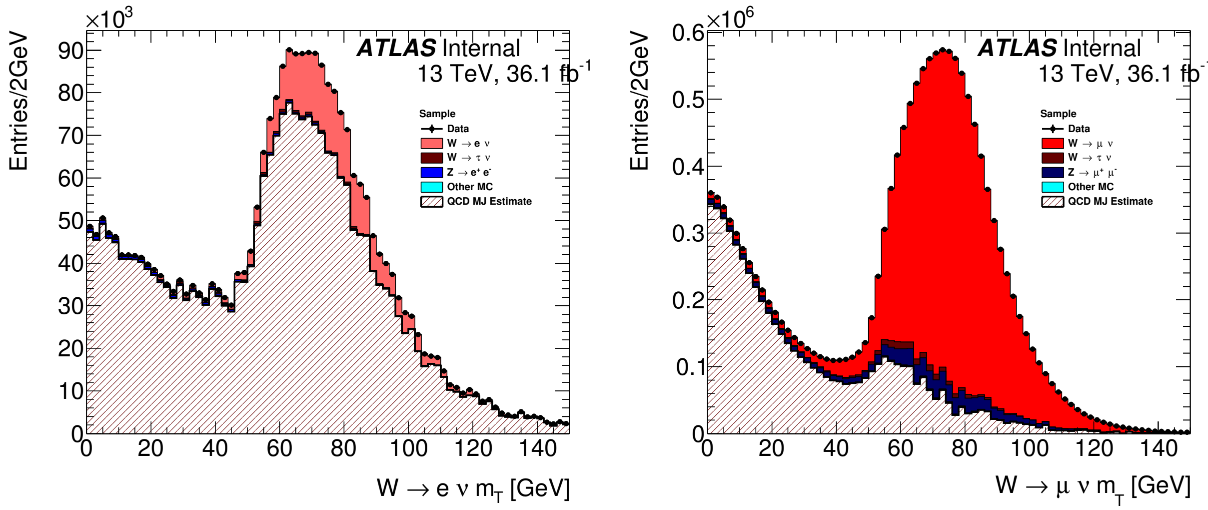

Figure 5.1: The W transverse mass distributions with exclusively loose lepton identification from the control data in the electron (left) and muon (right) final state. The QCD Multijets templates are determined by subtracting the MC simulated contributions of SM processes with prompt leptons from the data.

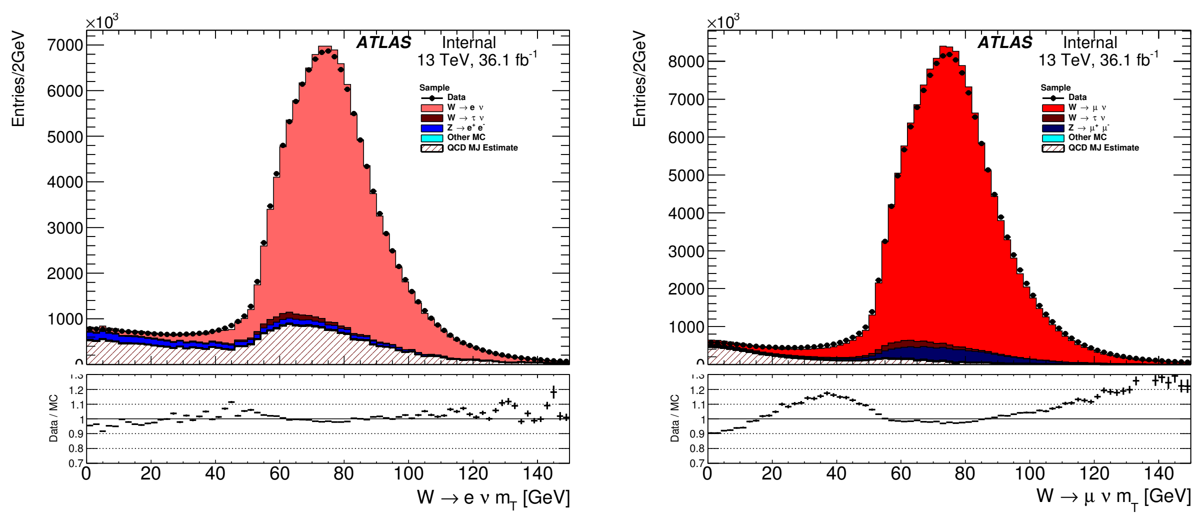

Figure 5.2: Fitting the QCD Multijets template and MC to the data in the QCD-supressed region. Only the region $m_T > 50\text{GeV}$ is considered a $W \to \ell\nu$ event. The electron channel (left) contains $\approx$ 17% QCD multijets background above the 50GeV threshold while the muon channel (right) contains $\approx 2.2\%$.

5.5 Signal Events

Signal events require a reconstructed SM Z boson in addition to a CR Jet (see Section 4.3).

Z bosons are reconstructed from the combination of two oppositely charged lepton candidates with the same flavor ($Z \to \ell^+\ell^-$). Events with additional leptons are rejected. The event preselection requires that at least one of the selected leptons is required to match to a lepton trigger object. It is required that the invariant mass of the reconstructed Z candidate ($m_{\ell\ell}$) lies within the mass window $66\,\mathrm{GeV} < |m_{\ell\ell}| < 116\,\mathrm{GeV}$, as shown in Fig. 5.3.

The signal yield is estimated by comparison of the number of observed $pp \to ZZ_d$ event candidates in data to the predicted number of background events, as described in Sec. 6. For larger mediator masses a higher jet E_T cut results in a better signal-to-background ratio. For such samples the jet E_T cut which provides the better sensitivity is selected instead. These E_T cuts are specified in Section 9.

5.5.1 Z Reconstruction Efficiency

To extract results from the analysis it is necessary to determine not only the number of Z bosons selected, but also the fraction of Z bosons which have been removed by the selection criteria. This is done by applying the same selection cuts to a MC sample of Z bosons and observe the fraction of them which are removed. As each signal MC has a different Z p_T spectrum, each will also have a slightly different Z reconstruction efficiency. The Z boson reconstruction efficiencies are summarized in Table 5.3 for each signal MC sample.

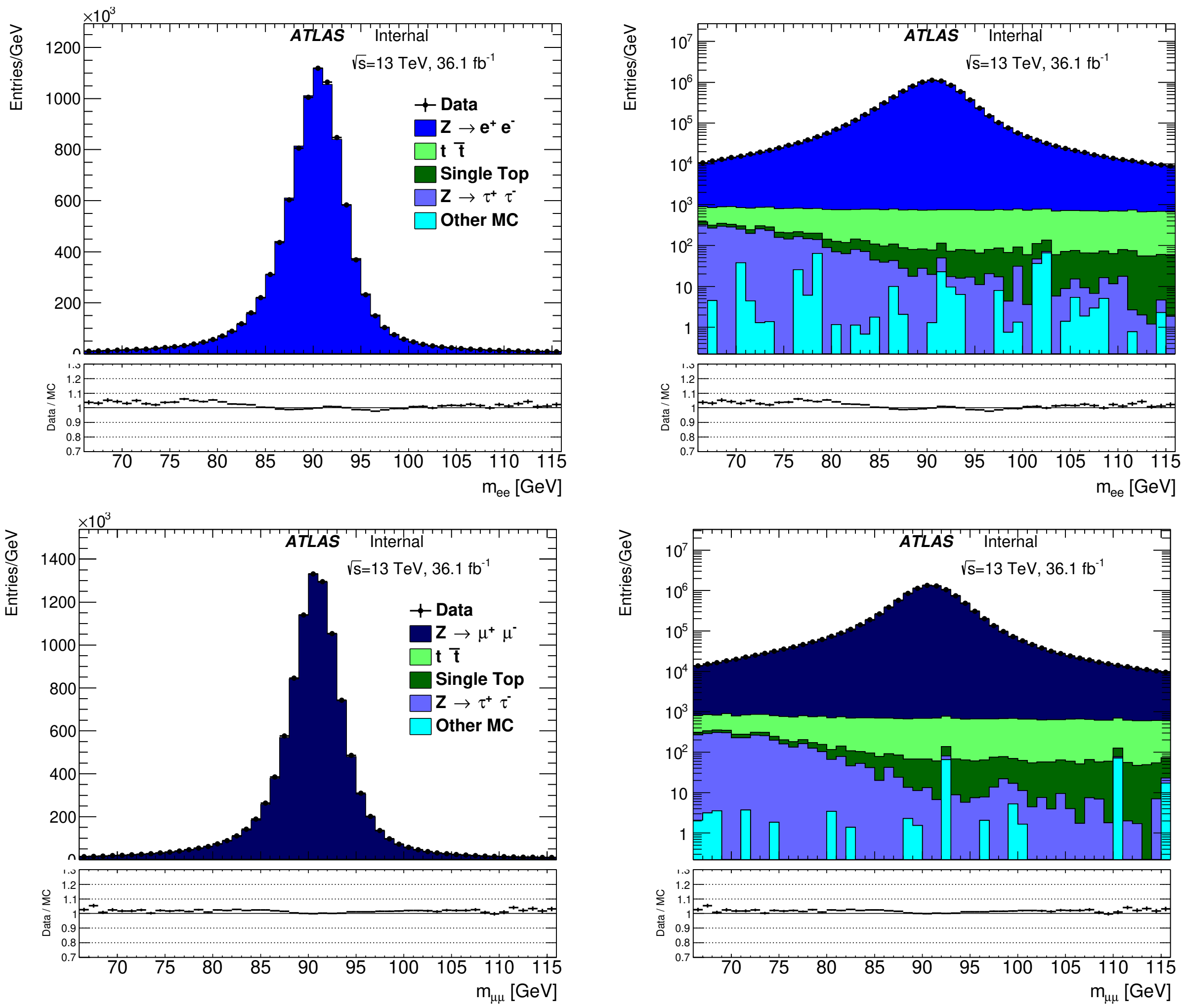

Figure 5.3: The invariant mass distributions of the reconstructed $Z \to e^+e^-$ (top) and $Z \to \mu^+\mu^-$ (bottom) candidates in a linear scale (left) and log scale (right). Here it is also required that there is at least one baseline jet in each event.

Table 5.3: The Z reconstruction efficiency for each signal MC sample. More boosted samples result in the Z having p_T peaked at higher values which changes the efficiency slightly.

m_Φ [GeV]	m_{Z_d}[GeV]	$\epsilon^Z_{reconstruction}$
125	5	45%
125	10	45%
125	15	45%
250	10	42%
250	50	42%
250	100	40%
500	20	50%
500	100	50%
500	200	47%

CHAPTER 6. BACKGROUNDS

The backgrounds of Z + jets are well understood ($Z \to \tau\tau$ and $t\bar{t}$ being the largest), however the background rate of CR jets is not.

6.1 Sources of CR Jets

Possible sources of CR jets have been thoroughly studied in Ref. [13]. They are:

- **Detector effects :** A CR jet can be produced if adjacent calorimeter cells have an upward fluctuation at the same time so that they can be registered as a seed for the anti-k_t jet reconstruction algorithm. This effect decreases with increasing jet E_{T} requirement [13] and is the primary motivation behind the jet energy fraction cuts made by the JetCleaningTool [16] for typical ATLAS analyses without possible presence of long lived neutral particles. The CR jet probability in W+Jets events is shown as a function of η and E_{T} in Figure 6.1. From this diagram it is clear that the transition region between the barrel and end-cap cryostats ($1.0 < |\eta| < 1.3$) has an increased rate at lower energies. This effect been observed in previous studies which use low EMF jets [30] and is believed to be due to the fact that jets in this region are affected by even small energy in the Tile Gap scintillators (shown in Fig 6.2), and are therefore significantly affected by noise contributions. This effect is present only at low energies so jets in this region below $E_{\mathrm{T}} < 60$GeV are excluded as CR jets.

- **Cosmic Muons :** It is possible for cosmic muons to enter the detector and deposit energy in the HCal without leaving tracks in the center of the detector. An actual ATLAS Event display containing a cosmic muon depositing energy in the HCal is shown in Fig 3.11. The cosmic muon spectrum decreases [5] exponentially with p_{T}, which suggests that this source of CR jets should also decrease as a function of jet E_{T}. Despite the ATLAS detector lying ≈ 100m below ground the volume above isn't solid rock. Much of the region was excavated

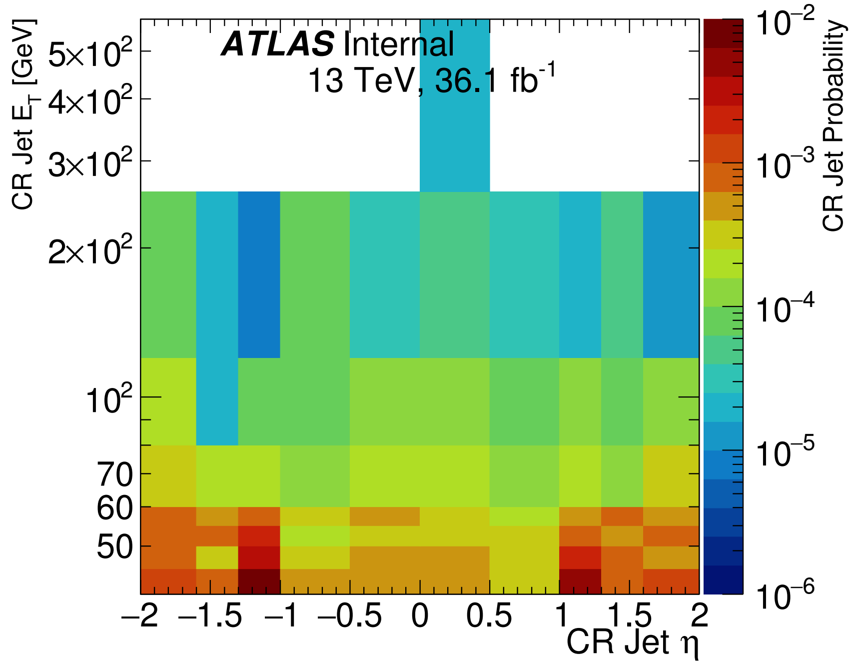

Figure 6.1: The measured CR jet fake probability measured as a function of E_{T} and η for $W + jets$ events. The probability is greatly increased in the transition region between the barrel and end-cap cryostats ($1.0 < |\eta| < 1.3$) - motivating the removal of jets in this region.

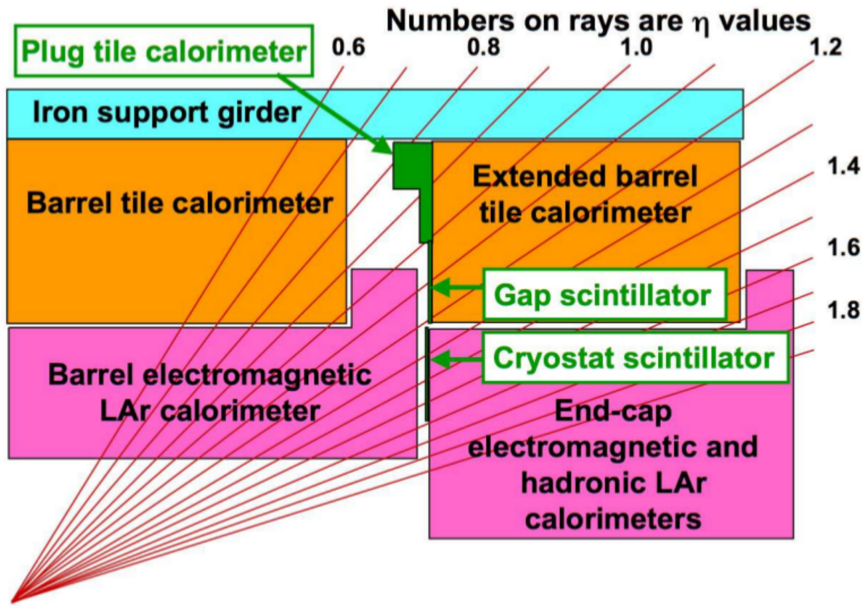

Figure 6.2: A diagram illustrating the gaps between the various hadronic and electromagnetic components of the ATLAS calorimeter. Noise in the gap scintillator can result in a greatly increased background rate of CR jets in its η region.

to lower the detector components into place. Cosmic muons possess sufficient energy to fire the ATLAS muon triggers at a rate of a few Hz [8].

- **Beam Induced Background (BIB) :** While the protons in each beam are confined by the magnetic fields, there are still some traveling protons in the beam that are far away from the center of the beam. Those protons may interact with beam pipe apertures or surrounding gas to produce particle showers in very forward directions, called "Beam Induced Background" (BIB) [44]. Such a shower could deposit energetic particles into the calorimeter without passing through the tracking system or ECal, causing a CR jet to be reconstructed. These collisions occur very far down the beamline (starting around z = 150m) and thus most particles are absorbed by the nearby shielding. However muons from these interactions are very energetic and can travel parallel to the beamline ultimately depositing energy in the HCal. Quality control is capable of detecting some muons on these trajectories, but not all. An ATLAS event display of such an event, taken with no collisions, is shown in Fig 3.12.

Other studies of CalRatio jets [13], [55] show this is one of the major background sources to fire the customized CalRatio trigger designed for long lived neutral particles, however this analysis utilizes lepton triggers (as detailed in Section 5) and is thus not biased towards selecting this background.

- **Truly Neutral Jets :** There are some neutral hadrons and mesons in the Standard Model with long lifetimes, such as the neutron, Λ, and K^0. If such particles are produced with a large enough E_{T}, then relativistic time dilation allows the neutral particles to travel farther before decaying, which may result in reconstruction of a CR jet. The lifetimes of these particles (and others) are shown in Table 2.2 and are so short that such particles decaying within the volume of the HCal is small. Additionally these particles are largely formed during the hadronization of a jet and so should be expected to be collinear with other particles, some of which would carry charge. The presence of neutral particles within a jet are affected by the flavors of the partons which initiate them, and therefore it is crucial to compare the parton content of a control sample to the signal. This comparison is done in detail in Section 6.3.

- **Pileup Jets :** Pileup jets have a different probability of producing CR jets. Pileup jets are produced from a different vertex and will therefore have a mismeasured track multiplicity, making it easier to pass the $nTrks$ cut. However pileup jets are also very QCD-like and therefore have a very different parton composition than W and Z associated jets (see Sec 6.3 for details). Pileup jets overlapping signal jets add energy in the ECal, therefore shifting the *logRatio* variable down and *decreasing* the CR jet probability. These competing effects are discussed in greater detail in Sec 6.2.

6.2 Pileup

It is observed in W+Jets events that different jet multiplicities have different CR jet probabilities (see Fig 6.3).

This is due to the fact that pileup jets make up a different proportion of events at each jet multiplicity, and have a different CR jet probability. Pileup jets originate from vertices other than the PV and are thus greatly removed by the jet vertex tagger (JVT) tool. While this tool also removes nearly all signal jets (and is therefore not useful for separating signal from background), it can be used to determine the relative fraction of jets in each sample originating from pileup. The jet multiplicity distribution of all baseline jets in the W+Jets sample is compared to the distribution of all baseline jets which pass the JVT cut in Fig 6.4. From this figure we can see that as jet multiplicity increases the relative fraction of pileup jets also increases.

The dependence on pileup is further confirmed by the observation of the CR jet probability parameterized by μ, shown in Fig 6.5. This observation makes clear that the net effect on the CR jet rate from pileup is a *decrease*.

Pileup jets overlapping jets from the signal event also leave additional energy in the ECal, suppressing the number of jets capable of passing the *logRatio* cut. This effect can be observed in Fig 6.6. The peak of the *logRatio* distribution is shifted slightly for events at different μ.

The rate of CR jets in MC is not a good model for data, however the effect of pileup jets is simulated (as discussed in Sec 3.2.8). As such this same effect on the CR jet probability for different amounts of pileup is also observed in MC (see Fig 6.7).

This dependence led to a question of whether or not to parameterize the CR jet probability by jet multiplicity to obtain a more accurate result. This parameterization was performed and was found to result in additional uncertainty on the estimate, shown in Fig 6.8. The two results are consistent with one-another within the uncertainty so this parameterization was not used by the final analysis.

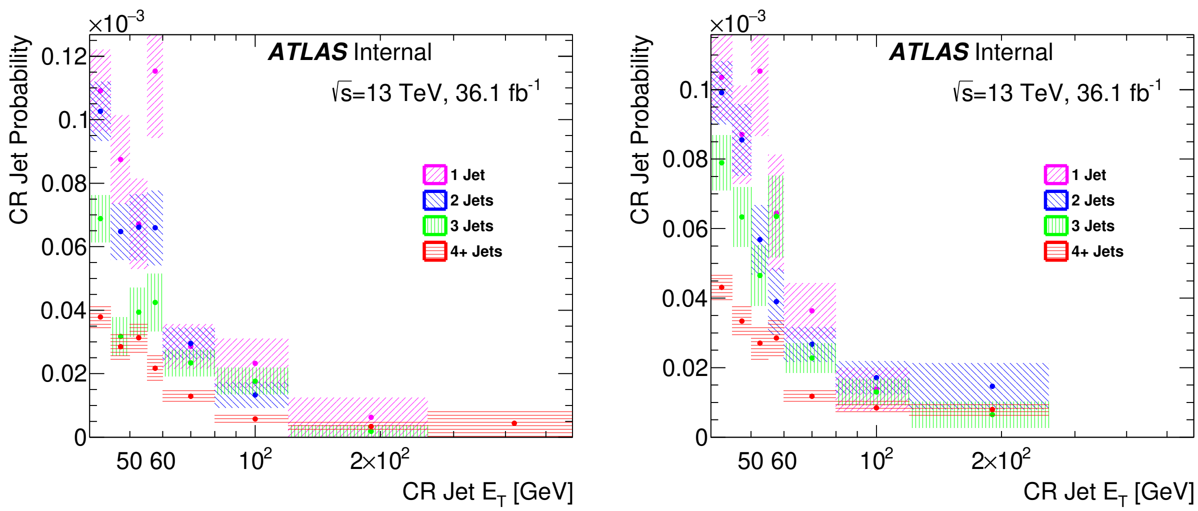

Figure 6.3: The measured CR jet fake probability as a function of E_{T} for $W \to e\nu$+jets (left) and $W \to \mu\nu$+jets (right) events with different jet multiplicity slices. At larger jet multiplicities the CR jet rate decreases (as the proportion of pileup jets increases). The colored bands are statistical uncertainty only.

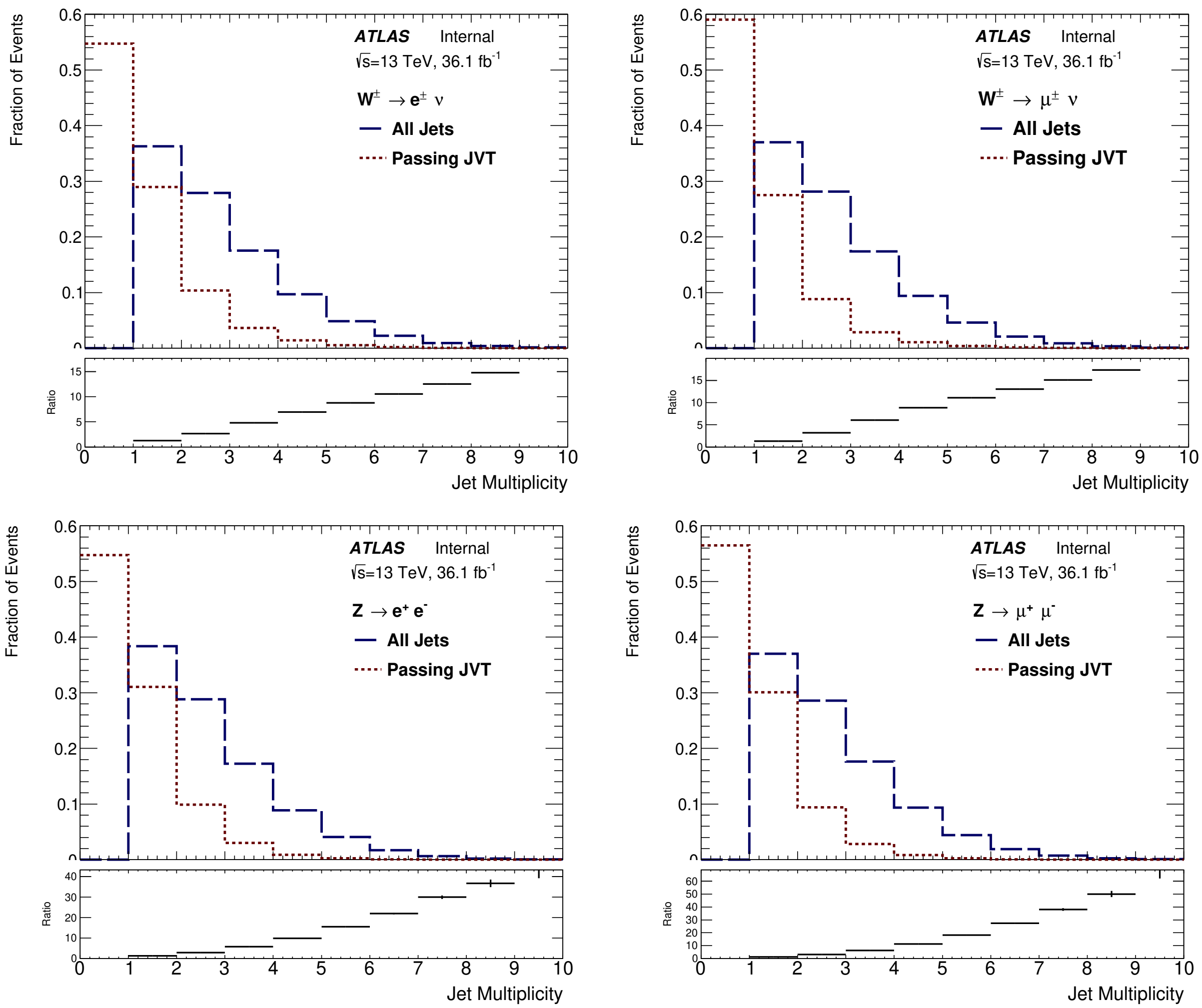

Figure 6.4: Jet multiplicity for all jets and jets which pass the JVT cut in each sample (from left to right, top to bottom, $W \to e\nu$, $W \to \mu\nu$, $Z \to ee$, and $Z \to \mu\mu$). The JVT cut removes a large fraction of pileup jets, enabling an estimate of the fraction of pileup jets in each jet multiplicity bin.

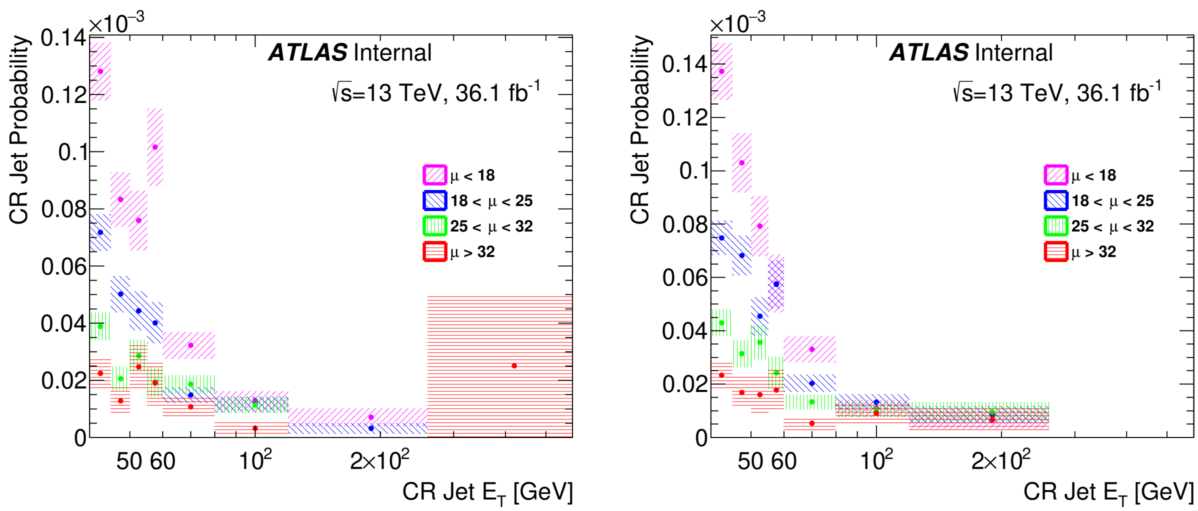

Figure 6.5: The measured CR jet fake probability as a function of E_{T} for $W \rightarrow e\nu$+jets (left) and $W \rightarrow \mu\nu$+jets (right) events with different pileup μ slices. At larger pileup μ the CR jet rate decreases (as jet multiplicity increases). The $\mu < 18$ bin has an average jet multiplicity of 2.0, $18 < \mu < 25$ events have an average jet multiplicity of 2.4, $25 < \mu < 32$ has 2.8, and $\mu > 32$ has 3.2. The colored bands are statistical uncertainty only.

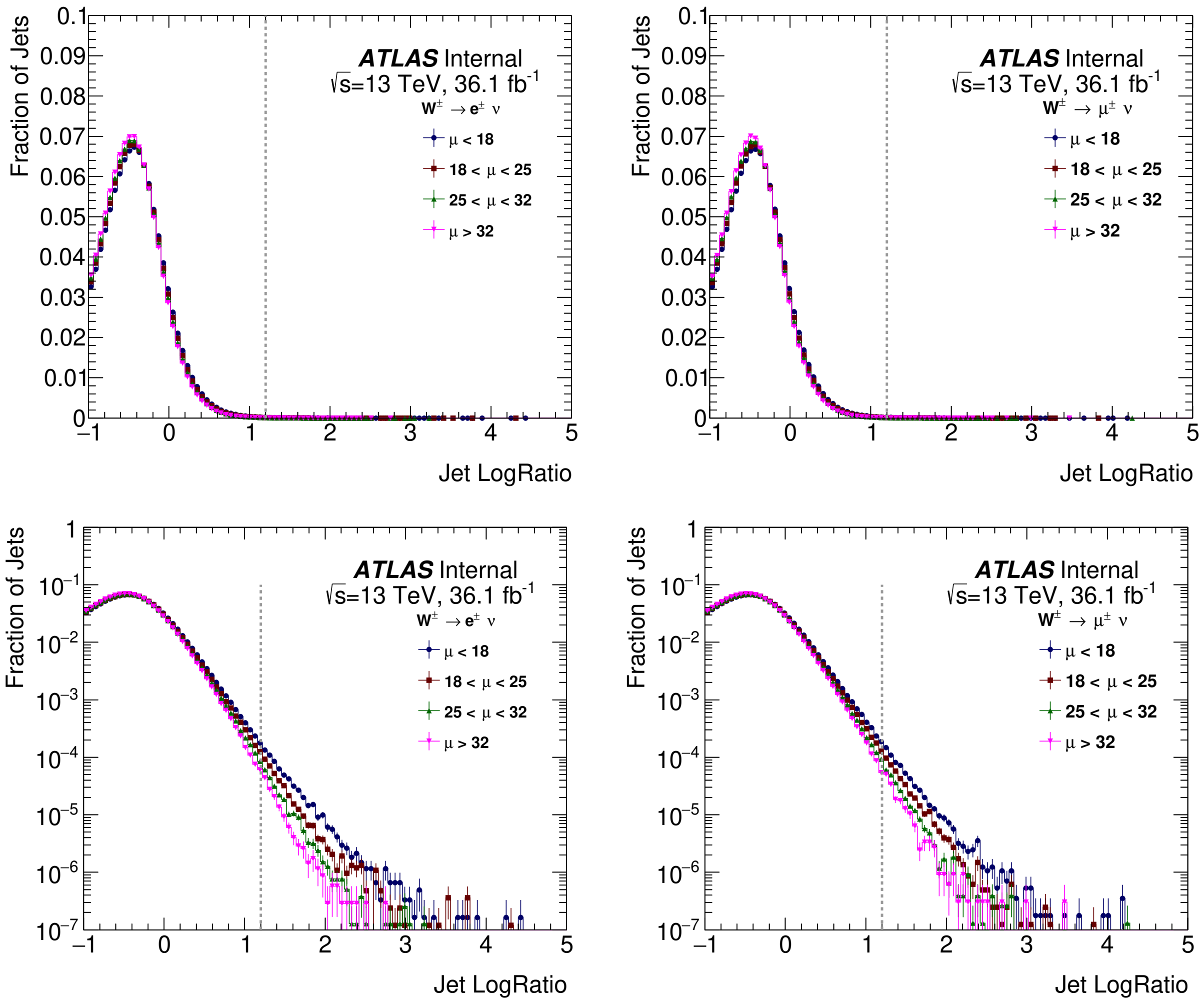

Figure 6.6: The logRatio of all jets in the $W \to e\nu$ (left) and $W \to \mu\nu$ (right) channels, normalized to the same number of entries. Note the very slight shift in the distributions - at higher pileup μ the logRatio distribution decreases. The log scale better shows the effect in the tail of the distribution, while the linear scaled plots better show that the peak of the distribution is shifted. The dashed gray vertical line indicates the position of the cut made on this variable.

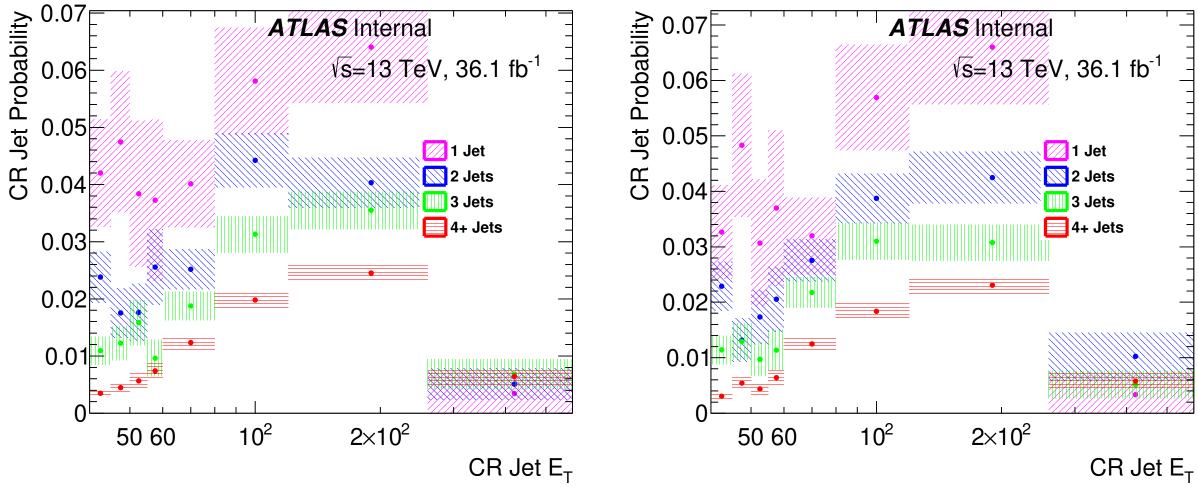

Figure 6.7: The CR jet probability in signal MC events in which an LLP decay happens well within the tracker for the electron channel (left) and the muon channel (right). Even in MC the effect of increased pileup in events is observed to shift the probability.

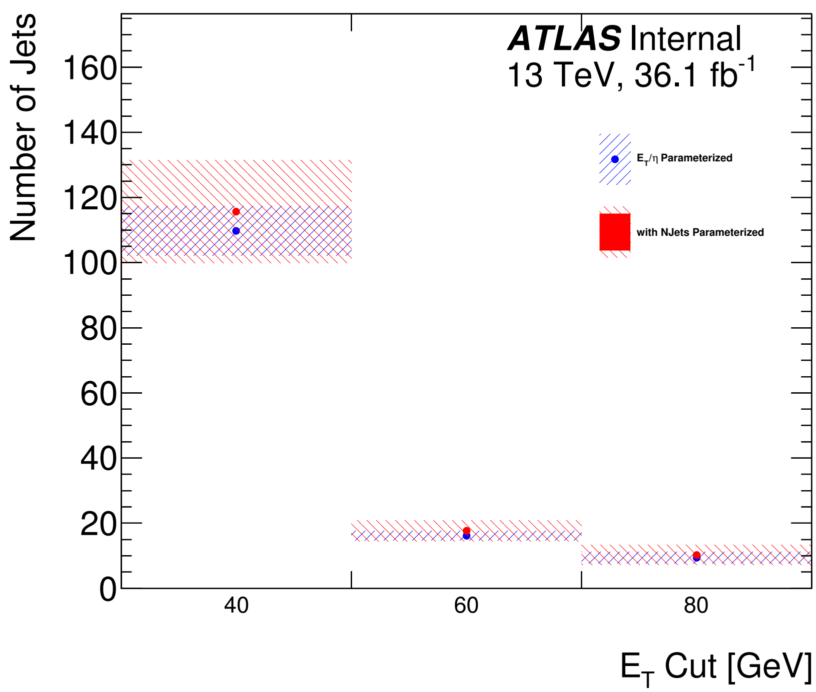

Figure 6.8: Here the estimated number of CR jets in the $Z + jets$ region in the electron and muon channel combined, based on measurements in the $W + jets$ region is shown, both with and without parameterization by jet multiplicity.

6.3 Parton Flavor Dependence

The Run I CalRatio paper [13] found a correlation which implied that different partons (i.e. gluon or quark) have different probabilities of producing CalRatio jets (based on their charge and subsequent probability of producing tracks). A comparison of the quark/gluon content in W and Z associated jets is important in order to understand how similar the CalRatio jet probability in the W sample is to the probability in the signal region. This was observed in MC generated events using the relative cross-section of the $2 \rightarrow 2$ hard process X+g and X+q processes. There is an $\approx 1\%$ statistical error as only 5000 events were generated. The results (summarized in Table 6.1) show that the W and Z samples should have comparable production of gluon and quark jets.

Table 6.1: The fraction of Pythia8 generated events which produced gluons and quarks in addition to the W or Z boson.

	X+q	X+g
W + jets	0.726	0.274
Z + jets	0.729	0.271

This comparison produced from MC generated events doesn't include the possible contribution from QCD multijets - which is a source of discrepancy between the W and Z regions in data. QCD jets are largely from gluons[18] in the region below 500GeV. There are known differences between gluon and quark initiated jets which have been used to determine a level of discriminating power between the two [21]. Gluon initiated jets tend to have a larger track multiplicity, with 60% of gluon jets with 100GeV $< p_{\mathrm{T}} <$ 200GeV have $n_{trks} > 10$ while only 20% of quark initiated jets pass the same selection, shown by Fig 6.9. The track multiplicity distributions of all jets with $E_{\mathrm{T}} >$ 40GeV are shown in Figure 6.10

The dependence of the CR jet probability on the parton which initiates the jet can be further checked through comparison of the $W \rightarrow e\nu$ and $W \rightarrow \mu\nu$ channels (which have significantly differing quantities of QCD background, measured in section 5.4.1). As shown in Fig 6.11 the CR jet probabilities in the electron and muon channels are relatively consistent, despite the differing parton content. For this analysis the central value of the CR jet probability is determined from the

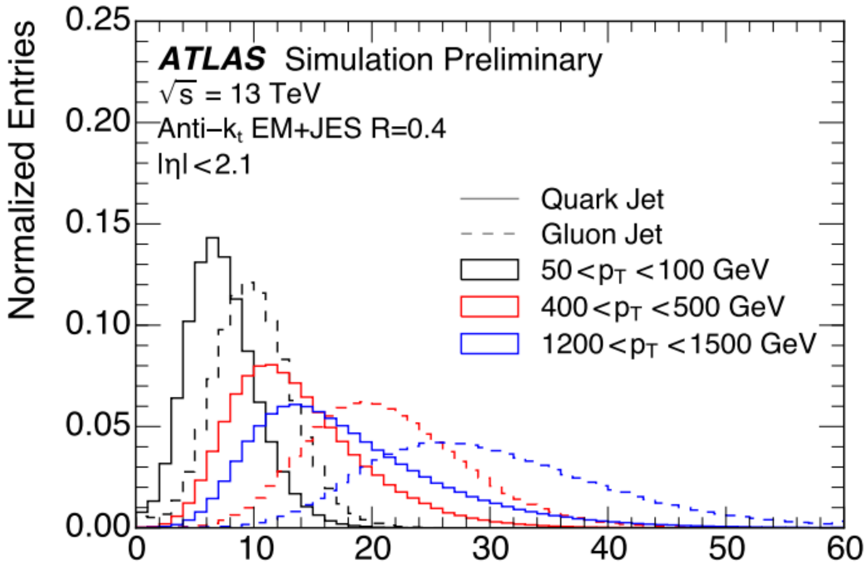

Figure 6.9: Distribution of the jet reconstructed track multiplicity (n_{trk}) in different p_{T} ranges with the Pythia 8 generator using the A14 tune, the NNPDF2.3 PDF set, and processes with a full simulation of the ATLAS detector. Jets must be fully within the tracking acceptance ($|\eta| < 2.1$) and tracks are required to have $p_T > 500$MeV and pass additional quality criteria [21].

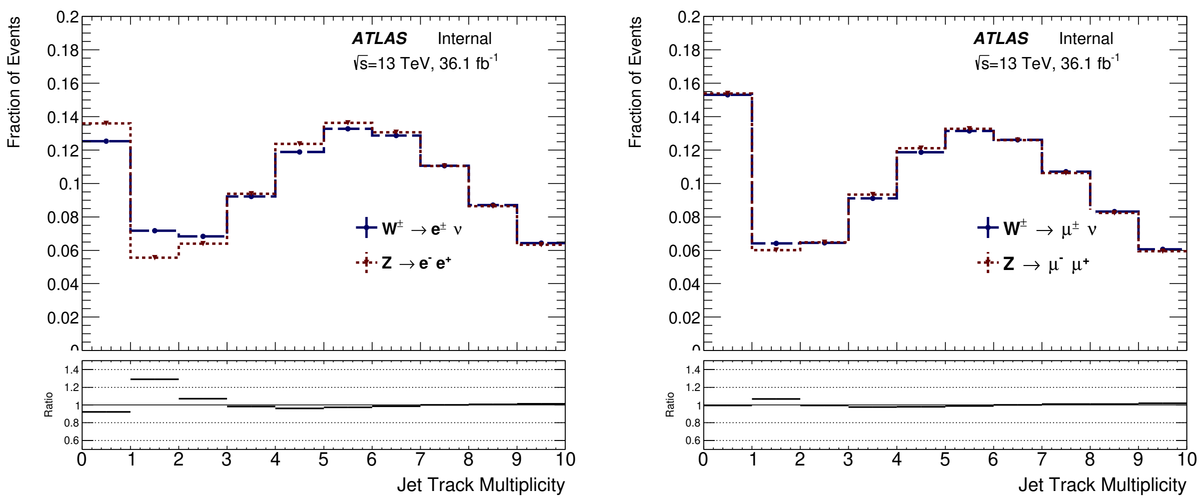

Figure 6.10: The track multiplicity of jets with $E_{\mathrm{T}} > 40$GeV in Z events compared to W events for the electron (left) and muon (right) channels. The similar shape of the distributions indicate a similar composition of jet-initiating partons.

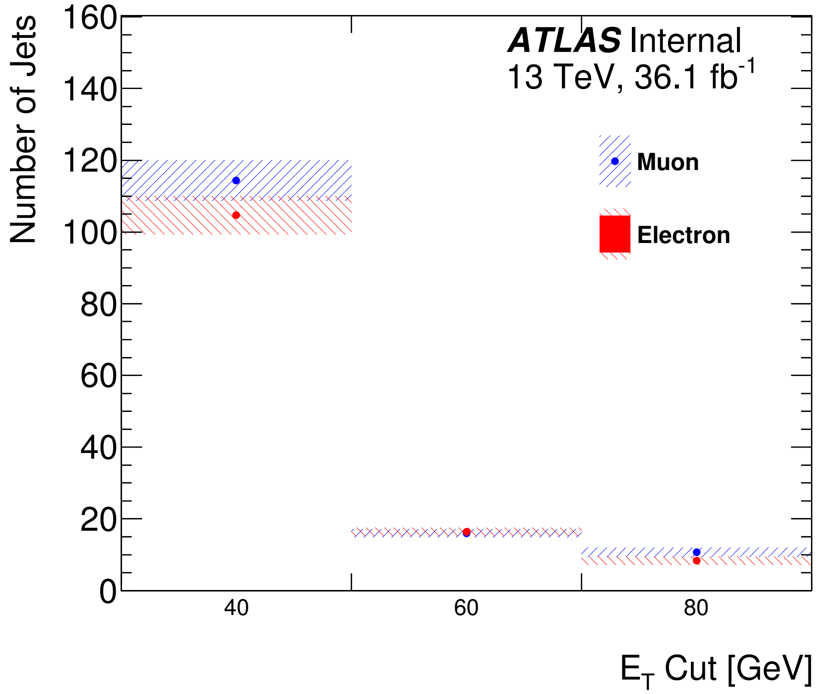

Figure 6.11: The CR jet estimate as a function of CR jet E_{T} in the $Z + Jets$ region is shown here as made using the $W \to e\nu$ channel (red) and $W \to \mu\nu$ channel (blue). The muon channel has significantly less QCD multijets background and is thus taken to be more similar to the $Z + Jets$ region than the electron channel. The difference between the channels is taken as an additional systematic uncertainty on the estimate.

$W \to \mu\nu$ channel while the difference between it and the $W \to e\nu$ channel is taken as an additional systematic uncertainty on the estimate.

These data seem to suggest that the dependence of the CR jet fake probability on the initiating parton of the jets can introduce a small effect when comparing the W+jets and Z+jets samples, and we can take the effect as an additional systematic.

6.4 CR Jets in the Control Sample

An accurate simulation of the background sources of the CR jets is very difficult. However the probability for a jet to be identified as a CR jet can be measured using W+jets data, referred as the CR jet fake probability hereafter. The reconstruction of the W+jets sample is described in

Sec. 5.4. The fake probability (f_{CR}) is defined as

$$f_{CR} = \frac{N_{CRjet}}{N_{jet}}, \tag{6.1}$$

where N_{jet} is the total number of the selected jets in the W+jets sample and N_{CRjet} is the total number of selected jets that can be identified as the CR jets in the same sample. The fake probability is measured as a function of jet E_T and η, shown in Fig 6.1.

The total number of CR jets in the W+Jets control region for each E_T cut is listed in Table 6.2. The corresponding estimates for the number of CR jets in the $Z + Jets$ signal region and their uncertainty are summarized in Table 6.3.

Table 6.2: The total number of CR jets in the $W \to \ell\nu$ control region at 3 different E_T cuts.

	$E_T > 40$GeV	$E_T > 60$GeV	$E_T > 80$GeV
Number of CR Jets ($W \to e\nu$)	982	189	63
Number of CR Jets ($W \to \mu\nu$)	1030	186	71
Number of CR Jets (Total)	2012	375	134
All Jets ($W \to e\nu$)	3.25×10^7	1.46×10^7	0.82×10^7
All Jets ($W \to \mu\nu$)	3.06×10^7	1.32×10^7	0.73×10^7
All Jets (Total)	6.30×10^7	2.78×10^7	1.55×10^7
Average Probability	3.19×10^{-5}	1.35×10^{-6}	8.65×10^{-6}

6.5 Expected Background in Signal Sample

The expected number of background events in the $pp \to ZZ_d$ search is determined by reweighing the observed inclusive Z+jets events using the measured CR jet fake probability from the control region. For each event with N associated jets (j_1,j_2 ... j_N), the probability for such an event to be identified as a $pp \to ZZ_d$ candidate is

$$P(j_{i\in N}) = 1 - \prod_{i\in N} \left[1 - f_{CR}(E_T^i, \eta^i)\right] \tag{6.2}$$

where $f_{CR}(E_T^i, \eta^i)$ is the CR jet probability for the jet j_i as measured in the W+jets sample (as a function of E_T and η). The sum of the probability P for all the selected Z+jets events is the expected background number of the $pp \to ZZ_d$ candidates. Given that $f_{CR} << 1$ at all E_T and η, the probability of obtaining an event with more than one CR jet is extremely small. There were no events in the $W + Jets$ data with more than 1 CR jet.

The sum of the probability P for all the selected Z+jets events is the expected number of background events in the signal sample. The results are summarized in Table 6.3.

Table 6.3: The number of expected background events in $Z \to \ell^+\ell^-$ +jets based on the rate of CR jets in the $W \to \ell\nu$ control region, including the corresponding systematic uncertainty. The number is shown for each E_T cut used.

E_T Cut [GeV]	N_{expected}
40	174.5 ± 22.0
60	33.0 ± 5.0
80	13.2 ± 2.8

6.6 Contamination of Control Region

A soft or poorly reconstructed lepton from a $Z \to \ell^+\ell^-$ decay (or one which traverses an area of the detector which doesn't result in proper reconstruction) will result in a signal event entering the control region. This in turn implies that any background estimate determined in the control region necessarily includes some fraction of signal events which will decrease our ability to distinguish signal from background. It is thus necessary to determine how much such contamination will affect our results.

To estimate the number of signal events which would enter the control region we can utilize $Z \to \ell\ell$ background MC. It was observed that for every 5 $Z \to \ell\ell$ events in the signal region (passing the Z reconstruction criteria) 1 event is expected in the control region. However the cross section of the W boson decays to leptons is considerably larger than that of the Z. As shown in Fig 5.2, only $\approx 2\%$ of the control region is expected to be $Z \to \ell\ell$ background. Given this and the large number of CR jets in the control region (see Table 6.2) the effect from any signal event in the control region will be small.

If X events are found in the signal region in excess of the background estimate, then $\approx X/5$ events should be expected in the control region. This number needs to then be subtracted from the total number of CR jets in the control region. The W+jets control sample has relatively large statistics (as indicated in Table 6.2) so this effect is guaranteed to be small.

For example, if 270 CR jets are found in the signal region with $E_{\mathrm{T}} > 40\mathrm{GeV}$ (an excess of ≈ 100 events over the expected background from Table 6.3), then it can be assumed that ≈ 20 CR jets in the control region originate from this signal. With 2010 CR jets total in the control region this would change the CR jet probability (and therefore the background estimate) by a factor of only $\approx 1\%$.

6.7 Validation in Z Sideband Region

It is useful to validate this background estimation procedure in another region. Using the CR jet fake probability measurement from the control sample the number of expected CR jets in a Z "sideband" region can be determined. The sideband region is defined by events with a dilepton invariant mass of $30GeV < m_{ll} < 55GeV$, well outside the mass window of the SM Z boson. The available sideband regions are shown in Fig 6.12. The region selected was chosen to minimize the amount of true $Z \rightarrow \ell\ell$ background (which could contain signal events). The results are roughly consistent (shown in Table 6.4 and Fig 6.13) but due to a lack of statistics this validation is not conclusive.

6.7.0.1 Trackful CR Jet Validation Region

An additional validation region was selected in which one CR jet cut was reversed but kept as close as possible to the signal region. These jets are called "Trackful" CR jets and are defined using the jet definition from Section 4.3 in addition to :

- $Jet E_{\mathrm{T}} > 40\mathrm{GeV}$
- $\log_{10}(\frac{1-EMF}{EMF}) > 1.2$

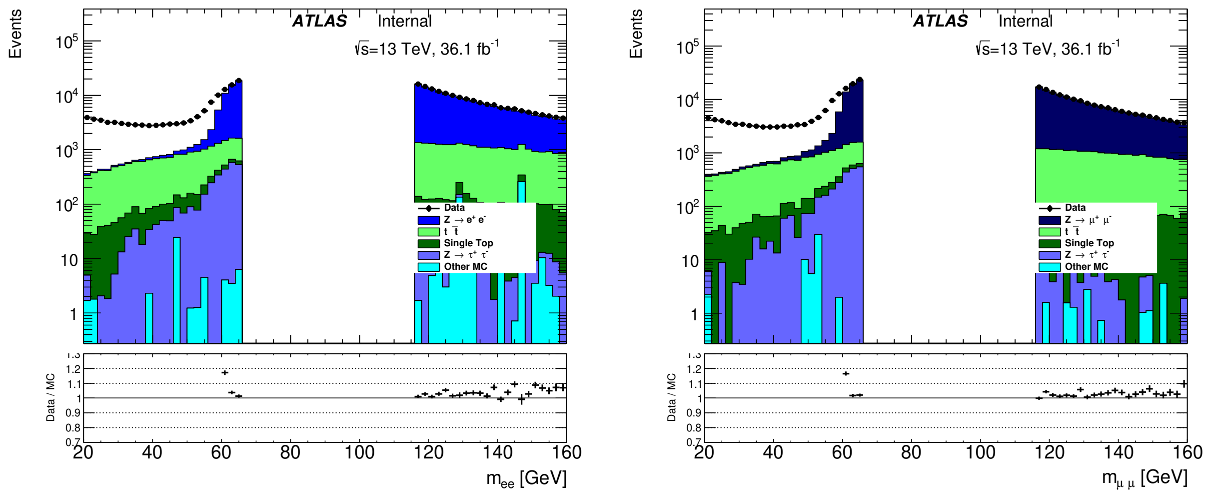

Figure 6.12: The Z Sideband region ($66GeV > m_{ll} > 116GeV$). To reduce contamination from $Z \rightarrow \ell^+\ell^-$ events only the region $30GeV < m_{ll} < 55GeV$ was used for validation.

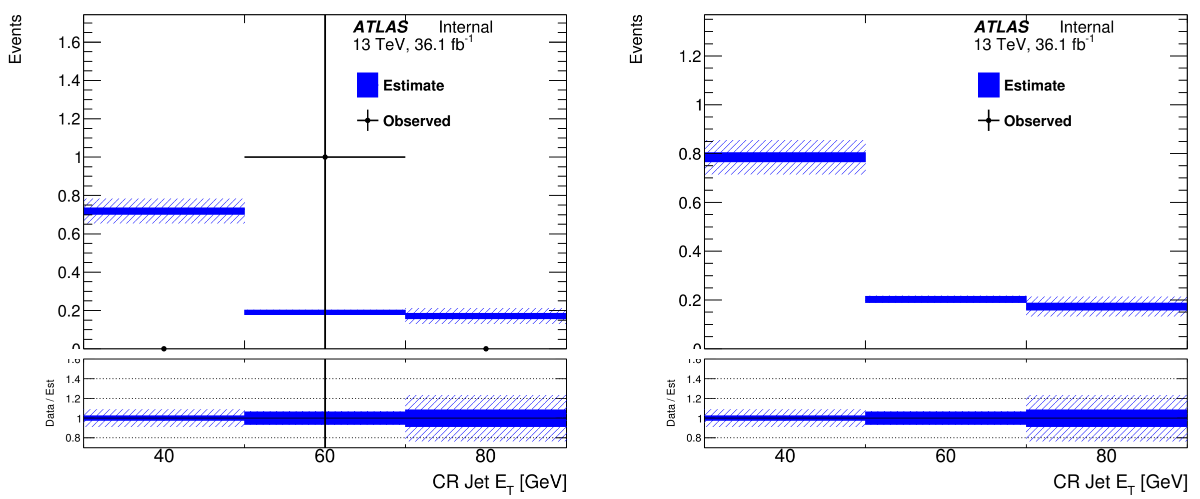

Figure 6.13: The total number of events with at least one CR jet in the sideband validation region at 3 different E_{T} cuts (binned exclusively) for the $Z \rightarrow ee$ (left) and $Z \rightarrow \mu\mu$ (right) channels. The expected number of events at each cut is predicted by the rate measured in the W+jets control region. The uncertainty on the estimate originating from the statistics in the control region is shown as a solid band while the additional systematic uncertainties are shown as the shaded band.

Table 6.4: The total number of events containing at least one CR jet in the sideband validation regions at 3 different E_{T} cuts (binned inclusively). The expected number of jets at each cut is predicted by the rate measured in the W+jets control region and is shown with the corresponding systematic uncertainty. The Poisson probability of making the measurement (given the uncertainty on the mean value) is shown.

	$E_T > 40GeV$	$E_T > 60GeV$	$E_T > 80GeV$
Jets in sideband ($Z \rightarrow e^+e^-$)	4.38×10^4	2.82×10^4	1.81×10^4
Jets in sideband ($Z \rightarrow \mu^+\mu^-$)	4.55×10^4	2.87×10^4	1.82×10^4
Total Jets in sideband	8.93×10^4	5.69×10^4	3.63×10^4
Expected CR Jet events in sideband ($Z \rightarrow e^+e^-$)	1.08 ± 0.12	0.36 ± 0.05	0.17 ± 0.04
Expected CR Jet events in sideband ($Z \rightarrow \mu^+\mu^-$)	1.16 ± 0.12	0.38 ± 0.05	0.17 ± 0.04
Total Expected CR Jet events in sideband	2.24 ± 0.24	0.74 ± 0.10	0.34 ± 0.08
Observed CR Jet events in sideband ($Z \rightarrow e^+e^-$)	1	1	0
Observed CR Jet events in sideband ($Z \rightarrow \mu^+\mu^-$)	0	0	0
Total Observed CR Jet events in sideband	1	1	0
$P_{poisson}$	$16.8\% - 27.07\%$	$27.6\% - 33.8\%$	$65.7\% - 77.1\%$

- There is at least 3 tracks with $p_{\mathrm{T}} > 1$GeV associated with the jet.
- -3ns $<$ Jet Timing < 15ns

The track multiplicity cut was selected to avoid signal contamination (see Fig 4.7).

Using this definition the rate of trackful CR jets is measured in the $W + jets$ data (Fig 6.15) and used to determine an estimate for the number of trackful CR jets in the $Z + jets$ data, and then compared to the measured number of trackful CR jets in $Z + jets$ data. Only baseline jets with $nTrks > 2$ are included in the denominator of this calculation. In the W+Jets control sample not a single event contained more than 1 trackful CR jet. Results of this validation are shown in Fig 6.16.

The estimate from the $W + Jets$ region appears to underestimate the corresponding number of jets in the $Z + Jets$ region. To correct the region a normalizing scale factor was determined (1.24 ± 0.11) and used to shift the estimate. The uncertainty on this scale factor was used as an additional systematic uncertainty. The results are shown in Fig 6.16 and Table 6.5.

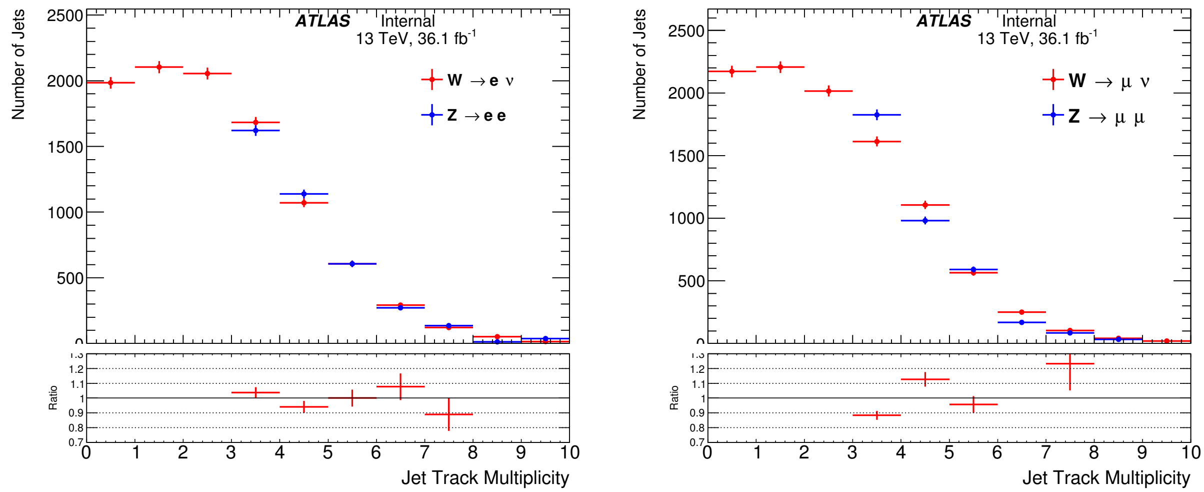

Figure 6.14: The track multiplicity of jets in the W+Jets data compared to those in the Z+Jets data (normalized to one another) passing all selection criteria other than the cut on track multiplicity. Bins below $nTrks > 2$ in the Z+Jets data are excluded as they may contain non-negligible contamination from signal.

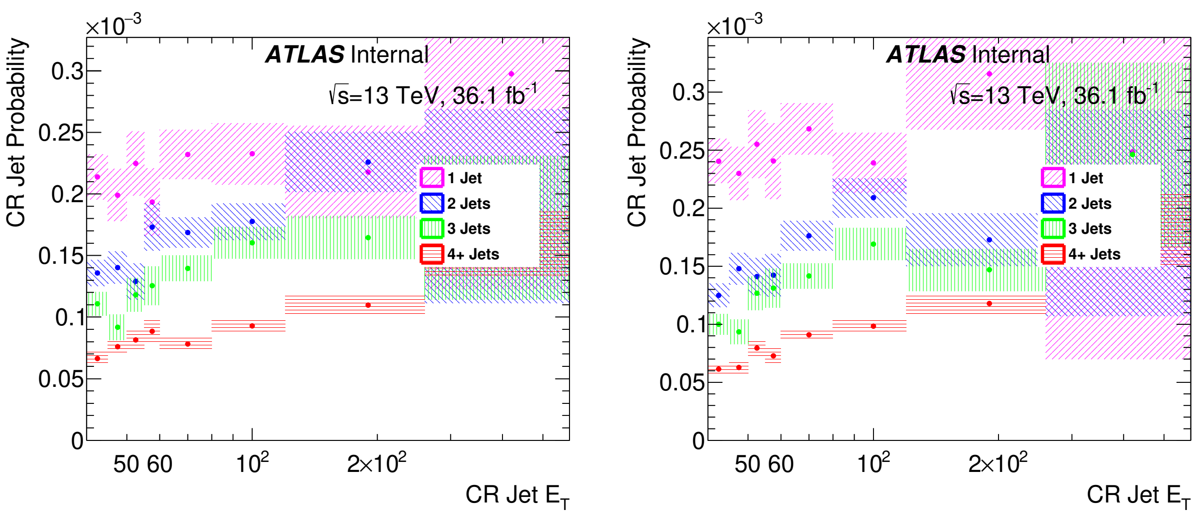

Figure 6.15: The trackful CR jet rate as a function of the jet E_{T} cut for different jet multiplicities in the electron channel (left) and the muon channel (right). Note the different behavior as a function of E_{T} compared to the CR jet rate compared to Fig 6.3.

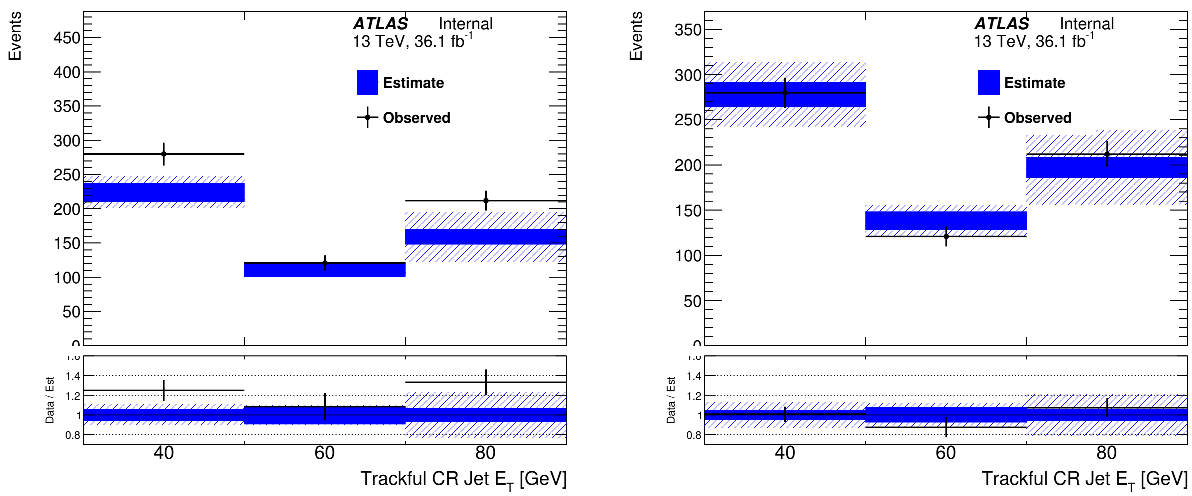

Figure 6.16: The total number of events containing at least one trackful CR jet in the validation region at 3 different values of jet E_{T} before (left) and after (right) application of the normalizing scale factor 1.239 ± 0.111 (binned exclusively). The expected number of events at each cut is predicted by the rate measured in the W+jets control region. The uncertainty originating from statistics in the control region is indicated by the solid band while the additional systematic uncertainties are indicated by the shaded band. (It should be noted that the x-axis here represents the bin and not the cut, so events in the 40 GeV bin do not contain events from 60 GeVand 80 GeVand so-on)

Table 6.5: The total number of events containing at least one trackful CR jet in the validation region at 3 different E_{T} cuts (binned inclusively). The expected number of events at each cut is predicted by the rate measured in the W+jets control region is shown with the corresponding normalizing shift and systematic uncertainty.

	40GeV	60GeV	80GeV
Total Trackful CR Jets in W Control Region	7055	3759	2171
Expected Trackful CR Jet Events Before Shift ($Z \to ee$)	245.6 ± 35.1	136.5 ± 23.8	81.3 ± 18.5
Expected Trackful CR Jet Events Before Shift ($Z \to \mu\mu$)	249.1 ± 35.1	134.1 ± 23.1	77.8 ± 17.7
Total Expected Trackful CR Jet Events Before Shift	494.7 ± 70.2	270.6 ± 46.9	159.1 ± 36.2
Expected Trackful CR Jet Events ($Z \to ee$)	304.4 ± 46.7	169.1 ± 29.4	100.7 ± 20.9
Expected Trackful CR Jet Events ($Z \to \mu\mu$)	308.7 ± 46.9	166.2 ± 28.6	96.4 ± 20.0
Total Expected Trackful CR Jet Events	613.0 ± 93.5	335.3 ± 58.0	197.1 ± 40.9
Observed Trackful CR Jet Events ($Z \to ee$)	292	154	96
Observed Trackful CR Jet Events ($Z \to \mu\mu$)	321	179	116
Total Observed Trackful CR Jet Events	613	333	212

CHAPTER 7. RESULTS

The total number of events containing at least one CR jet are summarized in Table 7.1 and Fig 7.1 alongside the expected values. No excess over the expected background is observed.

Table 7.1: The total number of events with at least one CR jet in the signal region at 3 different E_{T} cuts. The expected number of events is predicted by the rate measured in the W+jets control region and shown with the corresponding shift and total systematic uncertainty.

	40GeV	60GeV	80GeV
Expected CR Jet Events Before Shift ($Z \to ee$)	67.9 ± 6.6	13.2 ± 1.8	5.4 ± 1.3
Expected CR Jet Events Before Shift ($Z \to \mu\mu$)	72.9 ± 7.0	13.4 ± 1.8	5.2 ± 1.2
Total Expected CR Jet Events Before Shift	140.8 ± 13.7	26.6 ± 3.6	10.6 ± 2.5
Expected CR Jet Events ($Z \to ee$)	84.1 ± 10.6	16.4 ± 2.5	6.7 ± 1.4
Expected CR Jet Events ($Z \to \mu\mu$)	90.4 ± 11.4	16.6 ± 2.5	6.5 ± 1.4
Total Expected CR Jet Events	174.5 ± 22.0	33.0 ± 5.0	13.2 ± 2.8
Observed CR Jet Events ($Z \to ee$)	81	20	10
Observed CR Jet Events ($Z \to \mu\mu$)	77	15	6
Total Observed CR Jet Events	158	35	16

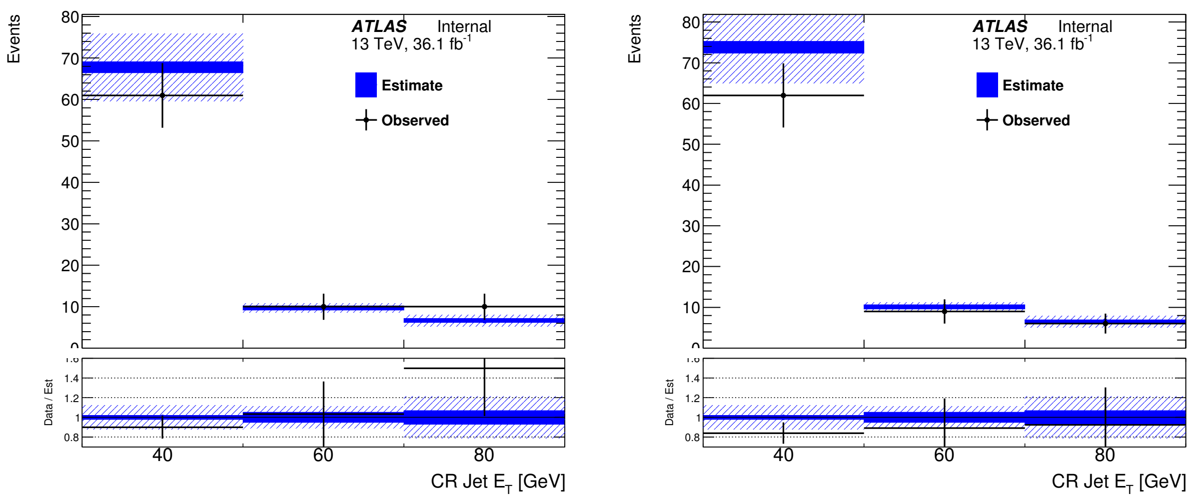

Figure 7.1: The total number of events with at least one CR jet in the signal region at 3 different E_{T} cuts (binned exclusively) for the $Z \to ee$ (left) and $Z \to \mu\mu$ (right). The expected number of events at each cut is predicted by the rate measured in the W+jets control region. Uncertainty due to statistics in the control region are shown as a solid band while the shaded band corresponds to the additional systematic uncertainties on the estimate as described in Sec 8.1

CHAPTER 8. SYSTEMATICS

The background estimation is completely data-driven and therefore the only source of systematic error is the difference in the CR jet probability at different jet multiplicities (see Sec 8.1). Additional systematics affect the signal MC and enter into the calculation of the sensitivity and limits and are described in the summary at the end of this section.

8.1 CR Jet Probability

As noted in Section 6.4, the statistical uncertainty on the measurement of the CR jet probability is treated as a systematic uncertainty. A systematic is applied to account for the difference in QCD contamination of the $W \to e\nu$ and $W \to \mu\nu$ channels which also adds an additional systematic uncertainty. Additionally a scale factor and corresponding uncertainty of 1.239 ± 0.111 is applied to the estimate from the W region to better match the data in the Z validation region (described in Section 6.7.0.1). The total uncertainty on our background estimation is shown in Table 6.3. This systematic varies from 12% for the $E_{\mathrm{T}} > 40$GeV cut to 21% for the $E_{\mathrm{T}} > 80$GeV cut.

This systematic is the only one which affects the background estimate as described in Section 6.

8.2 Jet Energy Scale (JES)

The uncertainty associated with the Jet Energy Scale (JES) is provided by the JetCalibTools package. The recommended procedure from Moriond2017 defined in is followed: the effect of the JES variation is compared to the nominal scale for each of four reduced uncertainty sets (the full uncertainty set contains about 100 different uncertainties). The fact that the differences with respect to the nominal yield are similar in all the configurations indicates that the analysis is not sensitive to jet correlations. Hence, the difference given by the first set of parameters is taken as the systematic uncertainty on the Jet Energy Scale. The average of this systematic for each sample is summarized in Table 8.1.

The jets used in this analysis have a low EMF, however the standard JES systematics are determined using mostly high EMF jets. A lepton jets analysis[30] followed the strategy used in the in situ jet pseudorapidity intercalibration analysis but evaluating the jet energy correction as a function of jet EMF. The relative jet calorimeter response was measured by balancing the transverse momenta of dijets in cleanly selected events from 2015 data. The systematic uncertainty is obtained by comparing the asymmetry in data to the balance in MC.

This systematic only meaningfully affects the samples with $m_\Phi = 125$GeV, the largest value being $\approx 8\%$.

8.3 Jet Energy Resolution (JER)

The jet energy resolution is measured in dijets data using the tag-and-probe method (see Appendix C for details). The uncertainty associated with the jet energy resolution (JER) is determined by the application of the standard JERTool from the JetResolution package. It enters the calculation through the CR jet reconstruction efficiency and the extrapolation of that efficiency to other particle lifetimes. This systematic is the second largest systematic for low-mass samples becoming much less significant for the high-mass samples, summarized in Table 8.1.

8.4 Pileup Reweighting

The PileupReweightingTool provides an event pileup weight as a function of μ that makes the μ distribution of the MC match that of the data sample. The number of reconstructed vertices is directly related to how much pileup there was in a given event. Studies comparing the number of vertices in data and MC for the same μ have shown a mismodelling in MC that has to be corrected using a scale factor for μ between data and MC. The standard recommendation for this scale factor, $1.16^{+0.07}_{-0.16}$, is applied. The nominal value, 1.16, is applied to get the nominal pileup weight. The variation of the scale factors by the errors give variations for the pileup weight used to determine the systematic uncertainties associated with pileup. The uncertainties in the final yields given by this tool are quoted in Table 8.1 for all signal MC samples.

This systematic varies from $\approx 19\%$ for the low mass samples to $\approx 5\%$ for the high mass samples and is therefore one of the most significant systematics affecting the limits.

8.5 Luminosity

The uncertainty in the integrated luminosity is 2.1%. It is derived following a methodology detailed in [9] from a calibration of the luminosity scale using x-y beam-separation scans performed in August 2015 and May 2016.

8.6 Electrons

References for the measurement of lepton trigger systematics can be found in Section 4.1. It contains the systematic and statistical error on the trigger SF respectively.

Reconstruction (Reco) and identification (ID) efficiency and its systematic uncertainties are provided by the AsgElectronEfficiencyCorrectionTool. The electron efficiency scale factors have been calculated using the full data of 2015 and 2016 from J/ψ and Z measurements at low and high p_{T} respectively (using a tag and probe method). The ID efficiency scale factor includes the combined cuts of impact parameter significance and on $|z_0 sin\theta|$ and is available from $p_{\mathrm{T}} > 7$GeV. The isolation efficiency scale factor is also provided. For the current recommendation, scale factors for $p_{\mathrm{T}} > 150$GeV are unity due to lack of statistics to measure the scale factors. Therefore a systematic uncertainty of additional $\pm 2\%$ is assigned for leptons above 150GeV. Three independent systematic sources are considered : the ID efficiency, reconstruction efficiency, and isolation efficiency.

Energy scale and resolution systematic uncertainties have been considered, however these are not dominant systematic sources. This analysis is very weakly sensitive to the electron energy scale and resolution.

All of the aforementioned electron systematics result in variations $< 0.1\%$ and are thus negligible compared to the other known sources.

8.7 Muons

For the muons, the trigger tool returns two components : the systematics error and the statistical error on the trigger SF. Systematics are obtained by a variation of $\pm 1\sigma$ of these errors.

Reconstruction, isolation and track-to-vertex association (d_0 significance and $z_0 sin\theta$) scale factors are calculated using $Z \rightarrow \mu\mu$ and $J/\psi \rightarrow \mu\mu$ (tag and probe) events in the full data of 2015, which corresponds to 3.2fb^{-1}. Due to the fact that the J/ψ measurement is valid below 15GeV and the Z measurements are more accurate above 15GeV, separate systematic uncertainties are used in the low-p_{T} and high-p_{T} regions (below/above 15GeV). This analysis relies only on those made from the Z measurement.

The isolation scale factor and its systematic uncertainties are supported in the range of 10GeV $< p_{\mathrm{T}} <$ 500GeV. The scale factor of the combined cuts on the impact parameter significance and the $|z_0 sin\theta|$ are also provided.

All muon associated systematic uncertainties have an effect $< 0.1\%$ and are thus negligible compared to the other known sources.

8.8 PDF Uncertainty

The parton density function (PDF) of the proton is an essential component of Monte Carlo simulations. The PDF is determined using cross-section data through a number of different approaches [2, 41, 22]. The differences between these PDFs is used as an additional systematic uncertainty.

The PDF4LHC recommendations for determining the PDF uncertainty are followed. Rather than generating events with different PDFs the existing events are reweighted to approximate how they would appear if generated with the different weights.

$$w = \frac{PDF_{new}(x_1, f_1, Q) \times PDF_{new}(x_2, f_2, Q)}{PDF_{old}(x_1, f_1, Q) \times PDF_{old}(x_2, f_2, Q)} \tag{8.1}$$

This reweighting calculation is performed by the LHAPDF tool [25].

The MC samples for this analysis were generated using the NNPDF set [22]. The NNPDF set does not provide a set of error PDFs. Instead of a central value and some error PDFs with parameters varied they provide an ensemble of PDFs. This ensemble is made from fits to the ensemble test on the input data. In that way they say that the best value is the mean of all the ensembles and the uncertainty is the standard deviation of the weights from the mean. For all signal MC samples this systematic uncertainty is 0.5%.

8.9 Lifetime Reweighting

The lifetime reweighting procedure described in Section 9.2.1 has a limited number of events (particularly at long lifetimes) and thus the statistical uncertainty becomes significant at extremely large and small reweighting values. This uncertainty is folded into the efficiencies as a function of proper lifetime and shown in Figure 9.5. The uncertainty from this procedure increases to unity at lifetimes below 1cm and above 100m. To reduce this uncertainty additional MC samples could be generated at other lifetimes.

8.10 Summary

A breakdown of how each independent systematic affects the estimated limit is shown in Table **??** for a single signal MC sample. A summary of these systematics for each signal MC sample is in Table 8.1. All systematics are listed for a lifetime of 1m.

Table 8.1: The average of each systematic at a lifetime of 1m for each signal MC sample. The total includes all sources of uncertainty, including the 2.1% uncertainty on the luminosity.

m_Φ [GeV]	m_{Z_d} [GeV]	Bkg Estimate	JER	JES	$lowEMF$	PU	$Total$
125	5	12.61%	1.23%	$^{+3.50\%}_{-3.84\%}$	$^{+4.4\%}_{-9.1\%}$	$^{+14.66\%}_{-15.97\%}$	$^{+20.18}_{-22.65}\%$
125	10	12.61%	0.68%	$^{+2.76\%}_{-3.63\%}$	$^{+4.4\%}_{-9.1\%}$	$^{+19.34\%}_{-13.07\%}$	$^{+23.77}_{-20.75}\%$
125	15	12.61%	5.04%	$^{+2.95\%}_{-2.06\%}$	$^{+4.8\%}_{-4.2\%}$	$^{+10.38\%}_{-13.30\%}$	$^{+18.12\%}_{-19.06\%}$
250	10	15.15%	0.43%	$^{+1.47\%}_{-0.17\%}$	$< 0.1\%$	$^{+4.71\%}_{-6.36\%}$	$^{+16.08\%}_{-16.57\%}$
250	50	15.15%	0.14%	$^{+0.11\%}_{-0.24\%}$	$< 0.1\%$	$^{+5.64\%}_{-6.44\%}$	$^{+16.30\%}_{-16.60\%}$
250	100	15.15%	0.07%	$^{+0.36\%}_{-0.09\%}$	$< 0.1\%$	$^{+4.24\%}_{-5.26\%}$	$^{+15.88\%}_{-16.17\%}$
500	20	21.21%	0.06%	$^{+0.20\%}_{-0.22\%}$	$< 0.1\%$	$^{+4.88\%}_{-3.76\%}$	$^{+21.87\%}_{-21.64\%}$
500	100	21.21%	0.08%	$^{+0.30}_{-0.25}\%$	$< 0.1\%$	$^{+14.35\%}_{-9.09\%}$	$^{+25.70\%}_{-23.17\%}$
500	200	21.21%	0.03%	$^{+0.15\%}_{-0.27\%}$	$< 0.1\%$	$^{+6.28\%}_{-3.74\%}$	$^{+22.22\%}_{-21.64\%}$

CHAPTER 9. LIMITS

With the background estimate made, it is possible to determine the experimental sensitivity to our signal model. Limit setting is an important part of an experimental science. This analysis determines these limits using the CL_s method and extends the results to other lifetimes using a reweighting technique, each outlined in detail in the following sections.

9.1 CL_s Method

The CLs method is commonly used for setting upper limits (or exclusion limits) in high-energy physics[51]. It is important to note that while this is referred to as a "confidence level", it is not the same as the "confidence interval" often used in statistics.

The method is neither purely frequentist nor Bayesian, instead its motivation is practical - it seeks to modify the frequentist CL_{s+b} to avoid false exclusions when the experiment is insensitive to the signal. The CL_s limit corresponds to the frequentist limits when the experiment is fully sensitive, degrading in regions where an experiment is insensitive.

The Poisson distribution is an appropriate model in circumstances where the occurrence of one event doesn't affect the probability of another, the rate of occurrence is a constant, and the number of events is an integer. For a simple single-bin counting experiment (which was used for this analysis) these are all guaranteed and thus we can assume a Poissonian probability density function (pdf) of

$$P(N_{obs}, N_{mean}) = \sum_{k=0}^{N_{obs}} e^{-N_{mean}} \frac{N_{mean}^k}{k!} \tag{9.1}$$

Using this pdf, we can assume that in an experiment where we observe N_{obs} events, expect N_{bkg} background events and $\mu \times N_{sig}$ signal events, we can compute the quantities

$CL_b = P(N_{obs}, N_{bkg})$ (the probability to obtain a result less compatible with the signal than the observed one in the background-only hypothesis)

and

$CL_{s+b} = P(N_{obs}, N_{bkg} + \mu \times N_{sig})$ (the probability to obtain a result less compatible with the signal than the observed result, assuming the signal hypothesis)

The frequentist approach when setting limits would be to simply use the quantity CL_{s+b}, and in the case that $N_{bkg} \to 0$ this works as $CL_{s+b} \to CL_s$, however if N_{bkg} is large relative to N_{sig} (which is to be expected in most experiments at ATLAS) then CL_{s+b} will be large despite a poor experiment.

The CLs method uses the ratio $CL_s = \frac{CL_{s+b}}{CL_b} < 1 - \alpha$ where α is the desired confidence level (usually 95%), to decrease the CL in regions where the experiment is insensitive.

One notable observation with this method is that if 0 events are observed, then any model predicting less than 3 events at a 95% confidence level cannot be excluded, regardless of the amount of expected background.

9.1.1 Example Calculation

For example, lets say that our background estimate tells us to expect 200 events ($N_{bkg} = 200$) while our signal model predicts 10 events ($N_{sig} = 10$).

If we observe 202 events ($N_{obs} = 202$) then the probability of observing 202 events or fewer in the null (background-only) hypothesis is given by $CL_b = P(202, 200) = 0.575$ Furthermore, the probability of observing 202 events or fewer in the signal+background hypothesis (using a signal strength $\mu = 1$) is given by $CL_{s+b} = P(202, 200 + 10) = 0.305$.

These are then combined to obtain $CL_s = \frac{CL_{s+b}}{CL_b} = 0.530$

To determine the exclusion limit on our signal we must modify the signal strength μ such that $CL_s = 0.05$ (i.e. we want to know the signal strength at which the probability of measuring the signal+background hypothesis to be true and the background-only hypothesis to be false is less

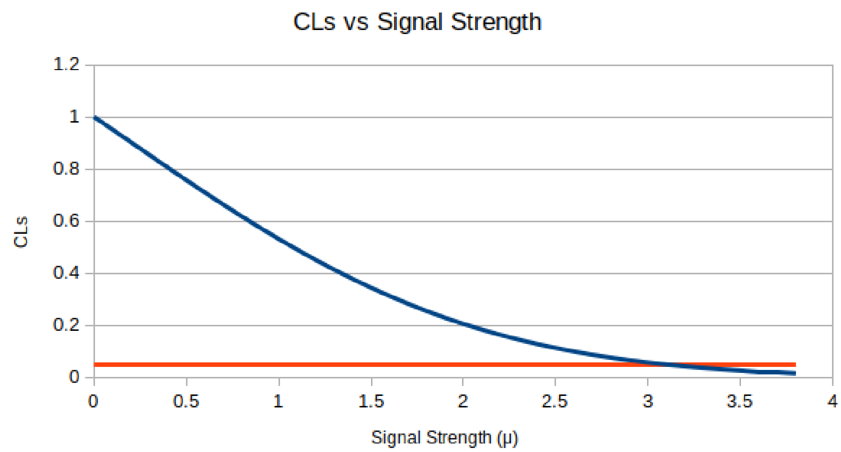

Figure 9.1: The value of CLs vs signal strength μ.

than 5%). To do this we run the calculation for several values of μ, as shown in Fig 9.1. The point where the value of CLs reaches 0.05 corresponds to roughly $\mu = 3.1$.

This tells us that at least $\mu \times N_{sig} = 31$ signal events must be present before the signal+background hypothesis reaches a 95%, and thus with these results we cannot claim a discovery.

9.1.2 Inclusion of Systematic Uncertainty

In order to properly account for the effect of systematics on the limit determined by the CLs method, a probability density function for each systematic needs to be included in the calculation. These pdfs are generally assumed to be Gaussian, with the standard deviation σ corresponding to the uncertainty of the measurement.

To produce the results of this calculation the Monte Carlo (MC) method is used, in which each variable is given a random value determined by its pdf. As a larger number of "toys" (generations) are performed the results converge to the true distribution.

The single bin counting limits determined in this analysis were determined using the HistFitter statistical framework which utilizes RooStats [48]. The exclusion limit for each jet E_T cut and are summarized in Table 9.1.

Table 9.1: The number of signal events required to measure an excess with a 95% CL over background for different CR jet E_{T} cuts.

E_T Cut [GeV]	$N_{\mathrm{sensitivity}}$
40	50
60	18
80	13

9.2 Cross Section Limit

To use our CLs limit to determine a limit on the cross section of the signal model we first need several efficiencies (detailed in Section 5.5.1), however these efficiencies are not constants as a function of the proper lifetime of the Z_d.

$$BR \times \sigma(\tau) = \frac{N_{95\%CL}^{sensitive}}{\mathcal{L} \times \epsilon_{Zreco} \times \epsilon_{CRreco}(\tau) \times \epsilon_{InHCal}(\tau)} \tag{9.2}$$

9.2.1 Lifetime Reweighting

Setting any limits in a study with long-lived particles (LLPs) requires extending the results to a wide range of lifetimes, however generating MC samples at several proper lifetimes is resource intensive and in many cases inefficient. For this analysis particle decays are only caught if they decay within the HCal (the barrel of which lies between 2.28m and 4.25m in radial distance from the IP). If a sample is generated with a very short proper lifetime (say 10mm), then almost none of the generated events will contain the objects of interest - decaying further inside the detector. Similarly if a sample is generated with a very long proper lifetime (for instance 100m) then the majority of particles will decay outside the detector - once more resulting in almost no objects of interest.

To avoid spending precious computing resources a re-weighting procedure was devised to allow results from a sample with one proper lifetime to be extended to a wide range of other proper lifetimes. First a sample was generated at a proper lifetime of 1m (ensuring a significant portion of

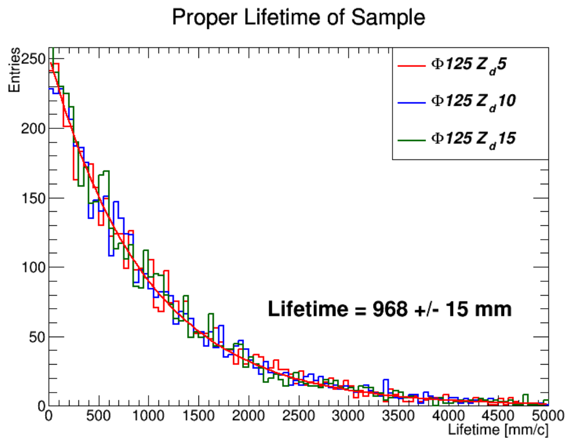

Figure 9.2: An exponential fit to the rest frame lifetime distribution of several signal MC samples. The fit results has an uncertainty which is used as an additional systematic uncertainty on the subsequent limits.

decays would occur in the HCal). Next, a plot of the rest frame lifetime of all LLPs in the sample was produced and fitted with an exponential decay function ($A_1 exp(-\frac{\tau_0}{\tau_1})$) as shown in Figure 9.2. The proper lifetime of the sample is defined as τ_1 and thus the sample contains a total number of events $N_1^{events} = \int_0^\infty A_1 exp(-\frac{\tau}{\tau_1})d\tau = A_1\tau_1$.

Another proper lifetime, τ_2 is now chosen. To maintain normalization the number of total events (the integral of the function over all τ) is the same, $N_2^{events} = N_1^{events} = A_2\tau_2$ and thus an expression can be written for the weight required to shift the distribution to a new proper lifetime τ_2. Each event is assigned a new weight as a function of the rest frame lifetime of the LLP $w = \frac{A_2}{A_1} exp(-(\frac{1}{\tau_2} - \frac{1}{\tau_1})\tau_0)$. The results of this procedure are shown in Figure 9.4.

9.2.1.1 Acceptance in the HCal

Once a sample is re-weighted according to the rest frame lifetime, the proportion of LLPs decaying within the HCal (those with $2.28m < L_{xy} < 4.25m$) can be determined as a function of proper lifetime. This acceptance is shown in Figure 2.12 for each of the signal MC samples. The official MC production request was made with the proper lifetime corresponding to the peak of this distribution.

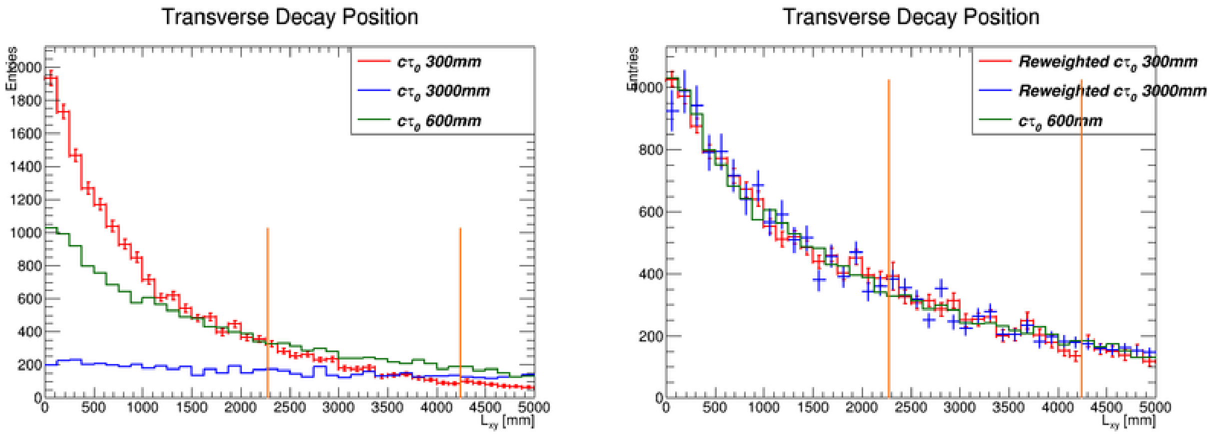

Figure 9.4: The transverse decay position of LLPs (L_{xy}) for a sample produced at 3 different proper lifetimes (300mm, 600mm, and 3000mm). All samples are reweighted to 600mm and then compared to ensure that the reweighting procedure is returning accurate results. The vertical lines correspond to the HCal barrel ($2.28m < L_{xy} < 4.25m$). Rest frame lifetime is shown prior to reweighting (left) and after reweighting (right).

9.2.1.2 Reconstruction Efficiencies

The Z and CR jet reconstruction efficiencies (detailed in Sections 5.5.1) are each re-evaluated after all events have been reweighted. Each of these efficiencies show behavior as a function of proper lifetime due to some underlying physics.

The CR jet reconstruction efficiency (shown in Figure 9.5) tends to decrease as a function of proper lifetime. At extremely short lifetimes only the most boosted particles reach the HCal, resulting in a bias towards higher E_T LLPs which reach the HCal quickly (easily passing the jet timing cut). This results in a higher CR jet reconstruction efficiency at shorter lifetimes. Similarly, at longer lifetimes a bias is created toward lower E_T LLPs which decay out-of-time with the event. The result is a decreased CR jet reconstruction efficiency. This efficiency was determined as a function of the proper lifetime for each sample, results are shown in Figure 9.5.

Prior to any jet selection, the Z reconstruction efficiency is independent of proper lifetime (see Fig 9.6), however as explained above shorter lifetimes select higher E_{T} CR jets whilst longer lifetimes select lower E_{T} CR jets. The momentum of the Z and the CR jet should always be in balance, and so after CR jet selection is applied the Z reconstruction efficiency can also change as

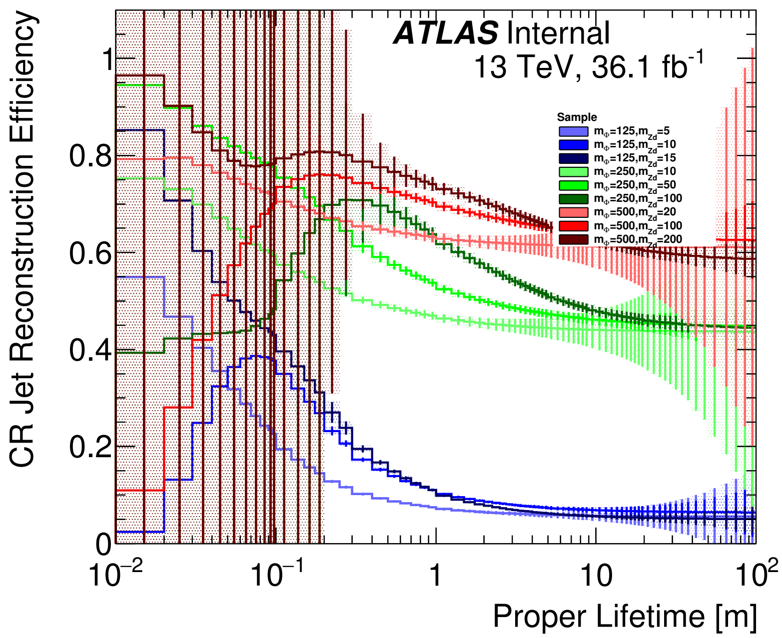

Figure 9.5: The CalRatio jet reconstruction efficiency as a function of proper lifetime for each sample. The error bands shown are statistical and grow as a byproduct of the reweighting procedure. This uncertainty is included as a systematic error wherever the lifetime reweighting is applied.

a function of lifetime. The Z reconstruction efficiency is affected in a complex way : at lower E_{T} the leptons from the Z have less momentum and thus more likely to be lost, however they are also more isolated and have better charge ID. As a result the shape of the Z reconstruction efficiency for different samples are highly dependent on the p_{T} spectrum of the Z in that sample. The resulting Z reconstruction efficiency after CR jet selection is shown in Fig 9.7 for each signal MC sample.

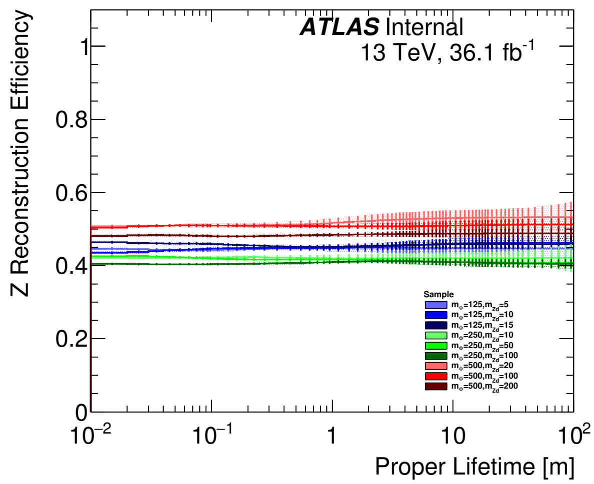

Figure 9.6: The Z reconstruction efficiency (prior to CR jet selection). As expected the efficiency is independent of proper lifetime.

9.2.2 Observed Limits

Using Equation 9.2 we can combine the sensitivity (from Table 9.1) with the efficiencies as a function of proper lifetime and produce the following plots of the observed cross-section limit of the process $H \to ZZ_d$.

Jets in the lower mass samples ($m_{\Phi} = 125\mathrm{GeV}$) have much less energy than those in the higher mass samples, which results in a smaller CR jet reconstruction efficiency (see Fig 9.5). These samples are also more affected by the jet systematics described in Sec 8.3, 8.2.

Combining the CR reconstruction efficiency and the expected sensitivity allows the determination of which E_{T} cut can provide the tightest limits for each MC sample. The cut choice was found to be the same for each mediator mass m_{Φ} and are summarized in Table 9.1.

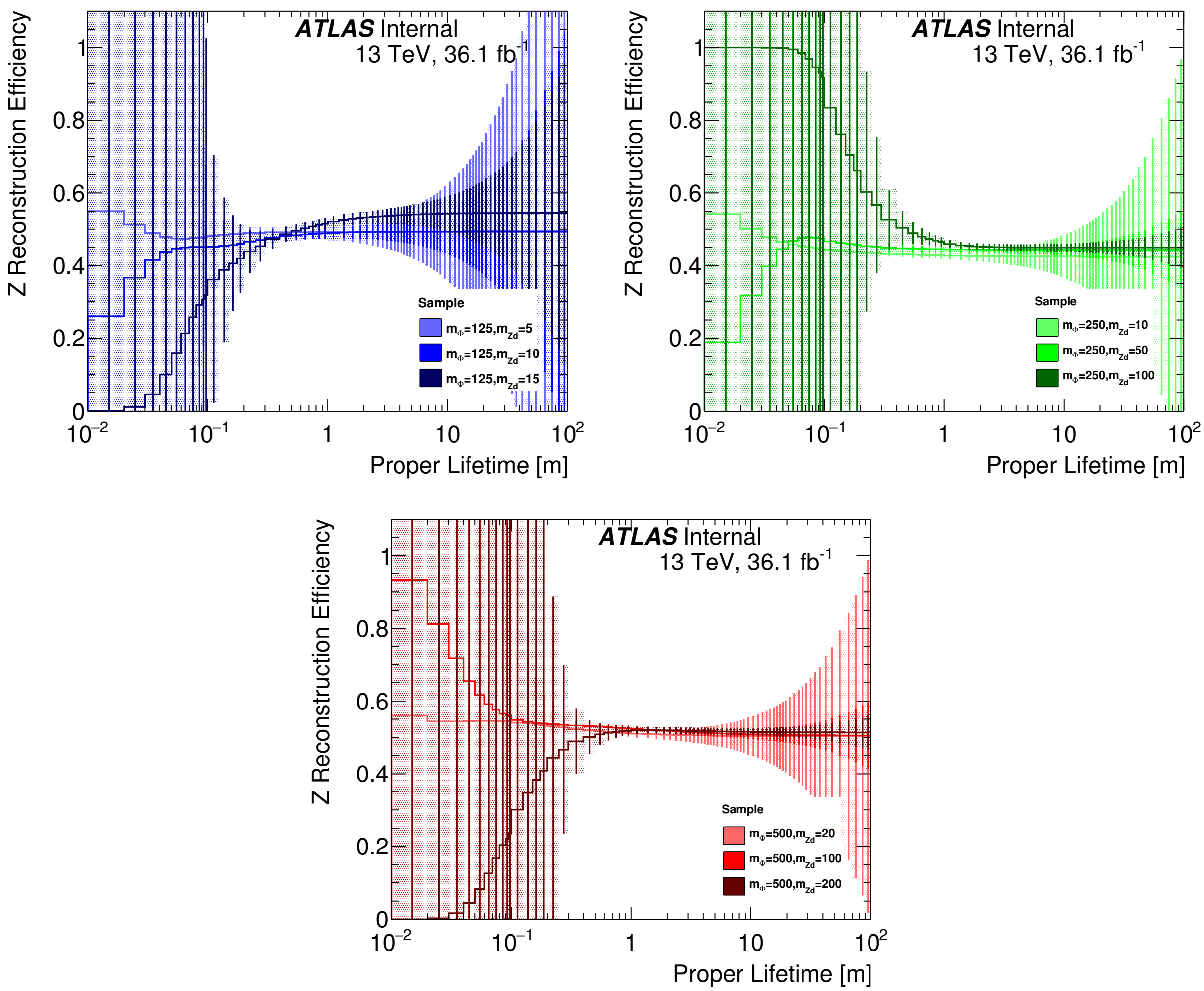

Figure 9.7: The Z reconstruction efficiency (after CR jet selection) for each MC Sample. The efficiency remains flat as a function of proper lifetime (within uncertainty).

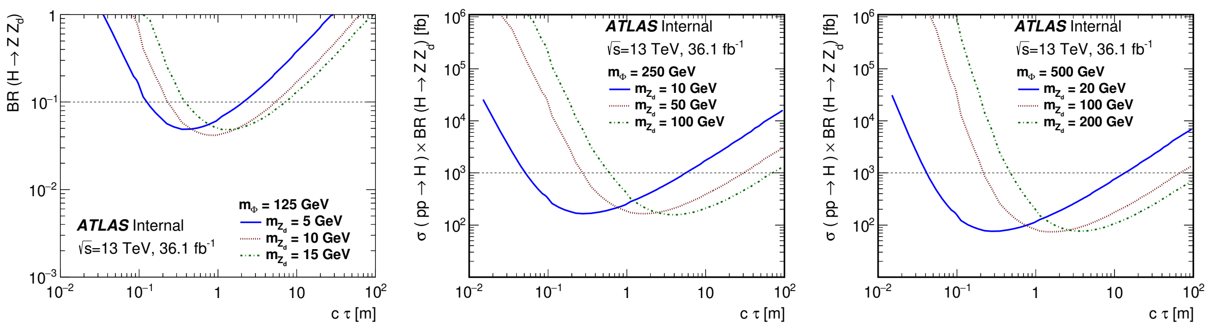

Figure 9.8: The expected 95% CLs limit on $\sigma \times BR$ for $\Phi \rightarrow ZZ_d$ at different mass points as a function of the proper lifetime of the Z_d, using the known cross section of the 125GeV Higgs (left). The center and right plots correspond to the limit on σ for higher mass mediators. The increased jet E_{T} cut results in greater sensitivity in the high mass regions.

For proper lifetimes of $c\tau \approx mm$ distances prompt searches are expected to place better limits and in the region above $100m$ or so $E_{\mathrm{T}}^{\mathrm{miss}}$ searches should have greater performance.

In addition, using the cross-section of the known SM Higgs at 125 GeV(48.5pb) allows limits to be placed on the branching fraction for this process (shown in Figure 9.8).

9.2.2.1 High Mass Mediators

While the high mass samples are subject to increased uncertainty (primarily due to the decrease in statistics in the control region at higher CR jet E_{T} cuts) the decreased background results in considerable additional sensitivity.

The limit on the cross section for a massive mediator $\Phi \rightarrow ZZ_d$ is shown in Figure **??**.

CHAPTER 10. CONCLUSION

A search for the decay of a heavy scalar mediator decaying to a single long-lived particle (recoiled against a standard model Z) is presented. The analysis is based on $36.1 fb^{-1}$ of pp collisions at $\sqrt{s} = 13 TeV$ collected in 2015 and 2016 with the ATLAS detector at the LHC.

No significant excess of events is observed over the background estimate, which has a systematic uncertainty dominated by statistics in the control region and the effects of pileup reweighting. The limits are set on the Z_d for different proper lifetimes and masses.

The number of free parameters in models with long-lived particles currently makes model-independent exclusions of the available dark-matter phase space impossible to make. However this analysis is focused on specific signatures and thus the results can be reinterpreted for models when desired.

There are a number of things to be better understood in future iterations of this analysis. Multivariate analysis techniques could be used to improve signal efficiency (particularly for the low mass samples). Further the need for the correction factor (specified in Sec 6.7) lacks a solid explanation.

BIBLIOGRAPHY

[1] M. e. a. Aaboud. Measurement of the Inelastic Proton-Proton Cross Section at $\sqrt{s} = 13$TeV with the ATLAS Detector at the LHC. *Phys. Rev. Lett.*, 117(18):182002, 2016.

[2] H. e. a. Abramowicz. Combination of measurements of inclusive deep inelastic $e^{\pm}p$ scattering cross sections and QCD analysis of HERA data. *Eur. Phys. J.*, C75(12):580, 2015.

[3] S. e. a. Arrenberg. Working Group Report: Dark Matter Complementarity. In *Proceedings, 2013 Community Summer Study on the Future of U.S. Particle Physics: Snowmass on the Mississippi (CSS2013): Minneapolis, MN, USA, July 29-August 6, 2013*, 2013.

[4] ATLAS Collaboration. The atlas experiment at the cern large hadron collider. *Journal of Instrumentation*, 3(08):S08003, 2008.

[5] ATLAS Collaboration. Commissioning of the ATLAS Muon Spectrometer with Cosmic Rays. *Eur. Phys. J.*, C70:875–916, 2010.

[6] ATLAS Collaboration. Luminosity Determination in *pp* Collisions at $\sqrt{s}$= 7 TeV using the ATLAS Detector at the LHC. *Eur. Phys. J. C*, 71(arXiv:1101.2185. CERN-PH-EP-2010-069):1630. 24 p, Jan 2011. Comments: 24 pages plus author list (36 pages total). 9 Figures, 10 Tables, submitted to Journal EPJC.

[7] ATLAS Collaboration. Luminosity Determination in *pp* Collisions at $\sqrt{s} = 7$ TeV Using the ATLAS Detector at the LHC. *Eur. Phys. J.*, C71:1630, 2011.

[8] ATLAS Collaboration. Studies of the performance of the ATLAS detector using cosmic-ray muons. *Eur. Phys. J.*, C71:1593, 2011.

[9] ATLAS Collaboration. Improved luminosity determination in pp collisions at $\sqrt{s} = 7$ TeV using the ATLAS detector at the LHC. *Eur. Phys. J.*, C73(8):2518, 2013.

[10] ATLAS Collaboration. Jet energy measurement with the atlas detector in proton-proton collisions at $\sqrt{s} = 7$ tev. *Eur. Phys. J. C*, 73:2304, 2013.

[11] ATLAS Collaboration. ATLAS Run 1 Pythia8 tunes. Technical Report ATL-PHYS-PUB-2014-021, CERN, Nov 2014.

[12] ATLAS Collaboration. Electron efficiency measurements with the ATLAS detector using the 2012 LHC proton-proton collision data. *ATLAS-CONF-2014-032*, Jun 2014.

[13] ATLAS Collaboration. Search for pair produced long-lived neutral particles decaying in the ATLAS hadronic calorimeter in pp collisions at $\sqrt{s} = 8$ TeV. Technical Report ATLAS-CONF-2014-041, CERN, Geneva, Jul 2014.

[14] ATLAS Collaboration. Expected performance of missing transverse momentum reconstruction for the ATLAS detector at $\sqrt{s} = 13$ TeV. Technical Report ATL-PHYS-PUB-2015-023, CERN, Geneva, Jul 2015.

[15] ATLAS Collaboration. Monte Carlo Calibration and Combination of In-situ Measurements of Jet Energy Scale, Jet Energy Resolution and Jet Mass in ATLAS. Technical Report ATLAS-CONF-2015-037, CERN, Geneva, Aug 2015.

[16] ATLAS Collaboration. Selection of jets produced in 13TeV proton-proton collisions with the ATLAS detector. Technical Report ATLAS-CONF-2015-029, CERN, Geneva, Jul 2015.

[17] ATLAS Collaboration. Electron efficiency measurements with the ATLAS detector using the 2015 LHC proton-proton collision data. Technical Report ATLAS-CONF-2016-024, CERN, Geneva, Jun 2016.

[18] ATLAS Collaboration. Measurement of jet charge in dijet events from $\sqrt{s}$=8 TeV pp collisions with the ATLAS detector. *Phys. Rev.*, D93(5):052003, 2016.

[19] ATLAS Collaboration. Muon reconstruction performance of the atlas detector in proton–proton collision data at 13 tev. *The European Physical Journal C*, 76(5):292, May 2016.

[20] ATLAS Collaboration. LHC Guide. Mar 2017.

[21] ATLAS Collaboration. Quark versus Gluon Jet Tagging Using Charged Particle Multiplicity with the ATLAS Detector. Technical Report ATL-PHYS-PUB-2017-009, CERN, Geneva, May 2017.

[22] R. D. e. a. Ball. Parton distributions for the LHC Run II. *JHEP*, 04:040, 2015.

[23] A. Barnacka, L. Bogacz, M. Grudziska, M. Janiak, N. Komin, G. Lamanna, and R. Moderski. Monte carlo simulations for the cherenkov telescope array observatory using pl-grid e-infrastructure. 13:113, 01 2012.

[24] L. Baudis. Dark matter searches. *Annalen Phys.*, 528:74–83, 2016.

[25] A. Buckley, J. Ferrando, S. Lloyd, K. Nordstrm, B. Page, M. Rfenacht, M. Schnherr, and G. Watt. LHAPDF6: parton density access in the LHC precision era. *Eur. Phys. J.*, C75:132, 2015.

[26] W. Buttinger. Using Event Weights to account for differences in Instantaneous Luminosity and Trigger Prescale in Monte Carlo and Data. Technical Report ATL-COM-SOFT-2015-119, CERN, Geneva, May 2015.

[27] M. Cacciari and G. P. Salam. Pileup subtraction using jet areas. *Phys. Lett.*, B659:119–126, 2008.

[28] M. Cacciari, G. P. Salam, and G. Soyez. The Catchment Area of Jets. *JHEP*, 04:005, 2008.

[29] B. J. Carr, K. Kohri, Y. Sendouda, and J. Yokoyama. New cosmological constraints on primordial black holes. *Phys. Rev.*, D81:104019, 2010.

[30] G. Ciapetti, M. Del Gaudio, M. Diamond, S. Giagu, R. Les, A. Policicchio, M. Schioppa, M. Testa, and M. Verducci. Search for long-lived neutral particles decaying into lepton jets in pp collisions at $\sqrt{s} = 13$ TeV with the ATLAS detector. Technical Report ATL-COM-PHYS-2016-010, CERN, Geneva, Jan 2016.

[31] D. Clowe, A. Gonzalez, and M. Markevitch. Weak lensing mass reconstruction of the interacting cluster 1E0657-558: Direct evidence for the existence of dark matter. *Astrophys. J.*, 604:596–603, 2004.

[32] E. Corbelli and P. Salucci. The extended rotation curve and the dark matter halo of m33. *Monthly Notices of the Royal Astronomical Society*, 311(2):441, 2000.

[33] H. Davoudiasl, H.-S. Lee, I. Lewis, and W. J. Marciano. Higgs decays as a window into the dark sector. *Phys. Rev. D*, 88:015022, Jul 2013.

[34] L. Dell'Asta and S. M. Shaw. Muon trigger public plots with full 2016 dataset. Technical Report ATL-COM-DAQ-2017-005, CERN, Geneva, Jan 2017.

[35] J. Diemand and B. Moore. The Structure and Evolution of Cold Dark Matter Halos. *Advanced Science Letters*, 4:297–310, Feb. 2011.

[36] S. e. a. Durr. Ab-Initio Determination of Light Hadron Masses. *Science*, 322:1224–1227, 2008.

[37] J. Ellis. TikZ-Feynman: Feynman diagrams with TikZ. *Comput. Phys. Commun.*, 210:103–123, 2017.

[38] C. Englert, A. Freitas, M. M. Mhlleitner, T. Plehn, M. Rauch, M. Spira, and K. Walz. Precision Measurements of Higgs Couplings: Implications for New Physics Scales. *J. Phys.*, G41:113001, 2014.

[39] C. W. Fabjan and F. Gianotti. Calorimetry for Particle Physics. *Rev. Mod. Phys.*, 75(CERN-EP-2003-075):1243–1286. 96 p, Oct 2003.

[40] D. Griffiths. *Introduction to Elementary Particles*. WILEY-VCH Verlag GmbH and Co. KGaA, second, revised edition, 2008.

[41] L. A. Harland-Lang, A. D. Martin, P. Motylinski, and R. S. Thorne. Parton distributions in the LHC era: MMHT 2014 PDFs. *Eur. Phys. J.*, C75(5):204, 2015.

[42] S. Hawking. Gravitationally collapsed objects of very low mass. *mnras*, 152:75, 1971.

[43] A. Kashlinsky. LIGO gravitational wave detection, primordial black holes and the near-IR cosmic infrared background anisotropies. *Astrophys. J.*, 823(2):L25, 2016.

[44] R. Kwee-Hinzmann, G. Bregliozzi, R. Bruce, F. Cerutti, L. S. Esposito, S. Gibson, A. Lechner, H. Garcia Morales, and C. Yin Vallgren. Machine-induced Background Simulation Studies for LHC Run 1, Run 2 and HL-LHC. Technical Report CERN-ACC-2017-0025, CERN, Geneva, Apr 2017.

[45] W. Lampl, S. Laplace, D. Lelas, P. Loch, H. Ma, S. Menke, S. Rajagopalan, D. Rousseau, S. Snyder, and G. Unal. Calorimeter Clustering Algorithms: Description and Performance. Technical Report ATL-LARG-PUB-2008-002. ATL-COM-LARG-2008-003, CERN, Geneva, Apr 2008.

[46] M. Cacciari, C. P. Salam and G. Soyez. The anti-k_t jet clustering algorithm. *JHEP*, 04:063, 2008.

[47] D. Merritt. The distribution of dark matter in the coma cluster. *apj*, 313:121–135, Feb. 1987.

[48] L. Moneta, K. Cranmer, and W. Schott, G. andVerkerke. The RooStats project. In *Proceedings of the 13th International Workshop on Advanced Computing and Analysis Techniques in Physics Research. February 22-27, 2010*, page 57, 2010.

[49] C. e. a. Patrignani. Review of Particle Physics. *Chin. Phys.*, C40(10):100001, 2016.

[50] C. Perkins. Background taskforce, 2010.

[51] A. L. Read. Presentation of search results: the cl_s technique. *Journal of Physics G: Nuclear and Particle Physics*, 28(10):2693, 2002.

[52] A. Ruiz-Martinez, F. Monticelli, J. Hoya, and S. D. Jones. Electron and photon trigger efficiency plots using the full 2016 dataset. Technical Report ATL-COM-DAQ-2017-015, CERN, Geneva, Mar 2017.

[53] Y. Sasaki, C. Santoni, and Z. Weng. Calibration of the ATLAS hadronic barrel calorimeter (TileCal)using muons produced by a scraping beam. Technical Report ATL-TILECAL-INT-2012-007, CERN, Geneva, Oct 2012.

[54] N. Soni. ATLAS Forward Detectors and Physics. In *25th Lake Louise Winter Institute: Celebrating 25 years (LLWI 2010) Lake Louise, Alberta, Canada, February 15-20, 2010*, 2010.

[55] E. e. a. Torro Pastor. Searches for long-lived neutral particles decaying into heavy flavors in the hadronic calorimeter of ATLAS at $\sqrt{s} = 13$ TeV. Technical Report ATL-COM-PHYS-2016-579, CERN, Geneva, May 2016.

[56] P. van Dokkum, S. Danieli, Y. Cohen, A. Merritt, A. J. Romanowsky, R. Abraham, J. Brodie, C. Conroy, D. Lokhorst, L. Mowla, E. O'Sullivan, and J. Zhang. A galaxy lacking dark matter. *Nature*, 555:629–632, Mar. 2018.

[57] M. Wolverton. Muons for Peace. *Scientific American*, 297(3):26–28, Sept. 2007.

APPENDIX A. DISPLACED HADRONIC JETS

In setting limits this analysis relies on an accurate simulation of how decays within the volume of the HCal will unfold. Whether the simulation is done properly is not something that can be tested easily (as any such SM decays are extremely rare).

Study of the signal MC samples indicate that decays within the volume of the HCal result in very narrow jets. Jets originating from the center of the detector hadronize quickly, and the resulting constituent particles spread apart in the distance before the calorimeters. Those originating from within the detector volume aren't given this opportunity to spread out, resulting in the majority of the energy being collected in relatively few calorimeter cells. The width of these signal jets compared to typical jets is shown in Fig A.1. The jet width was not selected as a discriminant due to the fact that CR jets formed by detector effects also tend to originate from only a few cells, also resulting in narrow jet widths.

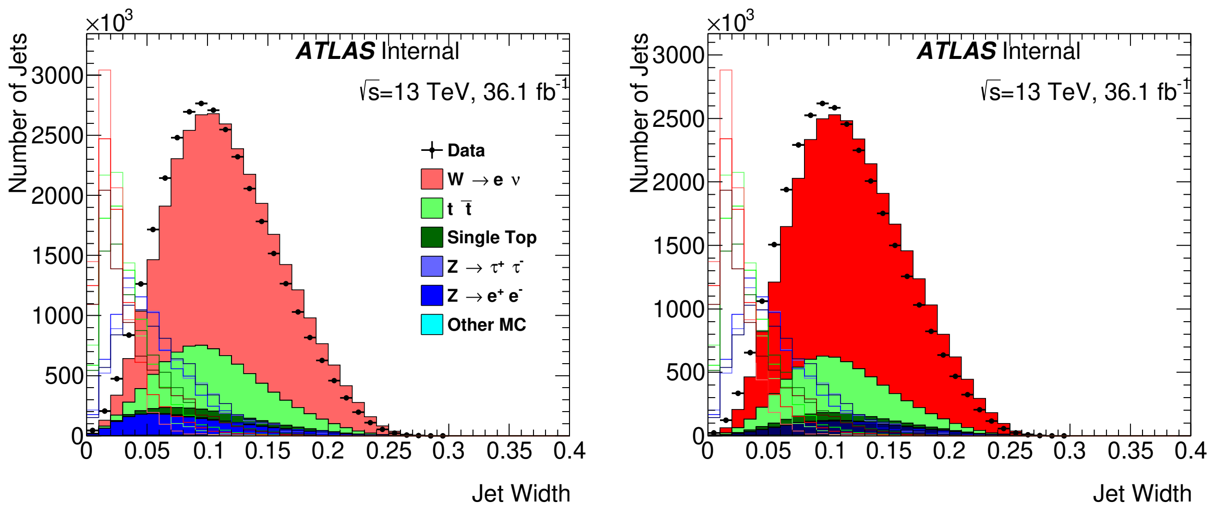

Figure A.1: The jet width for all jets in the W $\rightarrow e\nu$ (left) and W $\rightarrow \mu\nu$ (right) compared to the width of signal jets from decays within the volume of the HCal. Decays within the HCal result in narrow jets, decreasing width with increasing energy.

Jet reconstruction algorithms are all designed to (as accurately as possible) reconstruct jets originating from the center of the detector. Jets originating from decays within the calorimeter may not have their true energy reconstructed. This effect is indicated in Fig A.2 to be most dominant at lower energies, where the reconstructed energy is regularly overestimated by a factor of 50%.

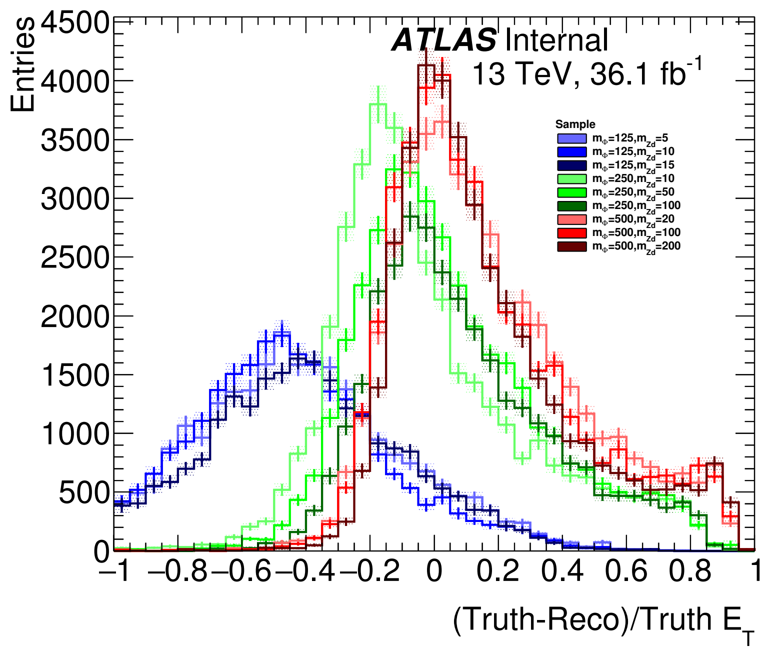

Figure A.2: A comparison of the truth particle energy to the energy of the matching reconstructed jet. Lower energy samples (with $m_{Z_d} = 5, 10, 15$GeV) are shown to have a poorly reconstructed energy.

This mis-reconstructed energy is not expected to affect the limits set by this analysis at all, as the mis-reconstruction shown here in simulation is expected to be an accurate representation of how such jets would be reconstructed in the true detector. Similar detector simulations in Geant are produced and studied for BIB (see Sec 6.1) which consist of jets being made from muons moving longitudinally through the detector cells[53]. Such simulations have also been used by a number of other analyses [13],[30],[55].

APPENDIX B. VERTEX SELECTION

An event with a reconstructed W and a single CR jet in principle has only 1 track (associated with the lepton). Given that the primary vertex (PV) is chosen by requiring at least 2 tracks with the greatest sum p_{T} squared there is some concern that the wrong PV may be chosen, resulting in a very different measurement of the CR jet probability in W+1 Jet events. However, each vertex actually has many low p_{T} tracks which do not contribute to the primary analysis objects. The number of these tracks in W+1 Jet events is shown in Figure B.1, and indicate that while the objects of interest do not provide enough tracks, there are sufficient additional tracks to determine the PV.

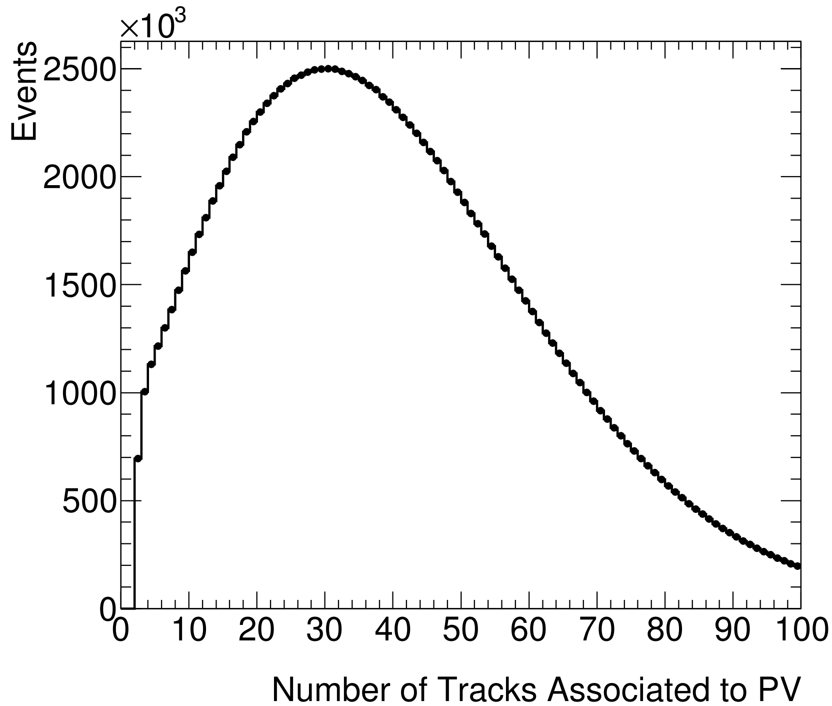

Figure B.1: The total number of tracks associated with the primary vertex in W+1 Jet events.

APPENDIX C. TAG AND PROBE TECHNIQUE

The tag and probe method is a typical means of measuring the efficiency and resolution of detectors in particle physics experiments.

This procedure is demonstrated in Fig C.1. The process begins by identifying one lepton (called the 'Tag') which is required to pass some selection criteria. A second lepton is then searched for (the 'Probe') which must have the opposite charge but no other applied selection.

The invariant mass of the lepton pair is then calculated. Most of the lepton pairs at high p_T originate from decays of the Z boson and therefore the Z mass peak is quite prominent and virtually all lepton pairs with an invariant mass within $\approx$ 25GeV of the Z are true Z events. Thus the fraction of the 'probe' leptons which pass selection gives a close approximation of the true efficiency of the lepton selection.

This efficiency is measured as a function of both p_T and η, as well as for a myriad of other selection cuts. To cover lower energy leptons the J/ψ particle is used as it similarly has a prominent dilepton mass peak at low energies. Such studies also model the background processes to ensure that the number of true J/ψ and Z events are selected, rather than the approximation mentioned above.

This procedure is also used to determine the energy resolution of different objects (leptons, photons, jets, etc) within the detector, based on the principle that the momentum of all objects in an event must be balanced (i.e. by observing the relative difference between the momentum of the tag and the momentum of the probe).

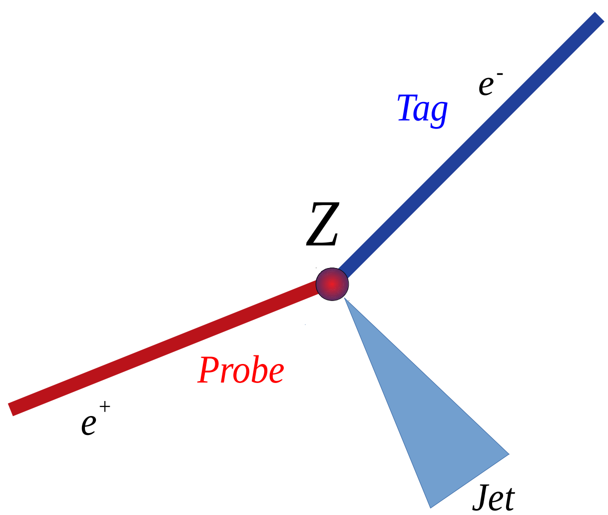

Figure C.1: An illustration of the Tag-And-Probe method, used for measuring the efficiency of lepton reconstruction.